The many facets of variabilities in X-ray binaries

by

Nazma Islam

Prof. Biswajit Paul

Raman Research Institute

Department of Physics

Indian Institute of Science

BANGALORE – 560 012

April 2016

TO

My parents

DECLARATION

I hereby declare that the work presented in this thesis titled, "The many facets of variabilities in X-ray binaries" is the result of the investigations carried out by me under the supervision of Prof. Biswajit Paul at the Astronomy and Astrophysics Group, Raman Research Institute, Bangalore, India, under the auspices of the Joint Astronomy Programme of the Department of Physics, Indian Institute of Science. I further declare that this has not formed the basis for the award of any degree, diploma, membership, associateship or similar title of any University or Institution. Keeping with the general practice, due acknowledgements have been made wherever the work described is based on other investigations.

Dated: **Nazma Islam**

Certified by

Biswajit Paul

Professor

Astronomy and Astrophysics Group

Raman Research Institute

Bangalore-560080

and

Tarun Deep Saini

Assistant Professor

Department of Physics

Indian Institute of Science

Bangalore- 560012

PUBLICATIONS

PUBLICATIONS INCLUDED IN THE THESIS

1. Effects of variability of X-ray binaries on the X-ray luminosity functions of the Milky Way, **Islam, N.**; & Paul, B., 2016, New Astronomy, 47, pp 81–87 .

2. A Suzaku view of IGR J16393–4643, **Islam, N.**; Maitra, C.; Pradhan, P.; & Paul, B., 2015, MNRAS, 446, 4148.

3. Orbital phase resolved spectroscopy of GX 301–2 with MAXI, **Islam, N.**; & Paul, B., 2014, MNRAS, 441, 2539.

4. Orbital evolution and search for apsidal motion in the eclipsing High Mass X-ray binary 4U 1700–37, **Islam, N.**; & Paul, B., MNRAS submitted.

OTHER PUBLICATIONS

1. Variations in the pulsation and spectral characteristics of OAO 1657–415, Pradhan, P.; Maitra, C.; Paul, B.; **Islam, N.**; & Paul, B. C., 2014, MNRAS, 442, 2691.

2. Variability study of the High Mass X-ray binary IGR J18027–2016 with Swift–XRT, Aftab, N.; **Islam, N.**; & Paul, B., MNRAS submitted.

CONFERENCE PROCEEDINGS

1. Average spectral properties of galactic X-ray binaries with 3 years of MAXI data, **Islam, N.**, Mihara, T., Sugizaki, M., Paul, B., & Nath, B. B. 2013, Astronomical Society of India Conference Series, 8, 109 (arXiv:1309.4581).

2. Effect of variability of X ray binaries on the X ray luminosity functions of our Galaxy, **Islam, N.** & Paul, B., 39th COSPAR Scientific Assembly. Held 14-22 July 2012, in Mysore, India, Abstract D1.2-32-12, p.800.

Abstract

More than half a decade of X-ray astronomy with various balloon borne and space orbiting X-ray instruments have led to discoveries and detailed studies of X-ray binaries. An important property of X-ray binaries is the intensity variations of different magnitude at a wide range of timescales from milliseconds (quasi-periodic oscillations, millisecond pulsations), few weeks (orbital and super-orbital modulations) or longer (outbursts etc). In this thesis, the different types of variability of X-ray binaries are considered in X-ray binary population studies as well as probing certain aspects of some individual systems.

In **Chapter 1**, we provide an introduction to the various types of variabilities seen in different classes of X-ray binaries. We mention in detail the various periodic and aperiodic variabilities seen in X-ray binaries.

In **Chapter 2**, we describe in some detail the various X-ray all sky monitors and X-ray observatories, data from which have been utilised in for the works carried out in this thesis. We also describe the various data analysis techniques we have used in this thesis.

The rest of the thesis is divided into two major sections: Variability studies of individual systems and X-ray binary population studies

Variability studies of individual systems

In **Chapter 3**, we report results from an investigation of energy resolved orbital

intensity profiles of GX 301–2 and carried out exhaustive orbital phase resolved spectroscopic measurements of GX 301–2 with MAXI. The orbital variation of the spectral parameters, especially the relation between equivalent width of Fe line and column density of absorbing matter are then utilised to examine the models about mode of accretion onto the neutron star in GX 301-2: circumstellar disk model by Pravdo & Ghosh (2001), and the accretion stream model by Leahy & Kostka (2008). A very large equivalent width of the iron line along with a small value of the column density in the orbital phase range 0.10-0.30 after the periastron passage indicates an asymmetry in the distribution of the matter around the neutron star, strongly favouring the accretion stream model by Leahy & Kostka (2008).

Presence of an eclipse in a X-ray binary can be useful in determining orbital parameters like inclination and estimating the orbital evolution by eclipse timing method, which is reported in **Chapter 4**. For the HMXB system IGR J16393–4643, we found a short eclipse in the Swift–BAT light-curve and utilised it to constrain the orbital inclination of the system. We have also studied for the first time broad- band pulsation and spectral characteristic of the system with a Suzaku observation, showing sub-orbital intensity variations.

For the eclipsing and non-pulsing HMXB 4U 1700–37, the orbital evolution is studied using mid-eclipse times from archival as well as from long term light-curves of X-ray all sky monitors. The orbital period decay rate is estimated to be $\sim 5 \times 10^{-7}$ /yr, an order slower than the previous measurement by Rubin et al.(1996). Since no pulsations are detected in this system, it is difficult to estimate its orbital parameters, especially eccentricity. Using mid-eclipse times from 10 years of Swift–BAT data, we have independently constrained the eccentricity of the binary system.

X-ray binary population studies

In **Chapter 5**, we report results from an analysis of the 16 years light-curves of X-ray binaries in 2-10 keV energy band of RXTE–ASM, used to construct the differential and integral probability distribution of count-rates. These distributions are then employed to

construct multiple snapshots of X-ray binary luminosity functions of Milky Way instead of averaging the luminosities, an improvement over previous analysis by Grimm et al. (2002). We found that the averaged luminosities of highly variable X-ray binaries do not represent their true positions in XLFs and the variability of X-ray binaries do indeed significantly affect the luminosity functions.

*In **Chapter 6**, the measurement of the averaged spectra of X-ray binaries using MAXI data are reported and are used for constructing the composite X-ray spectrum. These composite X-ray binary spectra are useful in constraining the contribution of X-ray binaries in extra-galactic SEDs constructed from the simultaneous Chandra / XMM–Newton and NuSTAR observations of these galaxies. These SEDs will also serve as a useful input in estimating the contribution of XRB heating at high redshift IGM during Epoch of Reionization.*

*In **Chapter 7**, we summarise the main conclusions of the various works carried out in this thesis and discuss some future works related to this thesis.*

Contents

---

[1]The work presented in this Chapter is published as a paper (2014, MNRAS, 441, 2539)

[2]The work presented in this Chapter is published as a paper (2015, MNRAS, 446, 4148) and the other submitted to MNRAS for publication

---

[3]The work presented in this Chapter is published as a paper (2016, New Astronomy, pp. 81-87)

List of Tables

List of Figures

Chapter 1

Introduction

1.1 Introduction

Human eye is sensitive in the spectral range of 400-800 nm, $i.e$ the optical part of the electromagnetic spectrum. When we look at the night sky, we see stars radiating with same intensity and color. Very rarely a nova or a supernova appear in which a previously detected star increases its intensity by several orders of magnitudes. Now imagine the scenario where human eye is sensitive to 0.01-10 nm, $i.e$ in the domain of X-rays. Of course, X-rays cannot penetrate Earth's atmosphere, making it possible to sustain life on Earth in first place. Just for the sake of an hypothetical scenario, imagine human eye being sensitive to X-rays and X-rays from celestial objects are not blocked by Earth's atmosphere. What would we see when we looks up at the sky ? We would see a dynamically changing sky, a far-cry from the static sky in optical regime. The X-rays would come from celestial objects and would have very rapid changes in intensities and even spectral color. Some of these X-ray sources will suddenly become very bright outshining every other objects and some of them will fade into oblivion, all in the timescales of days, hours or even shorter timescales. Majority of the bright X-ray sources are the X-ray binaries.

1.2 X-ray binaries

These X-ray binaries are gravitationally bound binary systems, consisting of a compact object like a neutron star or a black hole together with a main sequence, supergiant or a white dwarf as companion star, orbiting a common center of mass. The typical luminosities of these sources $\sim 10^{34-38}$ ergs/sec, 2-4 orders of magnitude brighter than Sun. Accretion is the main source of power in X-ray binaries, in which matter from the companion is captured by the compact object either by stellar wind or Roche lobe overflow.

Ever since the serendipitous discovery of the X-ray binary Sco X-1 with a payload consisting of three large Geiger counters flown onboard an Aerobee rocket in 1962 (Giacconi et al., 1962), more than half a decade of X-ray astronomy with various balloon borne and space orbiting X-ray instruments have led to discoveries and detailed studies of X-ray binaries. Important property of these X-ray binaries is the intensity variations by a large factor of a few to several orders of magnitude at all timescales from milliseconds (quasi-periodic oscillations, millisecond pulsations) to over few weeks (orbital and super-orbital modulations) and longer (outbursts). A majority of these intensity variations are associated with the change in mass accretion rate on to the compact object. The accretion mechanisms of different classes of X-ray binaries and the associated types of intensity variations will be described in detail in subsequent sections.

1.3 X-ray emission processes

For a body of mass M and radius R, the gravitational potential energy ΔE_{acc} released by the accretion of mass m on to its surface is given by

$$\Delta E_{acc} = \frac{GMm}{R} = (\frac{GM}{Rc^2})mc^2 = \eta mc^2 \tag{1.1}$$

where $\eta = (\frac{GM}{Rc^2})$ is called the accretion efficiency. The accretion efficiency is strongly dependent on the compactness of the accreting object, the larger the ratio of M/R,

greater is the accretion efficiency. For a neutron star with mass ~ 1.4 M$_\odot$ and radius of 10 km, $\eta \sim 0.15$, whereas for black holes as compact object, the accretion efficiency η can be as high as 0.3. The luminosity of the X-ray binary is closely tied to its mass accretion rate.

The radiation seen from X-ray binaries comprises of host of emission processes comprising of both thermal and non-thermal radiation mentioned below

1.3.1 Thermal processes

Blackbody radiation

Blackbody radiation or thermal radiation is emitted by the matter in thermal equilibrium. The spectra of a blackbody radiation follows a Planckian distribution, where the peak of the emission is dependant on the temperature of the radiating source.

In X-ray binaries, the emission from an accretion disk consists of a sum of multi-temperature blackbody components, arising from the inner radius of the accretion disk.

Bremsstrahlung radiation

Bremsstrahlung or free-free emission arises due to the acceleration of a charge particle for *e.g* an electron, in the presence of a Coulomb field of a high energy particle like a proton or an ion. Bremsstrahlung plays an important role in the diffuse X-ray emission of the intergalactic gas in clusters of galaxies as well as in supernova remnants.

1.3.2 Non-thermal processes

Compton Scattering

In Compton scattering, the high energy photons undergo scattering by low energy electrons, leading to a decrease in the energy of the photons. In Inverse Compton scattering, the high energy electrons scatter the low energy photons, leading to an increase in the energy of the photons.

In many X-ray binaries, the thermal radiation from the compact object provides the lower energy seed photons, which then undergo Inverse Compton scattering by the high energy electrons present in the vicinity of the compact objects.

Cyclotron and Synchrotron radiation

The radiation emitted by the acceleration of relativistic charged particles in a magnetic field is called Synchrotron radiation. Although this is not an important emission mechanism in most X-ray binaries, we see the presence of cyclotron absorption lines in the spectra of many accretion powered X-ray pulsars which results from the resonant scattering of X-rays by electrons in Landau orbits in the high magnetic fields near the poles of the neutron star (Pottschmidt et al., 2012; Maitra, 2013).

1.3.3 Fluorescence and atomic lines

Due to the reprocessing of the radiation by the surrounding circumstellar matter in X-ray binaries, we see various fluorescence lines in the spectra of these sources. The most common are the iron fluorescence lines (Fe Kα and Fe Kβ lines), which have high fluorescence yield and occur at 6.4 keV, falling in the energy bandpass of a majority of X-ray observatories. These Fe fluorescence lines serve as an excellent tracer to study the behaviour of matter in strong gravity regime (relativistic broadened lines) and distribution of matter in X-ray binaries.

Other than fluorescence lines, we also see other atomic lines in absorption present in interstellar medium like Si and other emission lines from various ionisation states of atoms like He like Ne (Ne IX), H like O (O VIII) etc.

1.4 Classification of X-ray binaries and their variabilities

1.4.1 High Mass X-ray binaries

HMXBs are systems consisting of a magnetised neutron star (having a field of the order of 10^{12} G – Pottschmidt et al. 2012) or a black hole as the compact object and an early type star ≥ 10 M$_\odot$ (usually O type or B type stars). Most of the HMXB systems are accreting X-ray pulsars and Cyg X–1, Cyg X–3 and SS 433 are the HMXB Black Hole (BH)/ Black Hole Candidate (BHC) in our Galaxy and LMC X–1, and LMC X–3 are the identified HMXB BH systems in nearby galaxies. The HMXBs are further subdivided into three categories:

Be High Mass X-ray binaries

A majority of galactic HMXBs are Be/X-ray binaries, which consist of a non supergiant, fast rotating B type (showing spectral lines in emission; hence Be star) optical star as the companion and a neutron star as the compact object. The only exception is MWC 656 which is a Be/X-ray binary system with a black hole as the compact object (Casares et al., 2014). Except 4U 0115+63 and V 0332+53, Be/XRBs are slow pulsars with P$_{spin} \geq 10$ s and long orbital period (≥ 20 days; except SAX J2103.5+4545). The Be star has a circumstellar disk around it, sustained from the material expelled from the rapidly rotating Be star and during its orbit around the companion star, the neutron star passes through the disk and accretes from the dense equatorial Be star disk, producing bright outbursts lasting for several days or even weeks (Paul & Naik, 2011). Most of the Be/XRBs are transients, with luminosities of 10^{37} ergs/sec during the peak of the outbursts. The X-ray behaviour of transient Be/XRBs are characterised by two types of out-bursting activity.
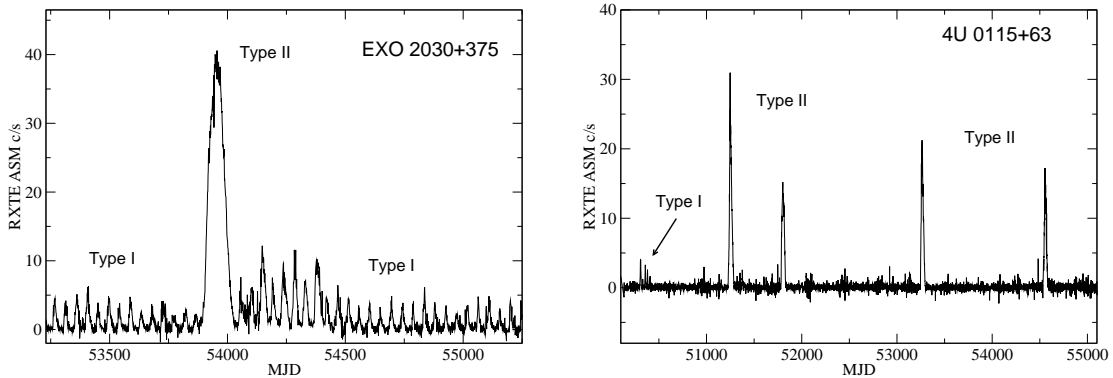
Figure 1.1: *RXTE*–ASM light-curves of two Be/XRB systems EXO 2030+375 and 4U 0115+63, showing both Type I and Type II outbursts. In EXO 2030+375, Type I outbursts are more common whereas in 4U 0115+63, Type II outbursts are more common. Image taken from Reig (2011)

Type I outbursts: These are regular and periodic (or quasiperiodic) outbursts, normally peaking at or close to periastron passage of the neutron star and considered to be associated with increased mass accretion during periastron passage.

Type II outbursts: These outbursts are more luminous than Type I outbursts and may reach the Eddington luminosity for a neutron star (Negueruela et al., 1998). They do not show any preferred orbital phase and last for a large fraction of an orbital period or even for several orbital periods. The long term light-curve from *RXTE*–ASM is shown in Figure 1.1 for two Be/XRB systems: EXO 2030+375 and 4U 0115+63 and the relative occurrence of Type I and Type II outbursts.

Supergiant High Mass X-ray binaries

The other major group of HMXBs is the Supergiant High Mass X-ray binaries (SGXBs), where the compact object has an early type supergiant star as the optical companion and the accretion on to the compact object occurs via stellar wind or Roche lobe overflow. These systems have short orbital period $P_{orb} \leq 10$ days and are further subdivided into
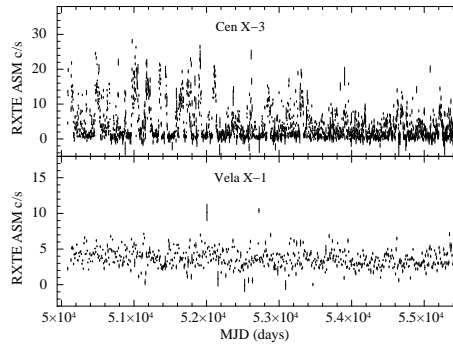
Figure 1.2: *RXTE*–ASM light-curves of two SGXB systems Cen X–3 (disk-fed system) and Vela X–1 (wind-fed system) binned by their orbital period and shown here for ∼600 orbital cycles. Both the SGXBs have persistent X-ray emission with presence of large variability, as compared to outbursts seen in Be/XRB systems in Figure 1.1

Roche lobe filling supergiants with short spin periods and underfilled Roche lobe supergiants with longer spin periods (Jenke et al., 2012). In SGXBs, the companion star emits a substantial stellar wind having a mass loss rate of 10^{-6} $M_\odot$ yr^{-1}, whereas the neutron star in a relatively close orbit captures a small fraction of this wind, sufficient to power a bright X-ray source. Hence a majority of supergiant HMXBs are persistent sources. If mass transfer occurs via Roche lobe overflow, then the X-ray emission is stronger and an accretion disk is formed around the neutron star. At present, Cen X–3, SMC X–1 and LMC X–4 are the known disk-fed SGXB systems while other systems like Vela X–1 are wind-fed systems (Figure 1.2). The supergiant phase of stars is short-lived due to the evolutionary timescales involved; hence the supergiant HMXBs (SGXBs) are less in number than the Be/X-ray binaries. However, with the discoveries of highly obscured SGXBs with *INTEGRAL* , the number of known SGXBs in our Galaxy is increasing. Some of the supergiant HMXBs, called the highly absorbed supergiant HMXBs, have very strong X-ray absorption with column density of absorbing matter $N_H \sim 10^{23}$ cm^{-2}.

Supergiant Fast X-ray Transients

Supergiant Fast X-ray Transients are a new class of X-ray binaries consisting of a compact object (mostly a neutron star) orbiting a OB supergiant. Discovered by *INTEGRAL*

(Sguera et al., 2006), these systems are characterized by occurrence of short, sporadic and bright X-ray flares, lasting for few minutes to even few hours and reaching a peak luminosity of a few 10^{36} ergs/sec. Their quiescent level is at about 10^{32} ergs/sec (Bozzo et al., 2012), thus making SFXTs a class of transients with the largest dynamic range $(10^3 - 10^5)$ among HMXBs . There are several models explaining the nature of these outbursts, proposing a clumpy nature of the wind from supergiant companion (Sidoli et al., 2007; Walter & Zurita Heras, 2007) or on the properties of the compact object like propeller effect or magnetic gating (Grebenev & Sunyaev, 2007; Bozzo et al., 2008).

1.4.2 Low Mass X-ray binaries

X-ray binaries consisting of a companion star ≤ 1 M$_\odot$ (usually K or M type stars or a white dwarf), along with a neutron star or a black hole as the compact object are the Low Mass X-ray binaries (LMXBs). The binary components are very close to each other such that the companion star fills its Roche Lobe and the accretion on to the compact object occurs via Roche Lobe overflow, forming an accretion disk. Different types of variabilities are seen for LMXBs containing a neutron star and a black hole.

Neutron Low Mass X-ray binaries

Most NS LMXBs consist of a weakly magnetised neutron star (B $\sim 10^8$ G), some of which show coherent millisecond pulsations, quasi-periodic oscillations (mHz to kHz), thermonuclear burst oscillations (similar to spin period of these systems) etc. They also show Type I bursts, characterised by fast rise in intensity followed by slow decay and can last for tens of seconds to hundreds of seconds. The Type I bursts or the thermonuclear X-ray bursts occur due to the matter accreted on to the surface of the neutron star, leading to an unstable nuclear H/He burning, whereas Type II bursts occur due to changes in accretion rates or accretion instability (Lewin et al., 1993; Bhattacharyya, 2010). In addition to Type I and Type II bursts, NS LMXBs also show super-bursts, characterized by higher luminosities and are caused by unstable nuclear carbon burning (Woosley & Taam, 1976). Other than X-ray bursts lasting for few days, NS LMXBs also undergo
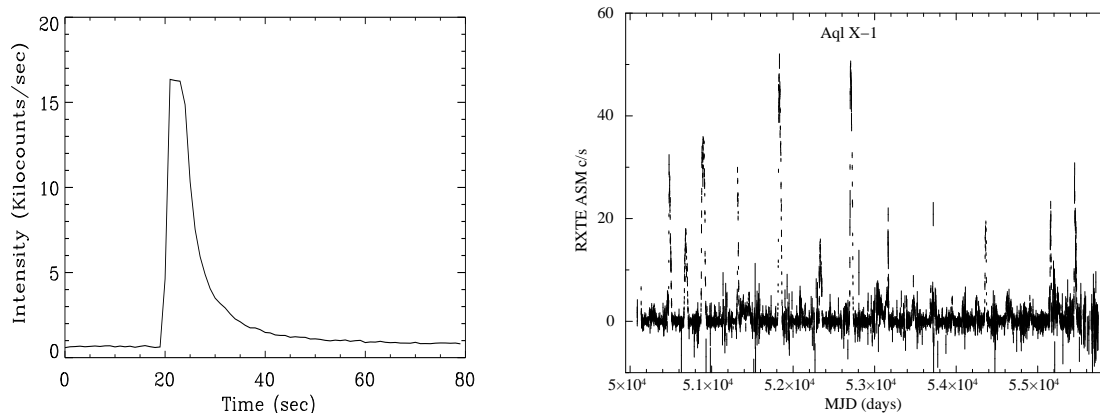
Figure 1.3: *Left panel:* X-ray intensity profile of a typical thermonuclear X-ray burst observed from an LMXB with *RXTE*–PCA, lasting few tens of seconds. Image taken from Bhattacharyya (2010). *Right panel: RXTE*–ASM light-curve of Aql X–1 showing outbursts lasting for days.

outbursts lasting months to years. Figure 1.3 shows a comparison of intensity variations in LMXBs on different timescales. Other than intensity variability, the NS LMXBs also show spectral variability and are broadly classified as Z sources and Atoll sources on the basis of the tracks traced on the X-ray hardness-intensity and X-ray color-color diagrams (Figure 1.4).

Black hole LMXBs

In contrast to NS LMXBs which are mostly persistent systems, black hole LMXBs (except GRS 1915+105 and GX 339-4) are highly transient systems. During quiescence, they occupy very low luminosity states and occasionally they go into outbursts (novae), during which their luminosities increase by several orders of magnitude and they occupy very high luminosity states for a considerable period of time (Remillard & McClintock, 2006). Figure 1.5 shows the light-curves of a persistent BH LMXB system GRS 1915+105 and a transient system V404 Cyg. These outbursts are thought to be triggered due to accretion disk instability and the recurrence timescales of these outbursts are usually in timescales of one year to several decades. Other than intensity variations, BHBs also
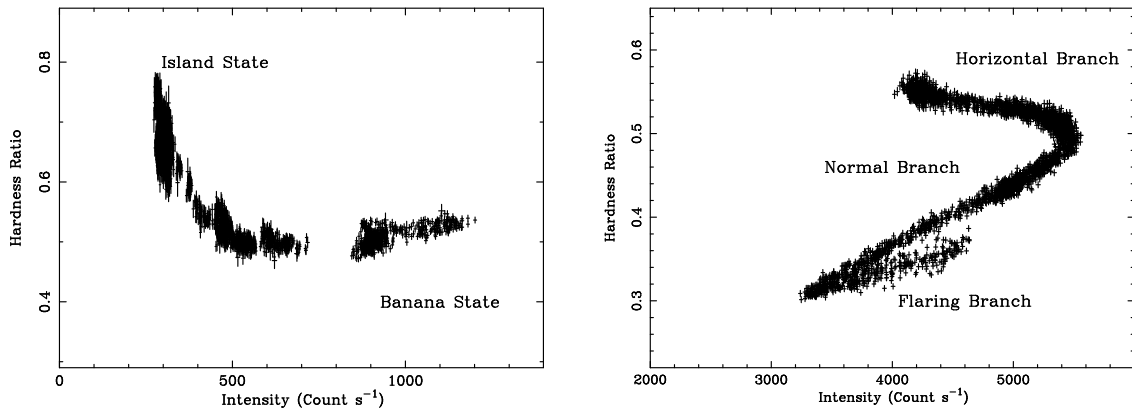
Figure 1.4: X-ray hardness-intensity diagrams of an atoll source 4U 0614+091 showing the island and banana states (left panel) and a Z-track source GX 340+0 (right panel) constructed from *RXTE*–PCA observations. Hardness is defined as the ratio of counts/sec in the bands 7.3–18.5 keV and 4.1–7.3 keV and intensity in the band 1.9–18.5 keV. Image taken from Church et al. (2014).

exhibit spectral variability, occupying different X-ray states: High/Soft state, (dominated by thermal radiation from inner accretion disk), Low/Hard state (dominated by non-thermal component of spectrum) and Steep Power-law state (power-law index $\Gamma \geq 2.4$). In case of BHBs, there is a strong correlation between transitions between certain X-ray states and the presence of radio jets.

1.5 Periodic variability in X-ray binaries

Periodic variation in X-ray intensities have been seen in many X-ray binaries on all timescales ranging from milliseconds (accreting millisecond X-ray pulsars), tens or hundreds of seconds (HMXB X-ray pulsars, orbital period of LMXBs) to days or months (orbital period of HMXBs, super-orbital period). These variations are generally associated with spin period of the neutron star, orbital period of the binary system and due to the precession of structures in an accretion disk. A brief description of different periodic X-ray variabilities are given below
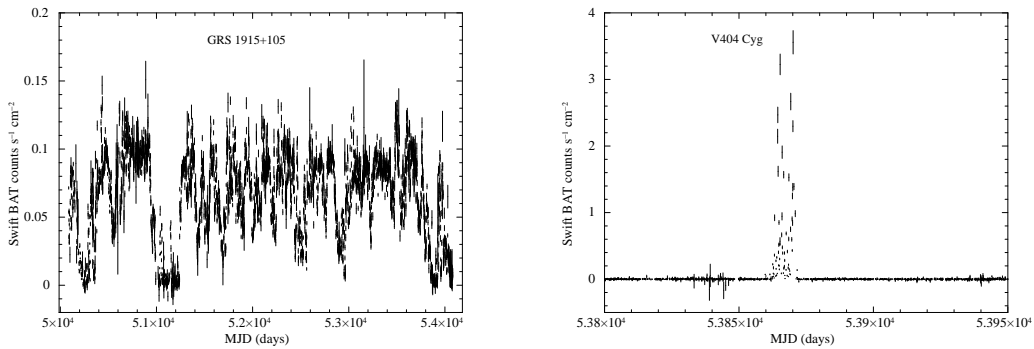
Figure 1.5: *Swift*–BAT light-curves of black hole LMXBs GRS 1915+105, which is a persistent system showing rapid variability (left panel) and V404 Cyg, a transient system which underwent a huge outburst in 2015 (right panel).

1.5.1 Pulsations

In case of an accreting pulsar, the accreted matter is magnetically channelled on to the poles of the neutron star, leading to the formation of accretion column and hotspots which radiates in X-rays. The X-ray emission resulting from the accretion is anisotropic, which due to spin of the NS appears as pulsed X-ray emission. The spin period of X-ray pulsars can range from few milliseconds (accreting X-ray pulsars, usually LMXBs) to few thousands of seconds (HMXB pulsars). The X-ray pulse profiles of accreting X-ray pulsars are complex and show dependence on energies and luminosities as shown in Figure 1.6 and can be used to infer the accretion geometry and beaming pattern of the neutron star (Maitra, 2013).

1.5.2 Orbital Intensity modulation

The orbital period of an X-ray binary system is given by the Kepler's third law

$$P_{orb} = \left(\frac{4\pi^2 a^3}{G(M_c + M_{NS})}\right)^{\frac{1}{2}} \tag{1.2}$$

where M_{NS} is the mass of the compact object, M_c is the mass of the companion star and a is the orbital separation between the binary components. LMXBs are compact
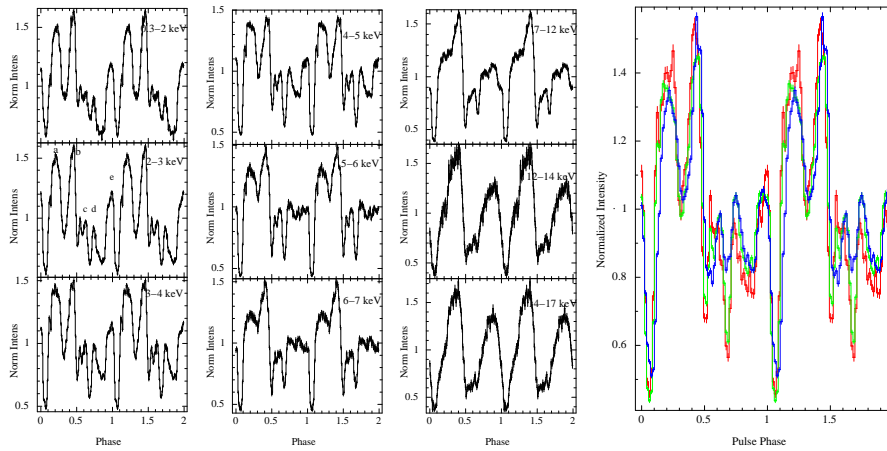
Figure 1.6: Variation in pulse profiles of Vela X–1 as function of energies (three panels from left to right) and luminosity of source (last panel on right). Image taken from paper by Maitra & Paul (2013).

systems with their orbital period ranging from few minutes to few days, whereas HMXBs have orbital period ranging from few days to few hundreds of days (except Cyg X–3 which has orbital period of 4.7 hours). Most of the orbits of X-ray binaries with a short orbital period are circularised due to tidal interactions, whereas long orbital period X-ray binaries like Be/X-ray binaries have eccentric orbits.

The orbital modulation of the X-ray intensities from the X-ray binary occurs due to various orbital phase dependant factors like the absorption and scattering of X-rays in the stellar wind of the companion, accretion streams, accretion disks etc. In Be/XRB systems like EXO 2030+375, there is an occurence of periodic X-ray outbursts when the accretion on to the compact object is enhanced around periastron passage (right panel of Figure 1.7), whereas in the orbital intensity profile of GX 301–2, the X-ray flare occurs before the periastron passage. Also depending on the orbital inclination of the system, we can see X-ray eclipses, which will be explained in detail in the next subsection.

1.5.3 X-ray Eclipses

Depending on the orbital inclination of the binary system, the compact object is periodically occulted along our line of sight either fully or partially by the companion, or
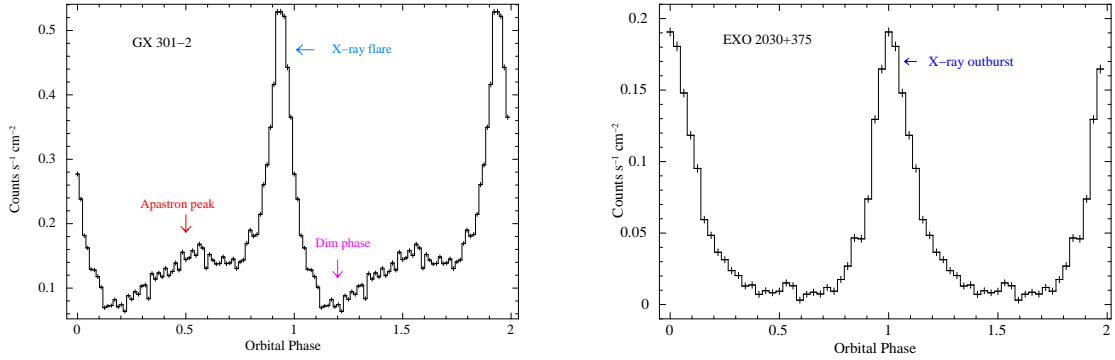
Figure 1.7: Orbital intensity profile of GX 301–2 (left panel) and EXO 2030+375 (right panel) constructed with 2-20 keV energy band of *MAXI*–GSC . The orbital intensity profile of EXO 2030+375 shows the presence of X-ray outbursts during periastron, indicating increase in mass accretion arising from the passage of the neutron star through the circumstellar disk of the Be companion star. The complex orbital intensity profile of GX 301–2 indicates a non symmetric wind from the companion star.

absorbed by the outer structure of the accretion disk, giving rise to full or partial X-ray eclipses. The probability of the compact object being periodically occulted by the companion star, *i.e* X-ray eclipse occuring *P(e)*, is given by the following equation in Ray & Chakrabarty (2002), for a circular orbit.

$$P(e) \sim 0.38 \quad (\frac{P_{orb}}{15\text{days}})^{-\frac{2}{3}} \quad (\frac{M_O}{15M_\odot})^{-\frac{1}{3}} \quad (\frac{R_O}{24R_\odot}) \tag{1.3}$$

where M_O is the mass of the companion star and P_{orb} is the orbital period of the X-ray binary system. Hence X-ray eclipses are mostly seen in binary systems with short orbital period and no long period X-ray binary has shown X-ray eclipses yet. In addition to eclipses, some LMXBs show periodic dipping behaviour in the light-curves, which arises due to the absorption of X-rays by the accretion disk structure, as seen in Figure 1.8 (White & Swank, 1982; Frank et al., 1987).
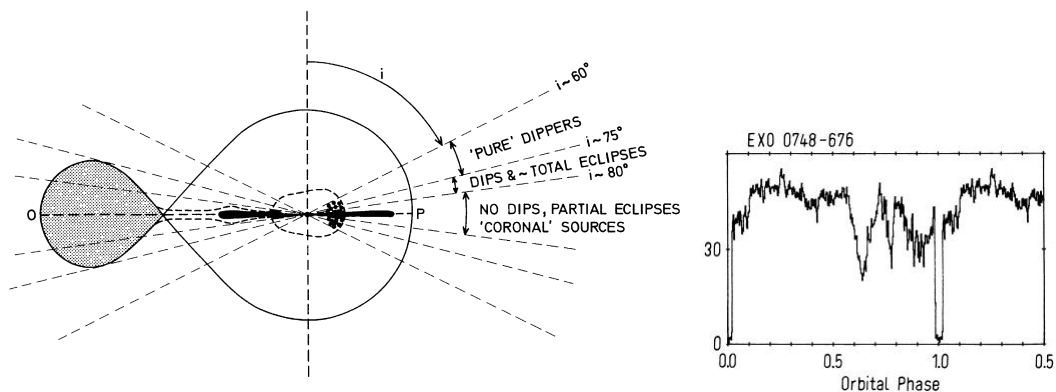
Figure 1.8: Right panel shows the different types of X-ray orbital flux modulation in LMXBs caused by the different inclination angles. Image taken from the paper by Frank et al. (1987). Left panel shows the orbital intensity profile of an LMXB EXO 0748-676, with an orbital period of 3.8 hours, showing the presence of both dips and eclipses. Image taken from Parmar et al. (1986).

1.5.4 Super-orbital intensity modulations

Along with periodicities associated with spin period and orbital period, some X-ray binaries also show additional periodicities associated with precession of the tilted accretion disk that periodically obstructs the X-ray source (Her X–1 – right panel of Figure 1.9, SMC X–1, LMC X–4) or the directions of the emitted jets (SS 433). These intensity modulations, called super-orbital intensity modulations, are seen in both HMXBs and LMXBs and occur on timescales of tens to hundreds of days (Kotze & Charles, 2012; Corbet & Krimm, 2013). These super-orbital intensity variations are not always stable (Paul et al., 2000).
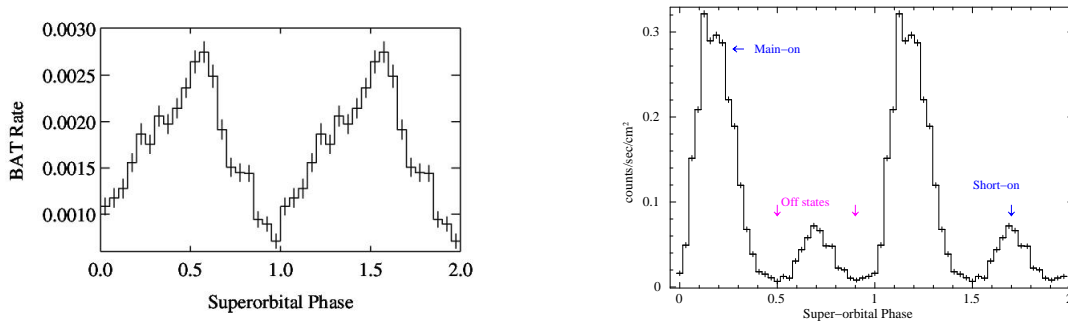
Figure 1.9: Left panel shows the super-orbital intensity modulation of HMXB 2S 0114+650 in *Swift*–BAT from Corbet & Krimm (2013). Right panel shows the super-orbital intensity modulation of LMXB Her X–1 in *MAXI*–GSC . The super-orbital intensity profile of Her X–1 shows the presence of two on states separated by two off states. The two on states, called the Main-on and the Short-on, represents the states when the central X-ray source is unobstructed and partially obstructed respectively by the precessing accretion disk.

1.6 Quasi-periodic or aperiodic variability in X-ray binaries

1.6.1 Quasi-periodic oscillations

The power spectra of some X-ray binaries show one or more peaks with a finite width (minimum quality factor $\nu/\delta\nu \sim 2$) called the quasi-periodic oscillations (QPO) (shown in Figure 1.10), which in some of the models are thought to be associated with the motion of inhomegenous matter in the inner accretion disks. QPOs can have a wide range of frequencies: from mHz to kHz and centroid frequencies are related to the magnetic fields, X-ray intensities and spectral states of the sources (Alpar & Shaham, 1985; van der Klis, 1989).
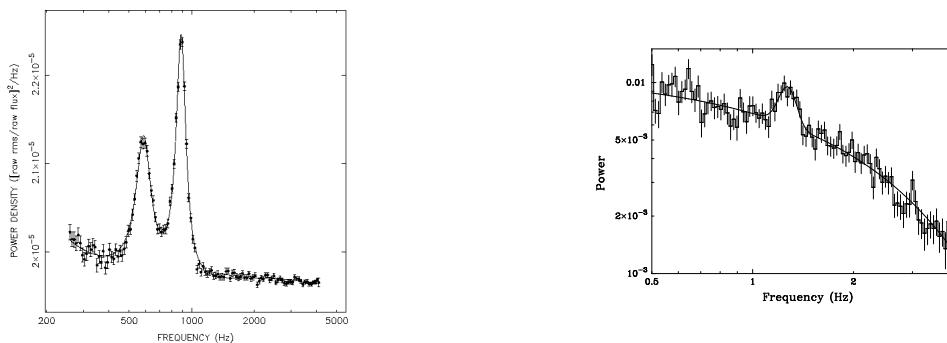
Figure 1.10: Power density spectra of LMXB Sco X–1 (right panel), showing the presence of twin kilohertz (kHz) QPO and HMXB XTE J0111.2–7317 (left panel), showing the presence of ~ 1 Hz QPO. Image taken from van der Klis et al. (1997) for Sco X–1 and Kaur et al. (2007) for XTE J0111.2–7317.

1.6.2 Power spectra of X-ray binaries

Rapid aperiodic X-ray variabilities are also seen in the light-curves of different types of X-ray binaries, which are investigated by constructing Power Density Spectra (PDs). These PDS are dominated by a strong band-limited noise component, which follows a power law with an index of roughly 1 at high frequencies and breaks at a frequency between 0.02 and 32 Hz, below which the spectrum is relatively flat and super-imposed on this noise component are the QPOs (seen in right panel of Figure 1.10) (Wijnands & van der Klis, 1999).

1.6.3 Outbursts from BHBs

As mentioned in Section 1.4.2, LMXB systems containing black hole as a compact object undergo huge X-ray outbursts where their luminosities increases by several orders of magnitude. The recurrence timescales of a BH LMXB going into outbursts are several years to several decades. The right panel of Figure 1.5 show the *Swift*–BAT light-curve V404 Cyg, a transient system which underwent a huge outburst in 2015.
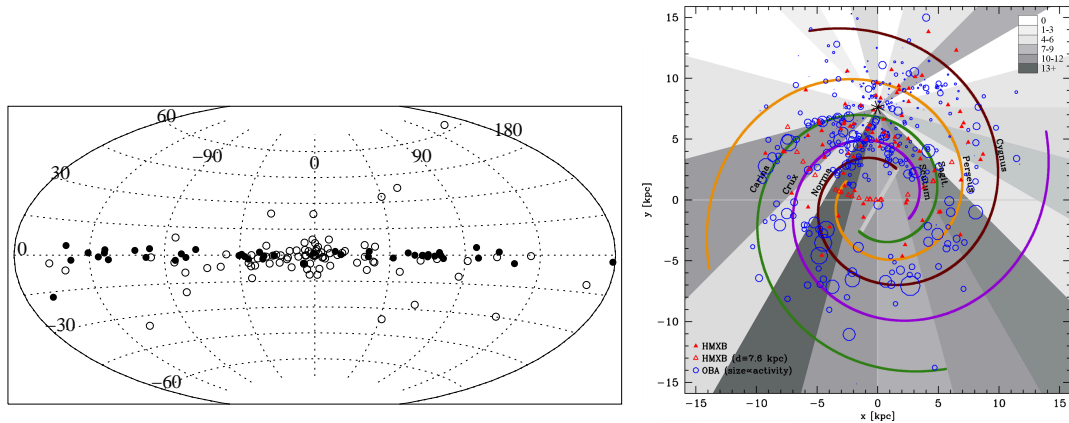
Figure 1.11: *Left Panel :* Distribution of X-ray binaries (black filled circles: HMXBs, open circles:LMXBs) as seen in Milky Way. We see a clustering of LMXBs around the galactic bulge. HMXBs are found to be confined in the galactic plane. Figure taken from Grimm et al. (2002). *Right Panel :* Galactic distribution of HMXBs (triangles) and OB associations (circles), showing the correlation of HMXBs and region of star-forming activity OB assciations and the concentration of HMXBs along the spiral arms of galaxy. Figure taken from Bodaghee et al. (2012b)

1.7 Distribution of X-ray binaries in the Galaxy

1.7.1 Spatial distribution of HMXBs

Due to massive nature of the companion star, HMXBs are short-lived system with an evolutionary timescales of 10^{5-6} years. They are typically associated with star-forming regions like spiral arms and OB associations (Bodaghee et al., 2012b; Coleiro & Chaty, 2013a) (right panel of Figure 1.11), tracing regions of high star formation. The X-ray binaries receive a natal kick of ~ 100 km/sec and due to shorter evolutionary timescales, they do not migrate far from the birthplace and they are mostly concentrated in the galactic plane (left panel of Figure 1.11).

1.7.2 Spatial distribution of LMXBs

The LMXBs have an evolutionary timescales of 10^{8-9} years and are tracers of a very old stellar population. From the right panel of Figure 1.11, we see that the distribution of LMXBs is strongly peaked around the galactic bulge and many of them are also located in globular clusters. The vertical distribution of LMXBs from the galactic plane are broader than that of HMXBs (left panel of Figure 1.11) and there are many sources at larger distances from the galactic plane. LMXBs are more numerous than HMXBs in Milky Way.

1.8 Motivation and outline of the thesis

In this thesis, we have utilised the different types of variability of X-ray binaries to

- To probe certain aspects of intensity variations in individual systems.

- To investigate the effects of variability of X-ray binaries on X-ray population studies of Milky Way.

Chapter 1 gives a brief description of the X-ray binaries and the different types of intensity variations seen in these systems. We also describe very briefly the various X-ray emission processes seen in X-ray binaries. We then describe the various kind of periodic variabilities seen in X-ray binaries like pulsations, orbital intensity modulations X-ray eclipses and super-orbital intensity modulations. Different types of aperiodic or quasi-periodic variabilities like quasi-periodic oscillations, band limited noise component in power spectra and outbursts in Black hole X-ray binaries are briefly touched upon. We also describe the distribution of HMXB and LMXB population seen in our Galaxy.

Chapter 2 provides a description of various X-ray all sky monitors whose long term monitoring data of X-ray binaries are used in this thesis. It also describes the various techniques of X-ray timing and spectral measurements used throughout in this thesis.

The works done in this thesis are divided into two major subsections: Variability studies of individual systems and X-ray binary population studies.

Variability studies of individual systems

- As seen in left panel of Figure 1.7, the orbital intensity profile of GX 301–2 has three intensity regimes: the main X-ray peak occuring before the periastron passage, a second peak at apastron passage and a low intensity state called the dim phase. This complex orbital intensity profile of GX 301–2 is further investigated in detail in this thesis in **Chapter 3** by carrying out exhaustive orbital phase resolved spectroscopic measurements over multiple orbital cycles with *MAXI*–GSC . The various models describing the mode of accretion on to the compact object in GX 301–2 are then examined in light of these new results.

- Presence of an eclipse in a X-ray binary can be useful in determining orbital parameters like inclination and estimating the orbital evolution by eclipse timing method, which is done in **Chapter 4**. For the HMXB system IGR J16393–4643, we found a short eclipse in the *Swift*–BAT light-curves and employed them to constrain the orbital inclination of the system. We have also studied for the first time broadband pulsation and spectral characteristic of the system with a *Suzaku* observation, showing sub-orbital intensity variations. For the eclipsing and non-pulsing HMXB 4U 1700–37, the orbital evolution is studied using mid-eclipse times from archival as well as from long term light-curves of X-ray all sky monitors. Since no pulsations are detected in this system, it is difficult to estimate its orbital parameters, especially eccentricity. Using mid-eclipse times from 10 years of *Swift*–BAT data, we have independently constrained the eccentricity of the binary system.

X-ray binary population studies

- In **Chapter 5**, we have utilised the 16 years light-curves of X-ray binaries in 2-10 keV energy band of *RXTE*–ASM to construct the differential and integral probability distribution of count-rates. These distributions are then employed to construct multiple snapshots of X-ray binary luminosity functions of Milky Way instead of averaging the luminosities, an improvement over previous analysis by Grimm et al.

(2002), since the averaged luminosities of highly variable X-ray binaries do not represent their true positions in XLFs.

- In **Chapter 6**, the averaged spectra of X-ray binaries are investigated using long term unbiased monitoring of these sources with *MAXI*–GSC data and are used for constructing the composite X-ray spectrum. These composite X-ray binary spectra are useful in constraining the contribution of X-ray binaries in extra-galactic SEDs and will also serve as a useful input in estimating the contribution of XRB heating at high redshift IGM during Epoch of Reionisation.

In **Chapter 7**, we summarise the main conclusions of the various works carried out in this thesis and discuss some future works related to this thesis.

Chapter 2

X-ray all sky monitors and Data analysis techniques

2.1   X-ray All Sky Monitors

As mentioned in Chapter 1, the different intensity variations seen in X-ray binaries have been primarily studied by various X-ray all sky monitors in different energy bands over past few decades. X-ray all sky monitors (ASM) have a long history of monitoring the X-ray sky for new transients and their uniform coverage of the X-ray sky has led to long term variability studies of X-ray sources (Wen et al., 2006; Levine et al., 2011; Corbet & Krimm, 2013).

The first true X-ray all sky monitor was the ASM onboard the Ariel 5 rocket in 1976 which had two sets of one-dimensional scanning pinhole cameras having an effective area of 1 cm^2 and a total weight of 2 kg (Holt, 1976). All sky X-ray/gamma ray monitors like Coded Mask Imaging Spectrometer (COMIS) on board Kvant/Mir (Sunyaev et al., 1990), HETE–2 (Shirasaki et al., 2003) and *CGRO*–BATSE (Harmon et al., 2004) launched to study gamma ray bursts and X-ray binaries, had a larger field of view and monitored the sky for new transient events as well as variability of known sources.

In recent times, X-ray all sky monitors have been working as supplementary payload onboard X-ray observatories. The ASM onboard *Ginga* consisted of two collimated

gas proportional counters operating in the energy range of 1-20 keV. Some of the X-ray transients detected with *Ginga*–ASM were observed with the large area detectors onboard *Ginga* (Tsunemi et al., 1989), which has become the *modus operandi* of most of the X-ray observatories carrying ASM onboard. *BeppoSAX* carried a two coded mask proportional counters called the Wide Field Cameras, operating in the energy range of 2–30 keV and having a field of view of $20° \times 20°$ FWHM (Jager et al., 1997). The X-ray observatories Rossi X-ray Timing Explorer (RXTE), Swift and the recently launched Indian multiwavelength astronomy mission ASTROSAT carried an X-ray all sky monitor as an auxillary payload, and the appearance of a transient triggers the main detectors to carry out detail observations of the source. Monitor of All Sky X-ray Image (MAXI) is the only true X-ray all sky monitor, currently operating on the the Kibo module of the International Space Station (ISS) (Matsuoka et al., 2009).

Other than X-ray all sky monitors, various X-ray observatories carrying out large scale X-ray surveys, have also monitored X-ray binaries. While X-ray monitors revisits to the same part of the sky several times in a day to monitor variations in the fluxes of the sources or appeerence of a new transient, for X-ray surveys, the sources are monitored by either carrying out integration over a long time period ($\sim$ 1 yr) or built up from small numbers of observations of each part of the sky. Notable X-ray surveys in soft X-rays are *ROSAT* (Voges et al., 1999), hard X-rays to soft gamma rays are *Integral* IBIS/ISGRI (Bird et al., 2010; Krivonos et al., 2012) and gamma rays are *Fermi*–Large Area Telescope (LAT) (Nolan et al., 2012) and *AGILE* (Pittori et al., 2009).

In this thesis, we have used data from three X-ray all sky monitors to study long term variability patterns of X-ray binaries and they are described in the subsequent subsections. The instrument details are summarised in Table 2.1.

2.1.1 Rossi X-ray Timing: All Sky Monitors

The X-ray all sky monitor on board the Rossi X-ray Timing Explorer observatory *RXTE*–ASM had a long operational time of 16 years from 1996 to 2012 (Levine et al., 1996). It consisted of three Scanning Shadow Camera (SSC) mounted on a motorized rotation

Table 2.1: Details of X-ray all sky monitors used in the thesis. Table taken from paper by Krimm et al. (2013)

Instrument	Type	Energy range (keV)	Sky coverage (per day)	Source position resolution	1 day Sensitivity (3 σ; mCrab)
RXTE–ASM	Scanning Shadow camera	2–12	80%	5'	~ 15
Swift–BAT	Coded mask aperture	15–50	80%–90%	2.5'	16
MAXI–GSC	Slit-slat collimators	2–20	$\sim 95\%$	1.5°	9

platform. Each SSC contained a position-sensitive proportional counter (PSPC) with a slit mask on top of it. The directions of the X-ray sources and its intensities are measured by the displacements and the shadow patterns cast within the PSPC field of view of 6° by 90° FWHM. Each PSPC contained eight resistive carbon-coated quartz fiber anodes and the mask is made of aluminium. An X-ray event in the SSC yields a pair of pulse heights, which are used to compute the event energy, location in the X-ray detector and arrival direction of the event via the charge division technique. Each SSC is sensitive in the energy range of approximately 2–12 keV and had a sky coverage of 80% in every 90 minutes. The events get recorded in the series of 90 sec "dwells", in which the spacecraft maintains a fixed attitude and the ASM rotation drive is not active, so that the orientation of each SSC is fixed.

The sources in the ASM catalogue satisfy the criterion that they have reached an intensity of at least 5 mCrab in the operational time of *RXTE*–ASM and this catalogue excludes some sources like the highly absorbed, hard X-ray sources found in other catalogues like *Swift*–BAT , *INTEGRAL* etc. We have used 16 years of light-curves of X-ray binaries from *RXTE*–ASM archival data [1] for constructing X-ray luminosity functions of Milky Way in Chapter 4.

---

[1](ftp://heasarc.gsfc.nasa.gov/xte/data/archive/ASMProducts/definitive_1dwell/lightcurves/).
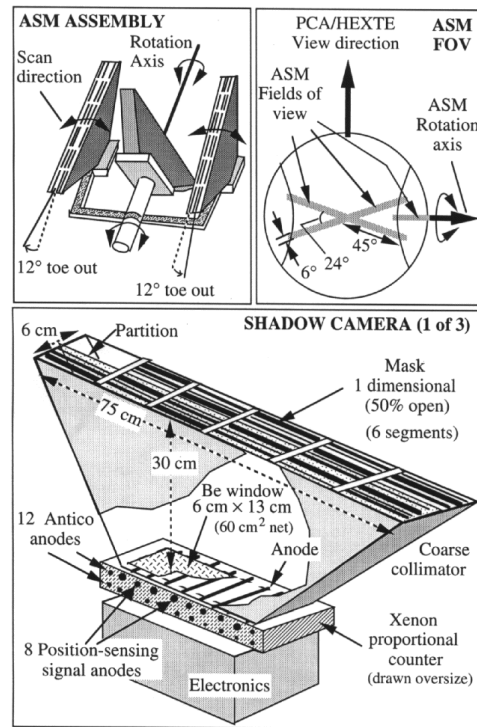
Figure 2.1: Schematic diagram of the *RXTE*–ASM *Top left*: Diagram showing the relative orientations of the SSCs on the ASM . *Top right*: The view direction of the other two RXTE instruments (PCA and HEXTE) is shown along with the ASM field of view. *Bottom panel*: Schematic diagram of one Shadow Camera showing the major components. Image taken from the paper by Levine et al. (1996).

2.1.2 Swift–Burst Alert Telescope

The Burst Alert Telescope onboard the *Swift* X-ray observatory was primarily built to detect Gamma Ray Bursts and provide a trigger to follow it up with *Swift*–X-ray telescope (XRT) and Ultraviolet/Optical Telescope (UVOT). However, due to its all sky nature of operation, it has been very useful in studying long term variabilities of X-ray binaries as well as detecting transient events like outbursts. It consists of a coded aperture mask constructed of 2.7 m^2 5×5 mm^2 lead tiles distributed in a half-filled random pattern over a 5200 cm^2 array of 4×4 mm^2 detector array of CdZnTe detectors (right panel of Figure 2.2) (Barthelmy et al., 2005; Krimm et al., 2013).

In coded mask aperture imaging technique, a coded mask *i.e* a plate with areas that are transparent and opaque to incoming photons distributed in pre-determined pattern, is placed over a position sensitive detector whose spatial resolution is matched to the spacing between 'mask elements' (in't Zand, 1992). As seen in left panel of Figure 2.2, the incoming photons cast a shadow on the detector plane and this shadow convolved with the pattern of the mask elements gives us the information about the direction of the photons and its fluxes.
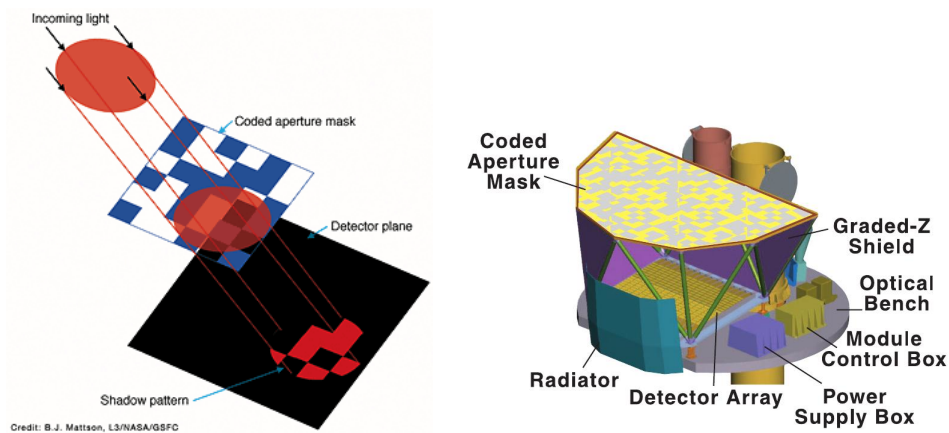
Figure 2.2: *Left Panel :* Schematic diagram showing the basic concept of coded aperture mask imaging. The incoming photons hits the mask, casting a shadow on the detector plane which is then convolved with the pattern of the coded mask to infer the direction of the photons. Image credit: B.J Mattson, NASA/GSFC. *Right Panel :* Schematic diagram of *Swift*–BAT showing the coded aperture mask and the CdZnTe detector array. Image taken from paper by Gehrels et al. (2004).

Swift–BAT operates in two modes: burst mode and survey mode. In the survey mode, the instrument collects count-rate data in 5 minute time bins for 18 energy intervals, whereas in the burst mode it switches to a photon counting mode (Gehrels et al., 2004). *Swift*–BAT operates in the energy range of 15-150 keV and has a point spread function (PSF) of 17 arcmin. The sources in the *Swift*–BAT catalogue satisfies the criteria that the source has a mean count-rate of $\geq$ 3 mCrab or a peak count-rate of $\geq$ 30 mCrab.

We have used 10 years of light-curves of X-ray binaries from *Swift*–BAT archival data [2] for eclipse measurement and mid-eclipse timing studies of two HMXBs in Chapter 3.

2.1.3 Monitor of All Sky X-ray Image

MAXI is an X-ray all sky monitor operated on the Kibo module of the International Space Station (ISS) (Matsuoka et al., 2009). It was launched by space shuttle Endeavor on July 16 2009 and saw its first light on August 3 2009. It follows the ISS orbit in which the ISS always faces the same side towards earth, so MAXI always sees the sky direction. It has 85% coverage of the entire sky in every 92 minutes of the ISS orbit. It has the best sensitivity and energy resolution amongst all operating all sky monitors. It has two instruments onboard: Solid state Slit Camera (SSC), operating between 0.7-7.0 keV (Tsunemi et al., 2010; Tomida et al., 2011) and Gas Slit Camera (GSC), operating in the energy range 2-20 keV (Mihara et al., 2011). The SSC consists of 32 X-ray CCDs, 1 square inch, 1024×1024 pixels and is the first X-ray all sky detector operating below 1 keV (left panel of Figure 2.3). The main mission of SSC is to construct all-sky X-ray maps for extended sources with better energy resolution than ROSAT maps.

The Gas Slit Camera consists of six identical units of large area position sensitive Xenon proportional counters with an instantaneous field of view of $1.5° \times 160°$. These six units are assembled into two groups : GSC–H and GSC–Z, whose field of views are pointed toward the tangential direction of the ISS motion along the earth horizon and the zenith direction respectively. The position sensitive Xe proportional counters have a slit and slat tungsten and phosphor bronze collimators (right panel of Figure 2.3). It has 1200 energy channels and the energy resolution of GSC is 18% (1 σ) at 5.9 keV (Sugizaki et al., 2011)..

We have used both archival data from GSC [3] and from MAXI on-demand processing [4] to study the long term averaged spectral properties of a large group of X-ray binaries

---

[2](http://swift.gsfc.nasa.gov/results/transients/).

[3]http://maxi.riken.jp/top

[4]http://maxi.riken.jp/mxondem/
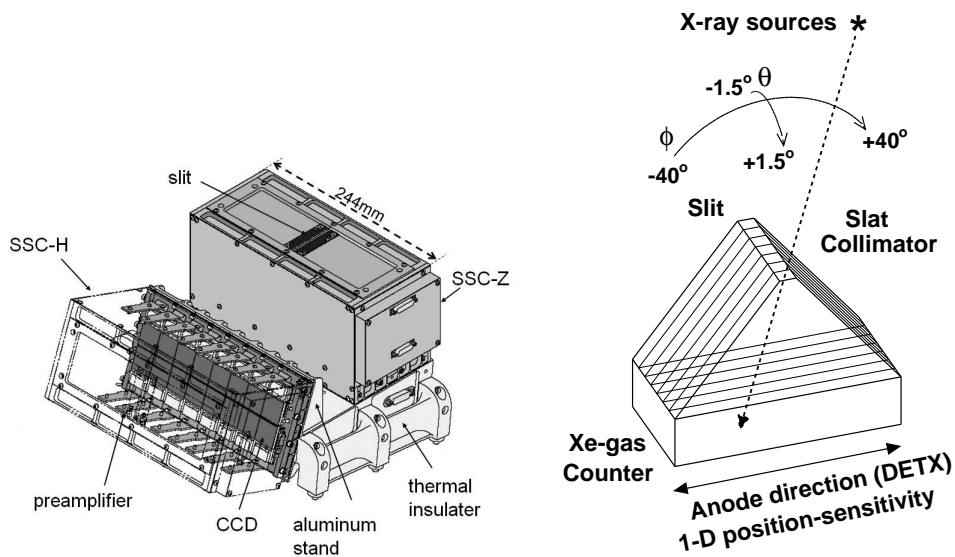
Figure 2.3: *Left Panel :* Solid state Slit Camera modules, with X-ray CCDs and slit collimators. Image taken from paper by Tomida et al. (2011). *Right Panel :* Schematic diagram of Gas Slit Camera with Xenon gas filled proportional counters and slit slat collimators. Image taken from paper by (Sugizaki et al., 2011).

in Chapter 5. We have also used *MAXI*–GSC data to study orbital resolved spectral characteristics of the HMXB GX 301–2 in Chapter 2.

2.2 Future X-ray All Sky Monitors/X-ray surveys

eROSITA or extended ROentgen Survey with an Imaging Telescope Array is an upcoming X-ray all sky survey, consisting of seven identical Wolter I type mirrors and operating in the energy band of 0.5–10 keV. To be launched in 2017, it will be more sensitive than ROSAT and will perform first imaging all-sky survey in the medium energy X-ray range up to 10 keV with an unprecedented spectral and angular resolution (Merloni et al., 2012).

Wide Field MAXI is a proposed replacement of MAXI on the ISS. The two main instruments are Soft X-ray Large Solid Angle Camera (SLC) operating in the energy band of 0.7–12 keV and Hard X-ray Monitor (HXM) operating in the energy band of 20
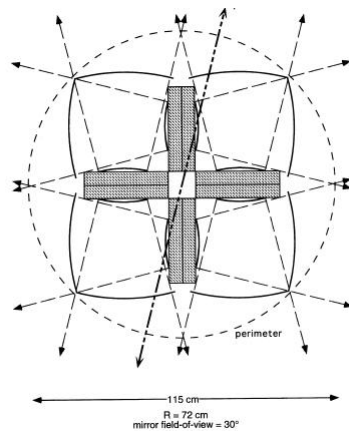
Figure 2.4: Schematic diagram of arrangement of lenses in spherical shape for lobster eye optics. Image taken from paper by Priedhorsky et al. (1996).

keV to 1 MeV (Kawai et al., 2014). The SLC will consist of four pairs of crisscross coded aperture cameras using 16 X-ray CCDs and will have a larger area than *MAXI*–SSC. The HXM will be a multi-channel array of crystal scintillators coupled with avalanche photo-diodes and will extend the energy band of the mission upto 1 MeV. The main objective of the mission is to detect X-ray transients with a position accuracy of $\sim 0.1°$ and will expect to detect electro-magnetic counterparts of gravitational wave (GW) events such as GRBs and supernovae (*e.g* core-collapse supernovae) in tandem with next generation GW telescopes such as Advanced LIGO, Virgo and KAGRA.

In a case of design inspired by nature, an optical configuration of imaging X-ray telescopes arranged in spherical geometry would achieve the 180° field of view, similar to the compound eyes of lobsters. First proposed by Angel (1979), the basic concept of the design is an array of imaging telescopes or microchannel plate devices curved into a spherical shape will have no preferred optic axis and will be able to focus equally well in all directions (Figure 2.4). Currently two X-ray all sky monitors are being developed using the X-ray lobster eyes optics: Lobster X-ray Transient Detector at NASA Goddard Space Flight Centre and Lobster All Sky X-ray Monitor at University of Leicester and will be flown as payload on the International Space Station.
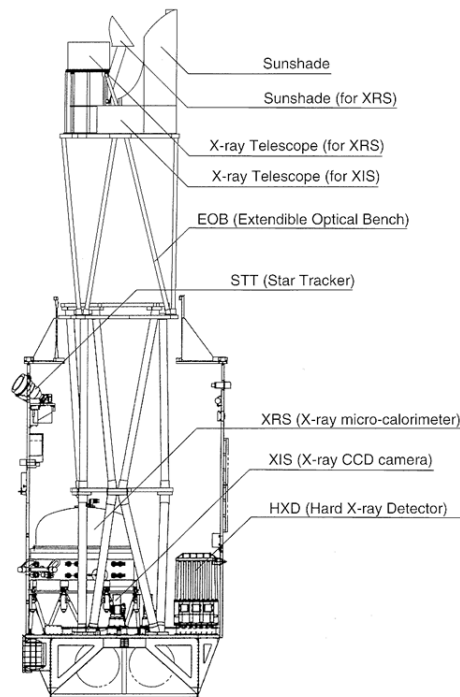
Figure 2.5: Schematic diagram the X-ray observatory *Suzaku* . Image credit: ISAS JAXA (http://www.isas.jaxa.jp/e/enterp/missions/suzaku/).

2.3 Other X-ray observatories used in this thesis

2.3.1 Suzaku

Suzaku is the fifth Japanese X-ray astronomy satellite launched in July 2005 and was operational till 2015. As shown in Figure 2.5, it consists of two sets of co-aligned scientific instruments, the X-ray Imaging Spectrometer (XIS), operating in the energy range 0.2-12 keV and Hard X-ray Detector (HXD), operating in the energy range 10-600 keV. The XIS consists of three front illuminated CCD detectors and one back illuminated CCD detector (Koyama et al., 2007), out of which three CCDs XIS0, XIS1 and XIS3 are currently operational. The CCD devices were located at the focus of four gold coated grazing-incidence reflective optics X-ray telescopes (XRTs) consisting of tightly nested, thin-foil conical mirror shells.

The HXD consists of silicon PIN diodes operating in energy range 10-70 keV and GSO

crystal scintillators extending the energy range till 600 keV (Takahashi et al., 2007). It is a non-imaging collimated instrument and consists of 16 identical detector modules arranged in 4×4 array. Each unit is composed of two detector layers at the bottom of a passive collimator consisting of a GSO/BGO phoswich scintillator, sensitive above $\sim$ 30 keV and a 2 mm thick PIN silicon diode on top of it, sensitive below $\sim$ 60 keV. The scintillator signals from GSO/BGO are read out by photomultiplier tubes located below the crystals. The effective area of HXD is energy dependent with ~ 160 cm^2 at 20 keV and ~ 260 cm^2 at 100 keV and the time resolution is 61 μs.

2.4 Data analysis techniques

The timing and spectral analysis carried out in this thesis has extensively used HEAsoft, which comprises of full set of softwares like FTOOLS (required for manipulation of the fits files), XRONOS (timing analysis software) and XSPEC (spectral analysis software). The description of some of the timing and spectral analysis tools used in this thesis are given in following subsections.

2.4.1 lcurve

The tool 'lcurve' produces time-series of intensity or binned light-curves of the input event file. It can poroduce upto 4 simultaneous energy (count-rate) time series and can be used to construct hardness or colour-colour diagrams. The output of the lcurve file is time and count-rate along with its errors.

2.4.2 efsearch

The tool 'efsearch' searches for periodicities in a time series by folding data over a range of periods, determines the chi-square of the folded lightcurve and plots the chi-square values versus the periods with the best period found in the analysis. This task is used to estimate the orbital period and pulse period of some X-ray binaries in this thesis.

2.4.3 efold

The tool 'efold' folds the lightcurves using the supplied period and plots the output. It can plot up to 4 simultaneous lightcurves folded with the same period and can also calculate the ratios and sums of the lightcurves over the folded period. This task is used to produce orbital intensity profiles and pulse profiles of some X-ray binaries in different energy bands in this thesis.

2.4.4 XSPEC

X-ray Spectral Fitting Package or XSPEC is used extensively in this thesis for spectral fitting of X-ray binaries. The basic principle of spectral fitting is: If the spectrometer measures photon counts C within the instrument channels I, the observed spectrum is related to actual spectrum of the source $f(E)$ by the following relation

$$C(I) = \int_0^\infty f(E)R(I,E)dE. \tag{2.1}$$

where $R(I,E)$ is the instrumental response and is proportional to the detection probability of an incoming photon of energy E in Channel I. The "forward folding technique" is used for spectral fitting in X-ray astronomy because of the non-invertable nature of the $R(I,E)$ matrix. We choose a model $f(E)$ for the source spectrum, and match, or "fit it to the data obtained by the spectrometer. For each model spectra, a predicted count spectrum C_p is calculated and compared to the observed data $C(I)$ and a fit statistics like χ^2 statistics is obtained to check of goodness of fit and best fit parameters of the model.

χ^2 statistics is defined as $\chi^2 = \frac{\sum(C(I)-C_p(I))^2}{(\sigma(I))^2}$ where $\sigma(I)$ is the error associated with each count Count(I). The χ^2 is estimated for a certain number of degrees of freedom ν given by number of channels minus the number of model parameters. In general a fit is said to be satisfactory if the reduced χ^2_{red} $(\frac{\chi^2}{\nu})$ is ~ 1.

Chapter 3

Orbital phase resolved spectroscopy of GX 301–2[1]

3.1 Introduction

GX 301–2 is a High Mass X-ray Binary (HMXB) system with an X-ray pulsar and a B-emission line hypergiant star (B1 Ia+) WRAY 977. The orbital period of the binary system is $\sim$ 41.5 days and the neutron star has a large spin period of $\sim$ 685 s (Koh et al., 1997). The distance to the binary system is estimated to be $\sim$ 3.1 kpc (Coleiro & Chaty, 2013a). The orbital parameters of the binary was measured by pulse timing analysis and it was found to be to be a highly eccentric binary system with $e = 0.462$ (Sato et al., 1986; Koh et al., 1997). The orbit of GX 301–2 is shown in Figure 3.1, where the occurence of flare and the line of sight are pointed out.

The orbital characteristics of GX 301–2 have been extensively studied with various X-ray instruments in different energy bands ($CGRO$–BATSE (15-55 keV) - Koh et al., 1997) ($RXTE$–ASM (2-12 keV) - Pravdo & Ghosh, 2001; Leahy, 2002; Leahy & Kostka, 2008) ($SuperAGILE$ (20-60 keV) - Evangelista et al., 2010). As shown in the left panel of Figure 1.7 in Chapter 1, the orbital intensity profile has three intensity regimes: bright phase during X-ray flare (pre-periastron passage around orbital phase 0.95), dim or low

---

[1]The work presented in this Chapter is published as a paper (2014, MNRAS, 441, 2539)
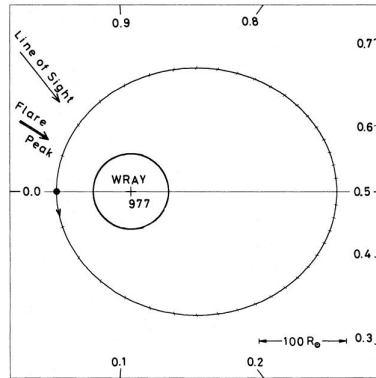
Figure 3.1: Schematic diagram of the orbit of GX 301–2 taken from Sato et al. (1986).

intensity phase (after periastron passage around orbital phase 0.15-0.3) and intermediate intensity phase (during the apastron passage around orbital phase 0.5) (Koh et al., 1997; Leahy, 2002). A strong X-ray flare occurs before the periastron passage as well as a medium intensity peak is observed at the apastron passage, indicating accretion onto the neutron star due to both spherical stellar wind along with a possible equatorial disk or accretion stream (Sato et al., 1986; Stevens, 1988; Haberl, 1991; Layton et al., 1998; Pravdo & Ghosh, 2001; Leahy & Kostka, 2008).

The X-ray spectrum of GX 301–2 have been studied in different orbital phases with *TENMA* (Leahy & Matsuoka, 1990), *ASCA* (Saraswat et al., 1996; Endo et al., 2002), *RXTE*– PCA (Mukherjee & Paul, 2004), *Chandra* (Watanabe et al., 2003), *BeppoSAX* (La Barbera et al., 2005), *XMM-Newton* (Fürst et al., 2011) and *Suzaku* (Suchy et al., 2012). It has a highly absorbed X-ray spectrum with a partial covering high energy cutoff power-law component and several emission lines. A soft excess component is found in the X-ray spectrum from *EXOSAT* and *ASCA* observations (Haberl, 1991; Saraswat et al., 1996). GX 301–2 has a very high line of sight photo-electric absorption, which is attributed to the dense circumstellar environment in which the neutron star moves. The column density varies strongly with orbital phase with certain amount of clumpiness attributed to the stellar wind (Pravdo & Ghosh, 2001; Mukherjee & Paul, 2004; Leahy & Kostka, 2008). A prominent Fe Kα line is found to exist in almost all orbital phases of GX 301–2. This fluorescence line is produced due to reprocessing of X-ray photons

from the pulsar by the circumstellar matter and sometimes shows evidence of a Compton recoil (Watanabe et al., 2003).

The equivalent width of the Fe Kα line depends on the quantity and distribution (geometry and column density) of the surrounding matter (Inoue, 1985; Makino et al., 1985; Makishima, 1986; Leahy & Creighton, 1993; Kallman et al., 2004). Therefore, by comparing the equivalent width of Fe Kα line with N_H, we can study the distribution of circumstellar matter around the neutron star at different orbital phases. This can be further used in examining the various accretion models of GX 301–2, in which the accretion rate and the reprocessing environment have strong orbital phase dependence. In this work, we have investigated the accretion phenomena in GX 301–2 using the orbital variation of column density of absorbing matter and the relation between the line equivalent width and N_H as observational parameters. For such studies, it is very useful to have long term orbital light-curves and spectrum measured at different orbital phases with uniform phase coverage. The Monitor of All Sky X-ray Image (*MAXI*), which has both all sky coverage and moderate energy resolution, is well suited for detailed studies of the orbital light-curves and the orbital phase resolved spectrum of bright X-ray sources.

In this Chapter, we have used light curves of GX 301–2 in the 2-20 keV energy range obtained over four years with the *MAXI*–GSC to create multi-band orbital intensity profiles. From spectroscopic analysis of the *MAXI* data with unprecendented orbital coverage for many orbits continuously, we have measured the orbital dependence of the absorption column density and equivalent width of the Fe Kα line. The orbital phase dependence of the column density and the line equivalent width are then used to examine the various models about the distribution of circumstellar matter and the mode of accretion onto the neutron star in GX 301–2.

3.2   Accretion models

The radiation driven spherical wind from the hypergiant star WRAY 977 (Castor et al., 1975) cannot account for the asymmetric orbital intensity profile of GX 301–2. The two
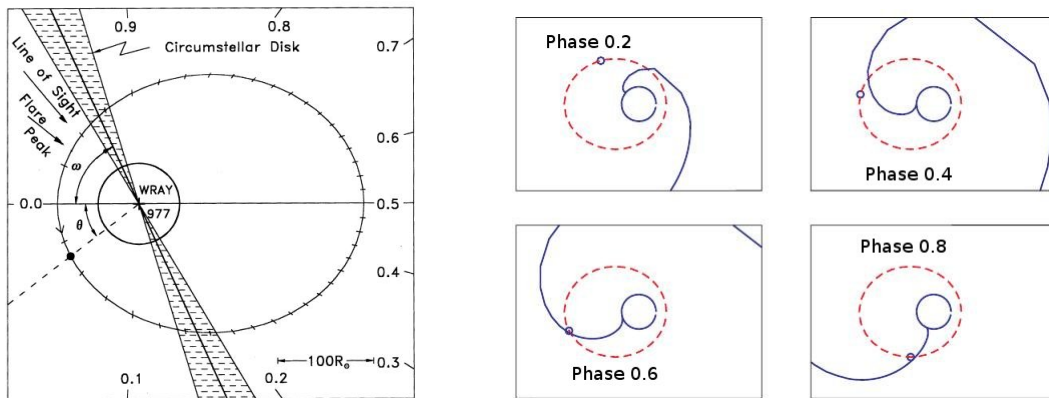
Figure 3.2: Accretion models of GX 301–2. *Left Panel :* Tilted circumstellar disk shown in the orbit of GX 301–2. Figure taken from Pravdo & Ghosh (2001). *Right Panel :* High density accretion stream following the NS along the orbit of GX 301–2. Figure taken from Leahy & Kostka (2008).

main accretion models proposed for this system are mentioned below.

3.2.1 Circumstellar disk model

Pravdo & Ghosh (2001) proposed the presence of a tilted circumstellar disk around the WRAY 977 star to explain the orbital profile of GX 301–2, as shown in left panel of Figure 3.2. The NS star passes through the dense circumstellar disk during its orbit and accretes matter at a much higher rate than it does for the rest of the orbit through the low-density, high-velocity wind from WRAY 977.

3.2.2 Accretion stream model

Leahy & Kostka (2008) proposed the presence of the high density accretion stream in the system along with the stellar wind from WRAY 977. As shown in right panel of Figure 3.2, in this model, the high density accretion stream follows the orbit of NS like a garden hose and the NS star periodically passes in and out of the stream.

3.3 Data and Analysis

3.3.1 Energy resolved orbital intensity profiles

We have first used 16 years long light-curve of GX 301–2 obtained with *RXTE*–ASM in 2-12 keV energy band to estimate the orbital period of the system (P_{orb}=3584304 s; consistent with Koh et al. (1997)). We have then folded the *MAXI*–GSC light curves of GX 301–2 obtained during MJD:55064 to 56502 with the orbital period obtained from *RXTE*–ASM to obtain energy resolved orbital intensity profiles. The orbital phase reference is taken from Koh et al. 1997, with the phase zero corresponding to periastron passage. The orbital intensity profiles in the *MAXI*–GSC energy bands of 2-4 keV, 4-10 keV and 10-20 keV are shown in Figure 3.3 along with hardness ratios (4-20 keV / 2-4 keV and 10-20 keV / 4-10 keV) of photons. The orbital modulation is most pronounced in the highest energy band of 10-20 keV showing the pre-periastron X-ray flare as well as the intermediate intensity apastron peak. In the lowest 2-4 keV energy band, instead of a strong flare, a sinusoidal modulation in intensity can be seen. This smoothly varying soft X-ray profile is seen for the first time in GX 301–2 with the *MAXI*–GSC data. As seen in Figure 3.3, there is an increase in the 4-10 keV photons after the apastron passage, which is reflected in the low hardness ratio values of counts in 10-20 keV and 4-10 keV energy band around orbital phase 0.5-0.8.

3.3.2 Orbital phase averaged spectrum

We have extracted the orbital phase averaged spectrum of GX 301–2 with *MAXI*–GSC for the same observation duration using the *MAXI* on-demand data processing [2]. The orbital phase averaged spectrum is modelled with a power-law with a high energy cut-off modified by photo-electric absorption by column density of absorbing material along our line of sight. The spectral analysis is performed using XSPEC v:12.6. Though the broadband X-ray spectrum of GX 301–2 is known to have a partial covering absorption

---

[2]http://maxi.riken.jp/mxondem/
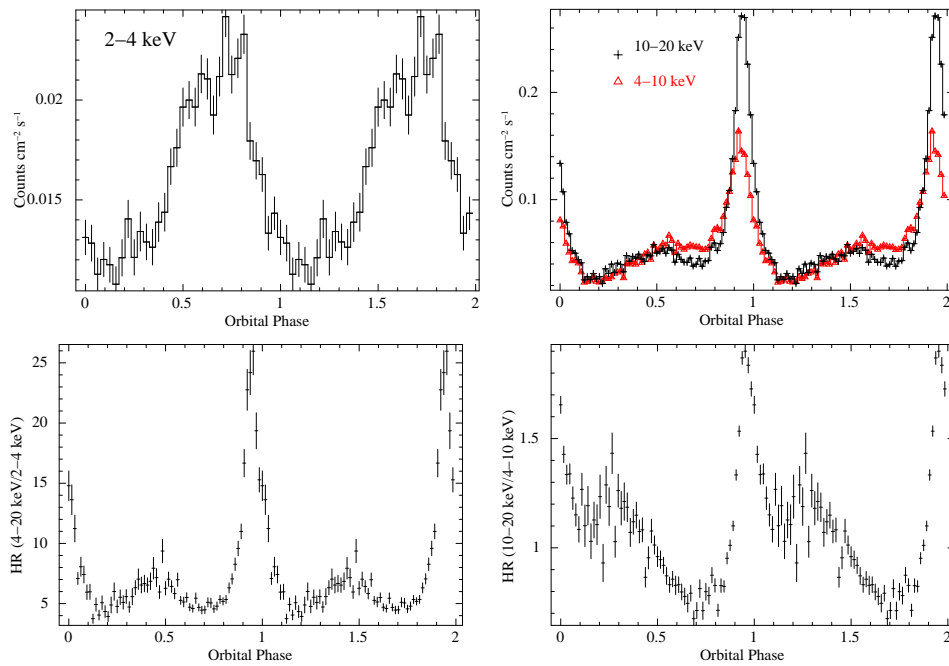
Figure 3.3: The top left panel is the orbital intensity profile of GX 301–2 in 2-4 keV energy band of *MAXI*–GSC . The top right panel is the orbital intensity profile in 4-10 keV (red triangles) and 10-20 keV (black cross) energy band. The bottom left panel is the hardness ratio (HR) of the counts in 4-20 keV energy band to low energy 2-4 keV band. Lower right panel is the hardness ratio (HR) of counts in 10-20 keV and 4-10 keV energy band.

(Mukherjee & Paul, 2004; Suchy et al., 2012; La Barbera et al., 2005), in the limited energy band of the GSC, it was not required to include partial covering absorption in the spectral model. A Fe Kα fluorescence line present in the spectrum is modelled with a single gaussian line. The analysis is carried out by fitting the spectrum from energy range 3.5 keV to 20 keV to a model consisting of a power-law with a high energy cut-off and a single gaussian line. When this fit was extended to lower energies till 2.0 keV, a low energy excess was found in the spectrum. This low energy excess was modelled by an unabsorbed blackbody component by freezing all other parameters of the previous best fit model. The motive behind modelling the low energy excess by an unabsorbed blackbody is to only estimate the flux of the low energy excess and not to derive a blackbody temperature and size of the region since the data below 3.5 keV has limited statistics. The orbital phase averaged X-ray spectrum along with the best fit model components is shown in Figure 3.4, along with the presence of soft excess, which is then modelled by a blackbody component. The reduced χ^2 for the phase averaged spectrum shown in Figure 3.4 is 0.99 for 352 degrees of freedom.

3.3.3 Orbital phase resolved spectra

Strong variations of the hardness ratio of photons in 10-20 keV energy band and 4-10 keV energy band with the orbital phase shown in Figure 3.3 indicates significant changes in the overall spectrum. Many observations of GX 301–2 have been carried out at different orbital phases in the past (Endo et al., 2002; Mukherjee & Paul, 2004; La Barbera et al., 2005; Suchy et al., 2012), but with uneven phase coverage. Long term orbital coverage of GX 301–2 with MAXI smears out short time scale variations and long term behaviour of the source remains. We have performed an orbital phase resolved spectral analysis of GX 301–2, by using the arbitrary grouping of the individual scans allowed by *MAXI* on demand data processing (Nakahira et al., 2012; Doroshenko et al., 2013). Using the orbital ephemeris, we extracted the start time and end time for different orbital phase bins, and extracted the spectra for each orbital phase with data from multiple orbital cycles by grouping the individual scans. We have chosen 21 independant orbital bins,
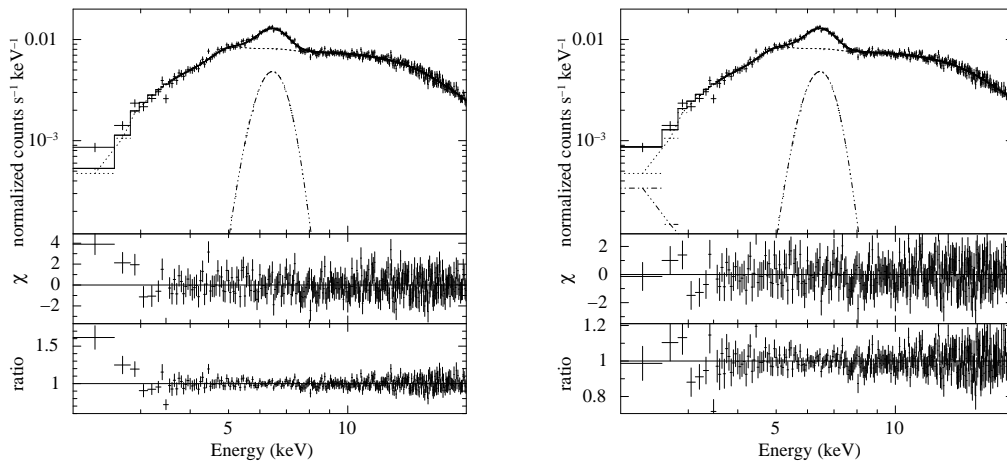
Figure 3.4: The orbital phase averaged X-ray spectrum is shown along with the best fit model components (top panel), contributions of the residuals to the chisquare (middle panel) and ratio between data and the model (bottom panel) in the 2-20 keV band. The best fit model is obtained in the energy range 3.5-20 keV and is extended to 2 keV. The left panel shows the presence of a soft excess and the right panel shows the fit after modelling the soft excess with a blackbody component.

with the bin size chosen such that it can constrain the Fe line parameters. The effective exposure times varies from 43 kilosec for the orbital bins near the X-ray peak to 454 kilosec for orbital bins near dim phase.

In this work, we have fitted these 21 orbital phase resolved spectra with two models: a power-law continuum, with and without a high energy cut-off. For the spectral fits with a high energy cut-off, the value of cut-off energy and fold energy (E_c and E_f) was frozen to the orbital phase averaged values of 15 keV and 18.6 keV respectively, since the parameters of the high energy cut-off cannot be constrained well in the phase resolved spectra. A Fe fluorescence line was found in all the orbital phases which was modelled by a single gaussian line. For both the spectral models, the spectra were fitted from energy range 3.5 keV to 20 keV and then the fit was extended to lower energies till 2.0 keV. For some orbital phases near the X-ray peak, a low energy excess is found to be present in the spectra. Ratio of the data and the model without including a component for the soft excess are shown in Figure 3.5 for both the spectral models. To only estimate the flux in the soft excess, we have modelled the low energy excess with an unabsorbed blackbody component. The range of χ_ν^2 values, after accounting for the low energy excess, is 0.8-1.16 (0.75-1.23) for a power-law with high energy cut-off (without the high energy cut-off). The orbital phase resolved X-ray spectra for all the 21 orbital phase bins along with the best fit power-law model is shown in Figure 3.6.

The orbital dependance of the spectral parameters photon index Γ, column density of absorbing matter along our line of sight N_H, flux and equivalent width of Fe line emission, total flux of the system in the entire 2-20 keV energy band of *MAXI*–GSC and ratio of flux included in the low excess to the total flux of the system, for both the spectral models are shown in the Figure 3.7. The errors on the spectral parameters Γ, N_H and flux of Fe line emission are at 90% confidence level whereas the errors on equivalent width of Fe line is shown at 1σ confidence level. The errors on the relative flux in the low energy excess, modelled by a blackbody is taken at 1σ confidence level of blackbody normalisation. Since the high energy cut-off affects the X-ray spectrum only above 15 keV, therefore the two results shown in Figure 3.7 with and without the high energy
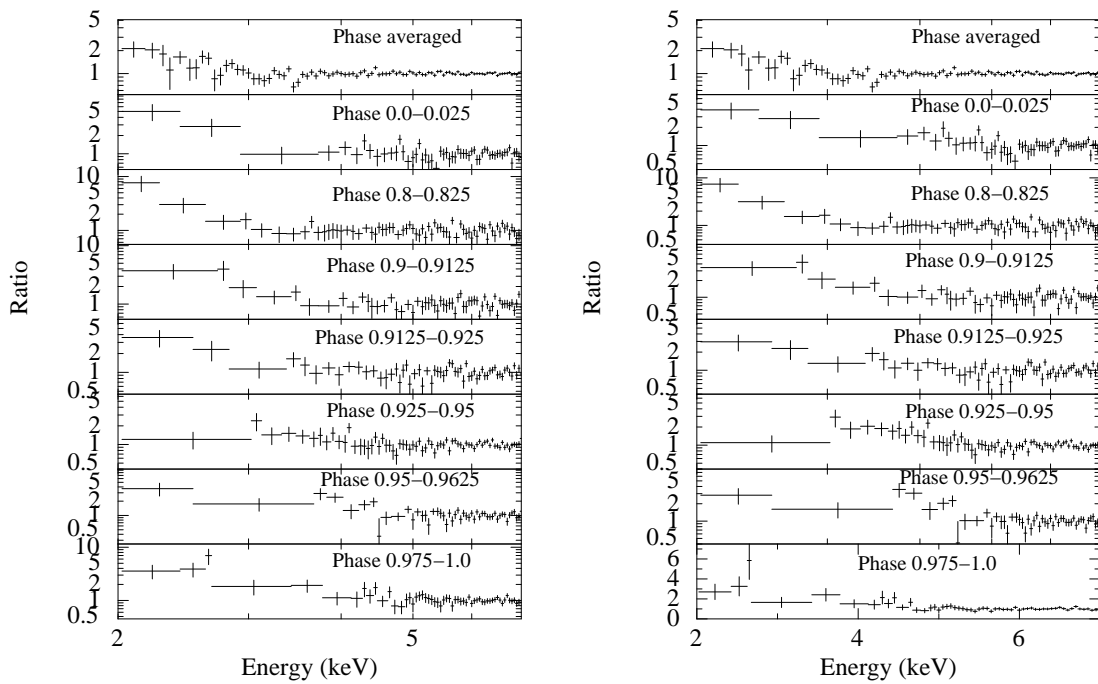
Figure 3.5: Ratio plot of data in the 2-20 keV band and the best fit model in the 3.5-20 keV extended to 2 keV, showing the low energy excess in some orbital phases with both power-law with high energy cut-off model (right panel) and power-law model (left panel). The phase averaged low energy excess is using a power-law with high energy cut-off model.
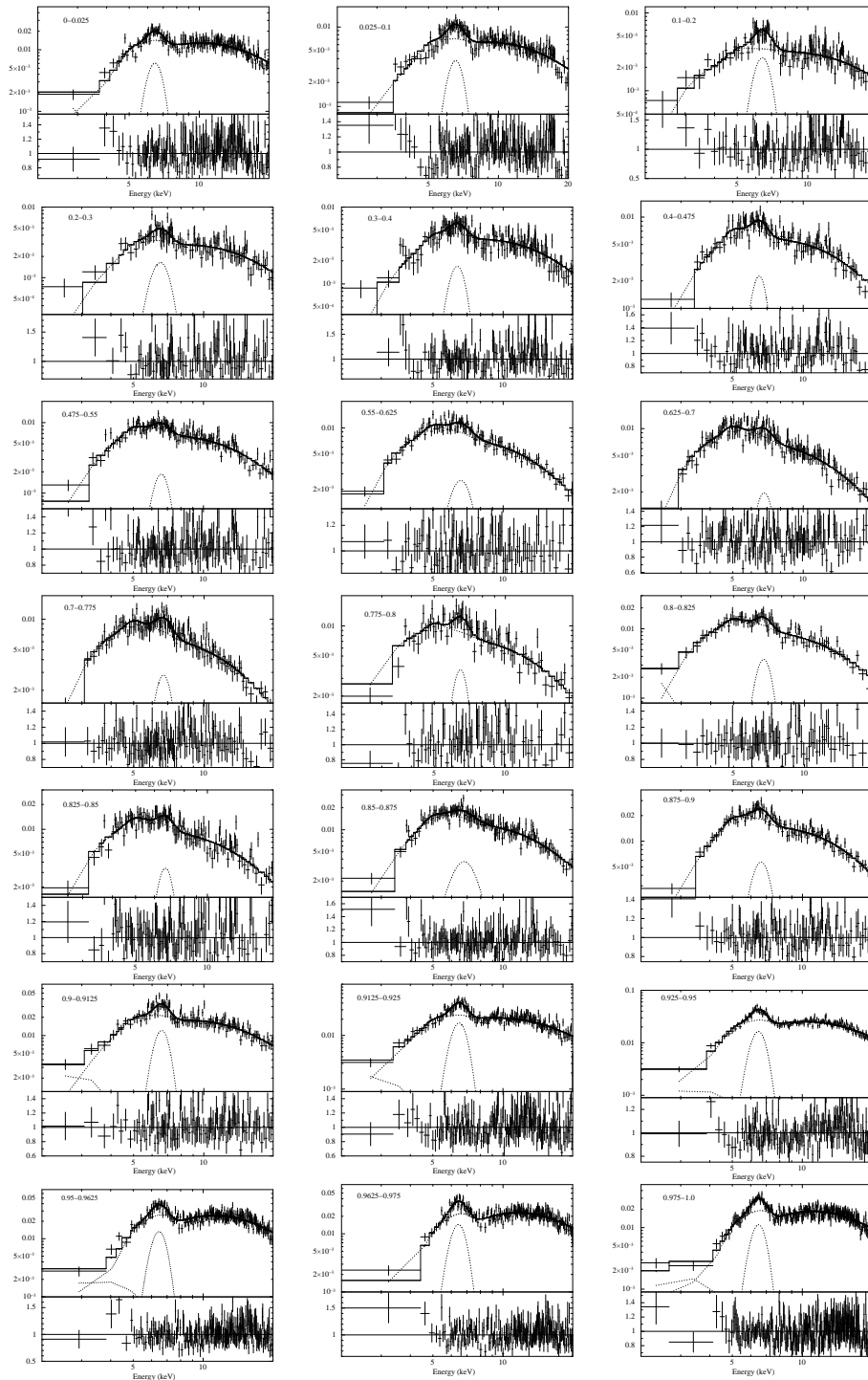
Figure 3.6: The orbital phase resolved X-ray spectra for 21 orbital phase bins are shown along with the best fit power-law model and the ratio between data and the model in the 2-20 keV energy band.
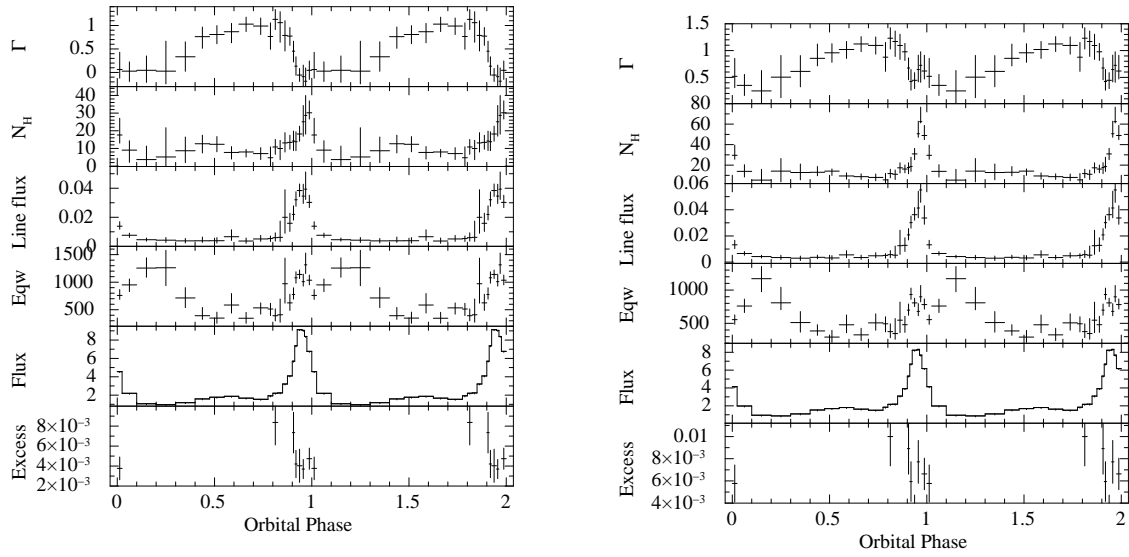
Figure 3.7: Variation of Photon index (Γ), equivalent column density of hydrogen (N_H in units of 10^{22} cm^{-2}), Line flux of Fe Kα (in units of photons cm^{-2} s^{-1}), Equivalent width of Fe Kα line (Eqw in units of eV), Flux of source (F in the units of 10^{-9} ergs s^{-1} cm^{-2} and in the energy band of 3.5 – 20 keV) and the ratio of flux in the low energy excess modelled by a blackbody to the total flux of the system (Excess) for both the spectral models: power-law with a high energy cut-off (left panel) and a power-law (right panel).

cut-off included in the spectral model show similar pattern of variation of the spectral parameters.

The orbital variation of column density of absorbing matter along our line of sight N_H and flux of Fe line emission for both the spectral models follows the orbital variation of the flux of the system. However, orbital variation of power-law photon index and equivalent width of Fe line follows a different pattern from the flux of the system. The power-law photon index Γ is lowest at the dim phase and at the pre-periastron X-ray flare. The Fe line equivalent width shows two peaks, one at the pre-periastron X-ray flare and the other around dim phase 0.1–0.3. The soft excess is detected only near the X-ray flare and has a flux that is less than 1.0% of the continuum flux.

Three of the phase resolved X-ray spectra showing the highest equivalent width of Fe line (dim phase : 0.1-0.2), lowest equivalent width (intermediate phase: 0.475-0.55) and
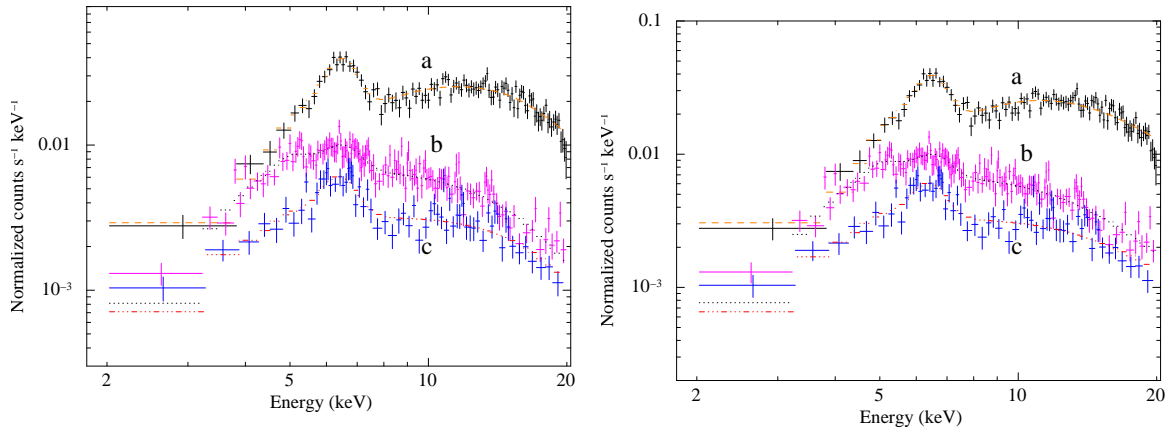
Figure 3.8: The spectra and the best fitted model are shown here for three different orbital phases: the pre-periastron X-ray flare (a), the apastron passage which has the lowest equivalent width of the iron line (b) and the dim phase which has the highest width of the iron line (c), for both the spectral models, i.e power-law with a high energy cut-off (left panel) and power-law model(right panel).

at pre-periastron flare (phase 0.95) are shown in Figure 3.8.

3.4 Discussions

3.4.1 Multi-band orbital modulation

Figure 3.3 shows the orbital intensity profiles of GX 301–2 in 2-4 keV, 4-10 keV and 10-20 keV energy bands of *MAXI*, along with the hardness ratios of photons in 4-20 keV energy band to 2-4 keV energy band and 10-20 keV energy band to 4-10 keV energy band. We have detected a strong, nearly sinusoidal, modulation by a factor of ~ 2.5 in the 2-4 keV energy band, the profile of which is different from the orbital modulation in the 4-20 keV band. In the entire 4-20 keV band and other sub-bands (4-10 keV and 10-20 keV), the source shows an appreciable orbital modulation, as previously known, with a strong pre-periastron X-ray flare as well as an apastron peak. The hardness ratio between the 10-20 and 4-10 keV bands shows the pre-periastron X-ray flare to be hard which is also reflected in small value of the power-law photon index at the phase ~ 0.95

(Figure 3.7). After the apastron passage and before the hard X-ray flare (orbital phase range 0.55-0.85), there is a decrease seen in the hardness ratio. A corresponding high value of the power-law photon index Γ is seen in the Figure 3.7.

3.4.2 Variation of spectral parameters with orbital phase

We have studied the orbital dependence of different spectral parameters of GX 301–2 using a power-law continuum model with and without a high energy cut-off. Figure 3.7 shows the orbital variation of Γ, N_H, flux and equivalent width of Fe fluoresence line, total flux of the system and ratio of flux included in the low excess to the total flux, for both the spectral models. From Figure 3.7, the orbital variation in spectral parameters for both the models show very similar trend. The photon index gradually increases from a low value of 0.05 for power-law with high energy cut-off (0.3 for power-law) model at the dim orbital phase 0.1-0.3, to 1.1 for both the models at the periastron passage, just before the X-ray flare. The spectrum is found to be hard at dim phase 0.1-0.3 for both the models. Spectral hardening at this phase was reported in earlier works using data from *RXTE*–ASM and *SuperAGILE* (Pravdo & Ghosh, 2001; Evangelista et al., 2010).

The column density N_H is found to vary with a pattern similar to the flux of the system, indicating a possible origin of flare due to increased mass accretion at the orbital phase of ~ 0.95. The absorption column density is in the range of 10-20 $\times 10^{22}$ cm^{-2} during most of the orbit, except near the flare. Since the data from *MAXI*–GSC is averaged over multiple orbital cycles, clumpiness in wind as seen in *RXTE*–PCA data over one cycle (Mukherjee & Paul, 2004) and *BeppoSAX* data over one cycle (La Barbera et al., 2005), is not detectable in the *MAXI*–GSC data and a partial covering absorption is not required to fit the X-ray spectra obtained with *MAXI*–GSC . The flux of Fe line emission also shows a strong increase during the flare, by a factor of ~ 3, compared to the nearly constant flux in the orbital phase range 0.1-0.8.

The orbital variation of equivalent width of Fe line shows a markedly different trend as compared to the orbital variation of column density and total flux of the system. The highest equivalent width occurs at the dim phase of 0.1-0.3 which also has lowest N_H

along the line of sight. This different pattern of orbital variation of equivalent width and the column density N_H provides us important clues about the distribution of matter around the system, which is discussed further in the next section.

A low energy excess, contributing to less than 1.0% of the continuum flux, is found in the spectra at orbital phases near the pre-periastron X-ray flare as shown in the bottom panels of Figure 3.7. Low energy excesses in the X-ray spectrum of GX 301–2 has been previously reported by Haberl (1991) using *EXOSAT* observation and Saraswat et al. (1996) using *ASCA* observation. Due to high value of N_H around the X-ray flare, we rule out the possible origin of low energy excess from the surface of the neutron star (Hickox et al., 2004). A possible origin of this low energy excess could be due to the X-ray shocks in the system when the high density accretion stream interacts with the stellar wind from WRAY 977 (Haberl, 1991; Kaper et al., 2006).

3.5   Orbital modulation: wind diagnostics

3.5.1   Column density as tracer

Figure 3.9 shows the orbital variation of the column density of absorbing matter along our line of sight obtained in this work with *MAXI*–GSC for both a power-law with a high energy cut-off model and a power-law model and is compared to the predicted orbital variation of N_H expected from Pravdo & Ghosh (2001) and Leahy & Kostka (2008) models. These models were developed to describe the orbital intensity profile of GX 301-2 as seen with *BATSE* (Pravdo & Ghosh, 2001) and *RXTE*–ASM (Leahy & Kostka, 2008). For the sake of comparison with the measured orbital profile of the column density, we have normalised the highest column density predicted by these models to the highest observed column density.

The Pravdo & Ghosh (2001) model predicts an enhanced column density twice, at the pre-periastron X-ray flare and at the dim orbital phase. However, only one peak in column density is observed with *MAXI*–GSC during pre-periastron passage. The Leahy & Kostka (2008) model underestimates the value of column density at the pre-periastron
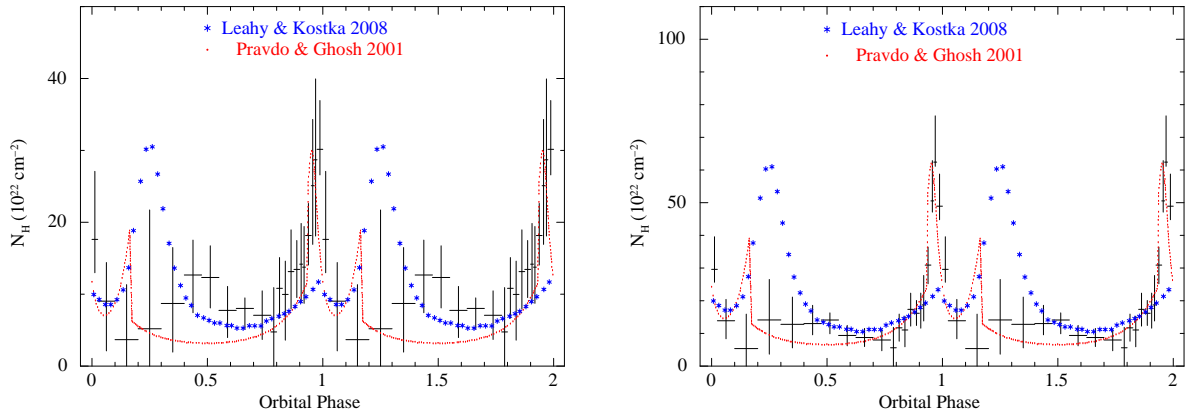
Figure 3.9: Variation of column density N_H as function of orbital phase of GX 301-2 for both power-law with high energy cut-off (left panel) and power-law model (right panel), overlaid on the predicted orbital variation of column density (circles - Pravdo & Ghosh 2001, asterisks - Leahy & Kostka 2008). The predicted orbital variation of column density is normalised to the highest column density found in our results for the sake of comparing with the observed orbital profile.

phase but predicts a large increase in column density around phase 0.2. On the other hand, the *MAXI*–GSC spectra do not show an enhanced column density at orbital phase 0.1-0.3 predicted by both the models. A possible explanation for this would be that the absorbing matter is situated away from the line of sight at this phase range. To further investigate this possibility, we have used the orbital variation of the equivalent width of the fluorescent iron line in the next section as an additional observational signature to study the orbital distribution of circumstellar matter around the neutron star in GX 301–2.

3.5.2 Iron line as tracer

The iron fluorescence line provides important information on the geometry and density of the line producing region around the central X-ray source that produces the continuum X-ray emission (Makishima, 1986). In HMXBs, the fluorescence lines originate from the dense absorbing material present in the stellar wind. The detection of a Compton
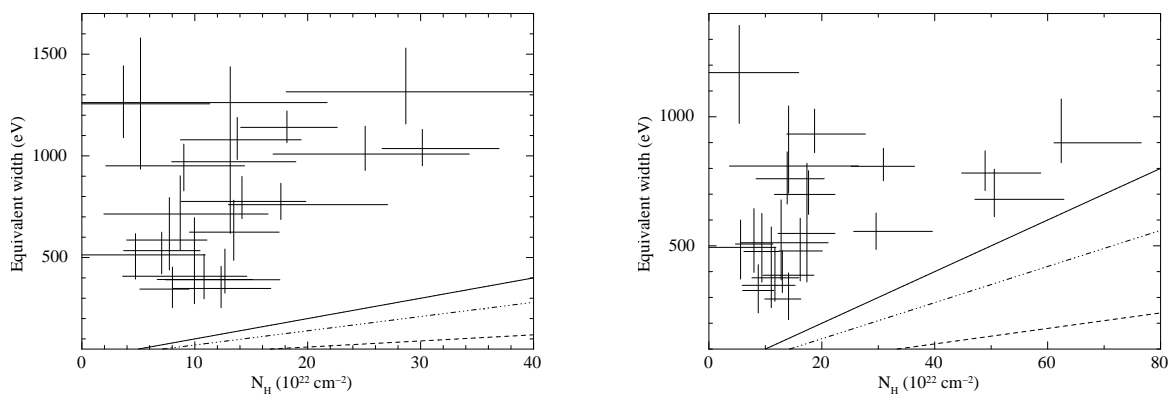
Figure 3.10: Plot of equivalent width of Fe Kα versus absorbing column density N_H obtained for different orbital phases with *MAXI*–GSC for both power-law with highecut (left panel) and power-law model (right panel). Solid line represents the relation between equivalent width and column density of absorbing matter for an isotropically distributed matter for $\Gamma \sim 1.1$ calculated by Inoue (1985). The dashed line and dot dashed line is the relation between equivalent width and column density for a spherical shell of gas for $\Gamma \sim 1$ and $\Gamma \sim 0.2$ respectively calculated by Kallman et al.(2004). $\Gamma \sim 0.2$ corresponds to the hardest spectrum seen in the dim phase with *MAXI*–GSC , where the highest value of equivalent width is found.

shoulder of Fe Kα in GX 301–2 by Watanabe et al. (2003) confirms the presence of Compton thick matter around the X-ray source. The equivalent width of the Fe line is expected to be linearly correlated to the column density for an isotropically distributed cold matter (Inoue, 1985; Kallman et al., 2004). Deviation from this linear correlation can be mostly attributed to any anisotropic configuration of the reprocessing matter around the X-ray source. The relation between the equivalent width of the iron line and the absorbing column density has been used to study the precessing accretion disk in LMC X–4 and Her X–1 (Naik & Paul, 2003, 2004).

Figure 3.10 shows a plot of equivalent width of the iron line against the absorbing column density N_H in different orbital bins for GX 301–2 in this work for both the spectral models. In certain orbital phases, we do see very high equivalent width ($\sim$ 1 keV) along with a small value of column density ($\sim$ 2-5 $\times 10^{22}$ cm^{-2}). These observations highly deviate from the relation expected for an isotropically distributed gas (Inoue, 1985; Kallman et al., 2004) and instead there seems to exist high anisotropicity in the distribution of circumstellar matter around the X-ray pulsar, especially in some orbital phases. These results are in contrast to the study of equivalent width versus N_H by Makino et al. (1985); Endo et al. (2002); Fürst et al. (2011), where they found a linear correlation between equivalent width and column density, thereby favouring a spherical shell model of gas distribution. However, such studies were carried out in narrow window of pointed observations and this work is carried by averaging over multiple orbital cycles of GX 301–2.

From orbital variation of N_H and equivalent width shown in Figure 3.7, we see a very high equivalent width along with a very low line of sight column density at orbital phases 0.1-0.3. This being an important outcome of the present work and the fact that it is hardest to measure absorption column density in the dim phase, we have further examined it. As the *MAXI*–GSC spectrum has very little count-rate below 3 keV, we carried out the spectral analysis above 3.5 keV and an upper limit on N_H of 11 $\times 10^{22}$ cm^{-2} is obtained at the orbital phase 0.1-0.3 with a 90% confidence limit. Near the flare phase, the spectrum has higher statistics and the best fit model for the spectrum above

3.5 keV, when extended to the lower energy band, clearly shows the presence of a soft excess. The blackbody temperature of the soft excess measured in these phases is in the range of 0.1-0.3 keV and this component does not have any significant contribution in the GSC spectrum above 3.5 keV. Therefore, the value of N_H measured at different orbital phases (especially at dim phase of 0.1-0.3) represents the true line of sight value of N_H. A possible explanation would be that the distribution of circumstellar matter in these orbital phases somehow avoids the line of sight and the possible geometries could be the ones in which the reprocessing region (where the Fe fluorescence line is produced) is situated behind the neutron star or on one side of the neutron star away from the line of sight. The optical studies of GX 301–2 done by Kaper et al. (2006) confirms the presence of gas stream trailing the X-ray pulsar around the orbital phases 0.18-0.34. This would also be a possible explanation for the absence of second peak in the orbital distribution of N_H, though it is predicted by both the circumstellar disk model (Pravdo & Ghosh, 2001) and the accretion stream model (Leahy & Kostka, 2008).

3.6   Conclusions

We have investigated the long term orbital variation of spectral parameters by exhaustive orbital phase resolved spectroscopic measurements of GX 301–2 with *MAXI*–GSC . The column density of the absorbing matter has a large value around the pre-periastron passage, suggesting the possible origin of X-ray flare due to enhanced mass accretion. A very large equivalent width of the Fe Kα line along with a small value of the column density in the orbital phase range 0.10-0.30 after the periastron passage indicates presence of high density absorbing matter behind the neutron star in these orbital phase range. The orbital dependence of column density and equivalent width of Fe line presented in this work provides stronger constraints to the dynamical wind plus stream model of Leahy & Kostka (2008).

Chapter 4

A study of two eclipsing systems: IGR J16393–4643 and 4U 1700–37[1]

4.1 IGR J16393–4643

4.1.1 Introduction

GR J16393–4643 belongs to an increasing class of heavily absorbed High Mass X-ray binaries, which are characterised by a very strong absorption with column density of absorbing matter $N_H \sim 10^{23}$ cm^{-2}. It was first discovered with the *ASCA* observatory during survey of the galactic plane (Sugizaki et al., 2001) and was named as AX J1639.0–4642 and was re-discovered in the *INTEGRAL* Galactic Plane Scan. The spin period of the system was found to be ~ 910 s with an orbital period of 4.2 days (Bodaghee et al., 2006; Corbet et al., 2010) and it occupies a unique position near the top edge of underfilled Roche lobe supergiant systems in the Corbet diagram (Jenke et al., 2012). Recent *Chandra* observation of the system refined its X-ray co-ordinates and found the position consistent with the optical counterpart being a supergiant O9 star with with radius R$\sim$ 20 R$_\odot$ at a distance of 25 kpc or a main sequence B star with radius R$\sim$ 10

---

[1]The work presented in this Chapter is published as a paper (2015, MNRAS, 446, 4148) and the other submitted to MNRAS for publication

$R_\odot$ at a distance of 12 kpc (Bodaghee et al., 2012a).

The X-ray spectrum of the pulsar is characterised by a highly absorbed power-law with an exponential cut-off along with Fe fluorescence lines (Lutovinov et al., 2005; Bodaghee et al., 2006). A strong absorption with a hydrogen column density of the order $\sim 10^{23}$ cm^{-2} is an evidence of a dense circumstellar environment surrounding the pulsar. Previous observations with *XMM*–Newton indicates the presence of a soft excess in the spectrum which could be due to X-rays scattering by the stellar wind (Bodaghee et al., 2006).

The orbital intensity profile for IGR J16393–4643 with *RXTE*–ASM and *RXTE*–PCA found no evidence of the presence of an X-ray eclipse. Previous estimates on the orbital inclination of the system were carried out assuming lack of X-ray eclipses and was found to be less than 60° (Thompson et al., 2006). However, we carried out the orbital intensity profile analysis for this source using 10 years long *Swift*–BAT light-curves in 15-50 keV energy band and found the presence of a short eclipse in the orbital intensity profile. We have used this X-ray eclipse to revise the orbital inclination of this system.

4.1.2 Orbital intensity profile analysis

We first estimated the orbital period of the system using 10 years long *Swift*–BAT light-curves with FTOOL "EFSEARCH". The estimated orbital period is $P_{orb} = 366150 \pm 1$ secs, consistent with Corbet et al. 2010. We then folded the light-curve with the orbital period to create orbital intensity profile. As seen in Figure 4.1, the orbital intensity profile shows a minimum intensity, taken as orbital phase zero (MJD: 53417.955), which indicates it to be an eclipsing binary (previously reported by Corbet & Krimm 2013). The eclipse duration is short with eclipse semi-angle $\theta_E \sim 17°$.

4.1.3 Determination of inclination of this system

Recent *Chandra* observation of this X-ray binary proposed the optical counterpart to be either a supergiant O9 star with radius $R \sim 20$ $R_\odot$ or a main sequence B star with radius
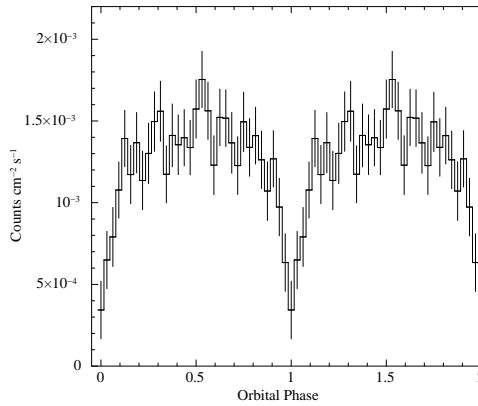
Figure 4.1: Light-curve of IGR J16393-4643 in 15-50 keV energy band of *Swift*–BAT folded with the orbital period (P_{orb} = 366150 secs). The orbital phase zero corresponds to the minima in intensity at epoch MJD: 53417.955

R$\sim$ 10 R$_\odot$ (Bodaghee et al., 2012a). The short orbital period of the binary system makes it more likely to have a supergiant O9 star as its companion than a main sequence B star. However, Bodaghee et al. (2012a) pointed out that having a supergiant O9 star as a companion would imply a lower limit of distance of 25 kpc to the binary as compared to a distance of 12 kpc for a main sequence B star.

The supergiant HMXBs like Cen X–3, Vela X–1 and OAO 1657–415 have masses of the companion star in the range of 10 M$_\odot$ – 30 M$_\odot$ and radii in the range of 10 R$_\odot$ – 35 R$_\odot$, with a nearly circularised orbit (Rappaport & Joss, 1983; Ash et al., 1999; van Kerkwijk et al., 1995; Mason et al., 2012). So assuming a circular orbit, the separation between the binary components a, can be expressed as

$$a^3 = \frac{G(M_c + M_{NS})P_{orb}^2}{4\pi^2} \tag{4.1}$$

where M$_{NS}$ is the mass of the neutron star which is assumed to be 1.4 M$_\odot$, P$_{orb}$ = 4.24 days is the orbital period of the system and M$_c$ is the mass of the supergiant companion star which is assumed to be in the range 10 M$_\odot$ – 30 M$_\odot$.

For a system showing X-ray eclipses, the orbital inclination of the system i is related

to the radius of the companion star R_O and orbital separation a by the following equation in Rubin et al. (1996)

$$\frac{R_O}{a} = \sqrt{\cos^2 i + \sin^2 i \quad \sin^2 \theta_E} \tag{4.2}$$

where $\theta_E \sim 17°$ is the observed eclipse semi-angle. Since for an X-ray binary, the radius of the companion star cannot exceed the Roche lobe radius of the system. So, the upper limit to the companion radius for a given mass is constrained by the Roche lobe radius R_{Roche}, which is given by the Equation 4.3 (Bowers & Deeming, 1984; Hill et al., 2005)

$$R_{\mathrm{Roche}} = a(0.38 + 0.2\log(\frac{M_c}{M_{NS}})) \tag{4.3}$$

Equation 4.1 gives the size of the binary system as a function of the companion mass. The size, and a given radius of the companion star, and the measured eclipse semi-angle gives a value of the orbital inclination (Equation 4.2). For a supergiant companion star, we have plotted two lines for companion stars mass of 10 $M_\odot$ and 30 $M_\odot$ in the plane of the inclination angle versus radius of the companion star. The blue shaded region shown in Figure 4.2 is thus the allowed region for inclination of the orbit. In addition, the Roche-lobe radius constraint on the companion star radius (given by Equation 4.3) puts a further lower limit on the inclination angle as shown in the same figure.

Similiarly, we carried out the above calculations for the companion as a main sequence B star having masses in the range of 2 $M_\odot$ – 16 $M_\odot$ and radii in the range of 5 $R_\odot$ – 25 $R_\odot$ (Habets & Heintze, 1981) and assuming a circular orbit. Figure 4.2 is the plot of the range of inclination angles allowed for given mass of the O9 supergiant companion star and main sequence B star as a function of its radius, assuming a circular orbit.

For a supergiant companion star radius of 20 $R_\odot$, the inclination of the orbital plane of the binary system is in the range $39° - 57°$. For a main sequence B star of radius 10 $R_\odot$, the inclination of the orbital plane of the binary system is in the range $60° - 77°$.
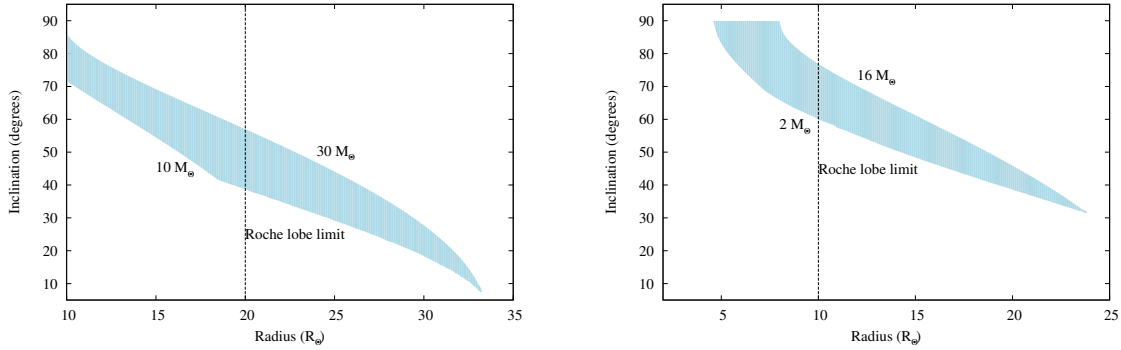
Figure 4.2: Left panel shows the plot of the range of inclination angles allowed for given mass of the O9 supergiant companion star as a function of its radius, assuming a circular orbit. Right panel shows the plot of the range of inclination angles allowed for given mass of the main sequence B star as a function of its radius, also assuming a circular orbit. See text for details. The dotted lines represent the 20 $R_\odot$ radius for a supergiant companion and the 10 $R_\odot$ radius for a B type companion (Bodaghee et al. 2012).

4.1.4 Pulsation and spectral analysis from a *Suzaku* observation

Here we present the simultaneous broad-band pulse profiles and spectral characteristics of the pulsar IGR J16393-4643 obtained from a *Suzaku* observation. The energy resolved pulse profiles are created for the first time for this source in a broad energy band. The broad-band spectral characteristics are studied both for the phase averaged as well as resolving the pulse phase into peak phase and trough phase.

Observations and Data Analysis

IGR J16393–4643 was observed with *Suzaku* during 12 March 2010 (ObsId: 404056010) with an useful exposure time of ∼ 44 kilosecs over a span of about 120 kilosecs. The observations were carried out at the 'XIS nominal' pointing position and the XIS were operated in 'standard' data mode in the 'Normal window' option, having a time resolution of 8 secs. For both the XIS and HXD data, we have used the filtered cleaned event files which are obtained using the pre-determined screening criteria described in the Suzaku

ABC guide. [2]

The XIS light-curves and spectra were extracted from the cleaned event files by selecting circular regions of 3' around the source centroid. The background light-curves and spectra were extracted by selecting circular regions of same size away from the source centroid. For HXD/PIN background, simulated 'tuned' non X-ray background event files (NXB) corresponding to the month and year of the observation was used to estimate the non X-ray background.[3] The cosmic X-ray background was simulated as suggested by the instrument team with appropriate normalisations and response files.[4] The response files for XIS were created using CALDB '20140211' and for HXD/PIN, response files were obtained from the *Suzaku* Guest Observer Facility.[5]

Timing Analysis

For the timing analysis of the source, we have applied barycentric corrections to the event data files using the FTOOLS task 'aebarycen'. Light-curves with time resolution of 1 s and 8 s were extracted from HXD/PIN (12-50 keV) and XIS (0.3-12 keV) respectively. Figure 4.3 shows the light-curves binned with a time bin of 908 secs *i.e* at the pulsar spin period, in XIS and PIN along with the hardness ratio. The count-rate in XIS and PIN increases gradually from the start of the observation upto 100 kilosecs by a factor of $\sim$ 2 and then decreases by a similar factor till the end of the observation. The hardness ratio remained constant throughout the observation. We have also folded the XIS and PIN light-curves with the *Swift*–BAT light-curves, to investigate the orbital phase of the *Suzaku* observation. As seen in Figure 4.3, the *Suzaku* observations were carried out roughly from orbital phase 0.55-0.9 *i.e* prior to going into the eclipse. The count-rate in XIS and PIN is seen to increases by a factor of $\sim$ 2 during orbital phase $\sim$ 0.65-0.8 and then again decreases till the end of the observation. The orbital intensity profile created with *Swift*–BAT is averaged over many orbital cycles, whereas the orbital intensity profile

---

[2]http://heasarc.nasa.gov/docs/suzaku/analysis/abc/node9.html

[3]http://heasarc.gsfc.nasa.gov/docs/suzaku/analysis/pinbgd.html

[4]http://heasarc.gsfc.nasa.gov/docs/suzaku/analysis/pin_cxb.html

[5]http://heasarc.gsfc.nasa.gov/docs/heasarc/caldb/suzaku
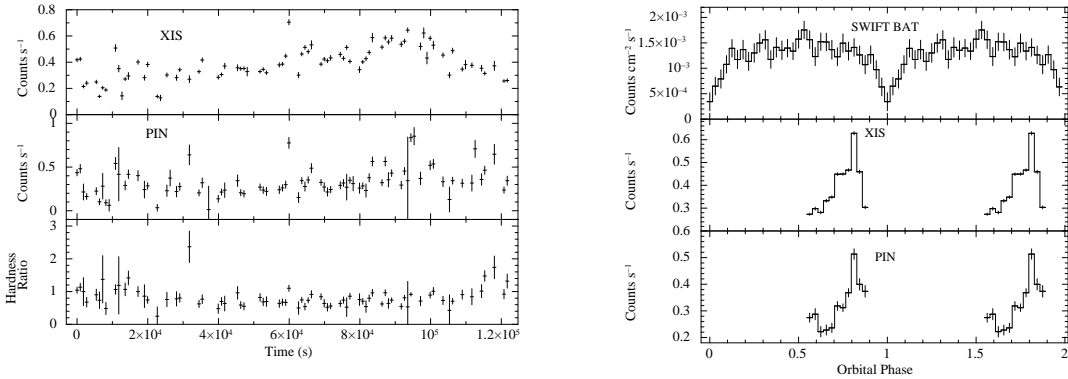
Figure 4.3: *Left Panel :* Light-curve of IGR J16393–4643 binned at the pulse period of 908 secs in 0.3-12 keV XIS energy band (top panel), 12-50 keV PIN energy band (middle panel) and the hardness ratio of the count-rates in PIN and XIS (bottom panel) are shown here. *Right Panel :* Light-curve of *Swift*–BAT , XIS and PIN folded with its orbital period (P_{orb} = 366150 secs).

created with XIS and PIN show variability on sub-orbital timescales, similar to that seen in OAO 1657–415 (Pradhan et al., 2014).

4.1.5 Energy resolved pulse profiles

We have searched for pulsations in the light-curves by applying pulse folding and χ^2 maximization technique and the pulse period was found to be 908.79 ± 0.01 secs. We then created the energy resolved pulse profiles by folding light-curves extracted in different energy bands with the pulse period. Light-curves from XIS0, XIS1 and XIS3 were added together to create the pulse profiles in XIS energy band 0.3-12 keV and sub bands within. From Figure 4.4, we see that the pulse profiles have a complex morphology with some energy dependance, which was also seen with *XMM*–Newton (Bodaghee et al., 2006) and *RXTE*–PCA (Thompson et al., 2006), but the broad-band nature of the pulse profiles are brought out from this *Suzaku* observation. Due to the presence of high column density of absorbing matter, very few photons are detected below 4 keV. The epoch for creation of the pulse profiles is adjusted to make the minima appear at phase zero in the PIN 12-50 keV energy band. The pulse minima is seen to become deeper at higher energies.
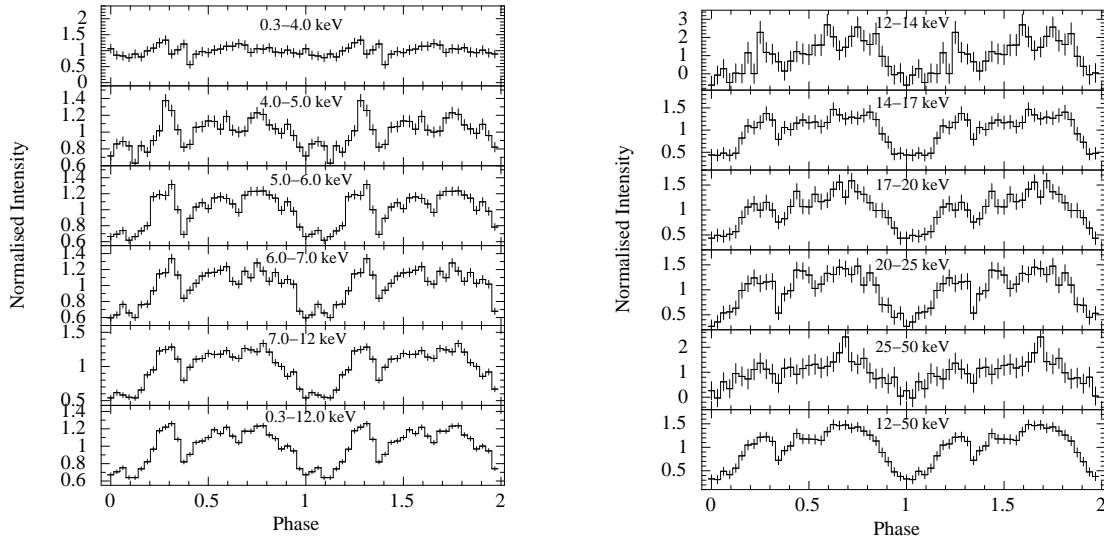
Figure 4.4: Energy resolved pulse profiles of IGR J16393–4643 folded with a period of 908.79 secs for XIS energy bands (left panel) and PIN energy bands (right panel). The epoch is chosen such that the pulse minima occur at phase 0.0 in the PIN 12-50 keV energy band.

A phase lag is seen in the energy resolved pulse profiles in the two XIS energy bands compared to the PIN energy bands, which is shown in Figure 4.5 for pulse profiles created in XIS energy band 0.3-6.0 keV and 6-12 and in PIN energy band 12-50 keV.

4.1.6   Pulse phase averaged spectrum

We have performed a pulse phase averaged spectral analysis of IGR J16393–4643 using spectra from three XIS and PIN. The energy range chosen for spectral fitting was 3.0 keV to 10.0 keV for XIS, since there were hardly any photons below 3.0 keV. For PIN, the energy range was chosen from 15 keV to 50 keV. The XIS spectra were rebinned by a factor of 12 upto 5 keV, by a factor of 6 from 5-7 keV and again by a factor of 12 from 7-10 keV. The PIN spectra was rebinned by a factor of 2 till 22 keV, by 8 from 22-45 keV and by a factor of 12 for the rest. The spectral fitting was done with XSPEC 12.8.1. To fit the continuum spectra, we have tried several standard continuum models used for
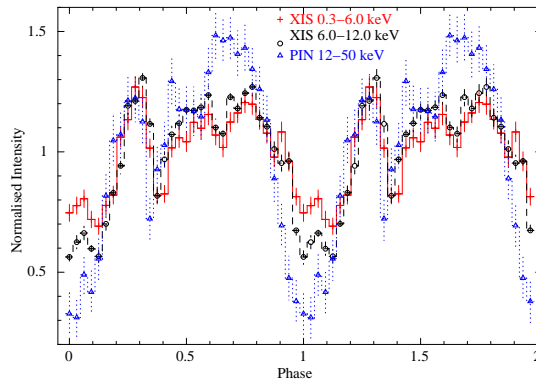
Figure 4.5: Overlaid pulse profiles created in XIS energy band 0.3-6.0 keV and 6-12 keV and in PIN energy band 12-50 keV, shows an indication of a phase lag.

HMXB pulsars like cut-off power-law (CUTOFFPL), power-law with high energy cut-off (HIGHECUT, White et al. 1983), power-law with a Fermi-Dirac cut-off (FDCUT, Tanaka 1986), and negative and positive power-law exponential (NPEX, Mihara 1995). The power-law with HIGHECUT and power-law with FDCUT spectral models provided the best fits to the phase averaged spectrum with physically acceptable parameter values and henceforth, we report results from these two spectral models.

We fitted the spectra simultaneously with all the parameters tied, except the relative normalisations of the instruments which were kept free. A 6.4 keV Fe Kα line was also found in the spectra, which was modelled by a gaussian emission line. The 7.1 keV Kβ line detected in the spectra with the *XMM*–Newton observation (Bodaghee et al., 2006) was marginally detected here with the 90 % upper limit on the line flux as 2×10^{-5} photons cm^{-2} s^{-1} and equivalent width of 33 eV, consistent with the upper limits quoted for *XMM*–Newton observation (6×10^{-5} photons cm^{-2} s^{-1} and 120 eV respectively; Bodaghee et al. 2006). The best fit parameter values of phase averaged spectrum for 90% confidence limits (except for $\sigma_{K\alpha}$ and equivalent width of the Fe line which are given for 1σ confidence limits) for the two spectral models power-law with HIGHECUT and power-law with FDCUT are given in Table 4.1. Figure 4.6 shows the best fit phase averaged spectrum using power-law with HIGHECUT and power-law with FDCUT models, along with the residuals.

Table 4.1: Best fit parameter values for power-law with HIGHECUT and power-law with FDCUT models for the phase averaged spectrum as well as the peak phase and trough phase spectra. Errors quoted for $\sigma_{K\alpha}$ and equivalent width of the gaussian Fe Kα line are for 1σ confidence limits and for rest of the parameters are for 90% confidence limits

Parameters	Phase averaged		Peak phase		Trough phase	
	HIGHECUT	FDCUT	HIGHECUT	FDCUT	HIGHECUT	FDCUT
N_H (10^{22} atoms cm^{-2})	26.5 ± 0.8	26.2 ± 0.8	27.4 ± 1.2	27.1 ± 1.2	26.4 ± 1.7	26.0^{+2}_{-3}
Photon Index (Γ)	0.91 ± 0.06	$0.86^{+0.07}_{-0.08}$	0.82 ± 0.09	$0.76^{+0.10}_{-0.13}$	1.2 ± 0.1	1.2 ± 0.1
Γ_{norm} (10^{-3} photons cm^{-2} s^{-1})	$3.8^{+0.5}_{-0.4}$	3.5 ± 0.5	$3.7^{+0.8}_{-0.6}$	$3.4^{+0.8}_{-0.6}$	$5.1^{+1.6}_{-1.2}$	$4.7^{+1.8}_{-1.4}$
Cut-off Energy (E_C keV)	20 ± 1	25^{+1}_{-3}	20 ± 1	25^{+2}_{-5}	19^{+6}_{-4}	25^{+4}_{-6}
Fold Energy (E_F keV)	9 ± 1	5 ± 1	9 ± 2	5 ± 2	11^{+5}_{-7}	6 ± 3
$F_{K\alpha}$ (10^{-5} photons cm^{-2} s^{-1})	$3.2^{+0.8}_{-0.7}$	$3.2^{+0.8}_{-0.7}$	3.9 ± 1.1	3.9 ± 1.1	5.1 ± 2.0	$5.2^{+1.9}_{-2.1}$
$\sigma_{K\alpha}$ (keV)	$0.02^{+0.03}_{-0.02}$	$0.02^{+0.03}_{-0.02}$	-	-	$0.13^{+0.05}_{-0.06}$	$0.14^{+0.04}_{-0.06}$
Equivalent width (eV)	46^{+7}_{-6}	46^{+7}_{-6}	47^{+8}_{-8}	48^{+8}_{-8}	99^{+23}_{-22}	102^{+21}_{-25}
Flux (XIS) (0.3-12 keV) (10^{-11} ergs cm^{-2} s^{-1})	3.6 ± 0.1	3.5 ± 0.1	4.2 ± 0.1	4.2 ± 0.1	2.5 ± 0.1	2.5 ± 0.1
Flux (PIN) (12-70 keV) (10^{-11} ergs cm^{-2} s^{-1})	2.7 ± 0.1	2.6 ± 0.1	3.4 ± 0.2	3.2 ± 0.2	1.6 ± 0.1	1.5 ± 0.2
χ^2_ν/d.o.f	1.17/296	1.18/296	1.03/280	1.05/281	1.10/289	1.09/289
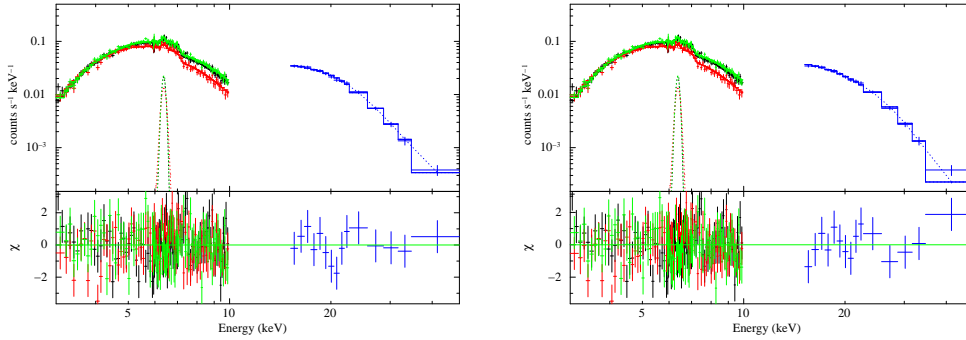
Figure 4.6: Phase averaged spectrum of IGR J16393–4643 with the best fit models power-law with HIGHECUT (left panel) and power-law with FDCUT (right panel) are shown here along with the contribution of residuals to the χ^2.

4.1.7   Pulse phase resolved spectrum

The energy dependence of the pulse fraction as seen in the XIS and PIN energy bands (Figure 4.4 and Figure 4.5) indicates a significant change in the spectrum with the pulse phase and we investigate the same with pulse phase resolved spectroscopy at the peak and trough of the pulse profile. The XIS and PIN spectrum were binned into two states: a peak phase around the pulse maximum (phase 0.4-0.8) and a trough phase around the pulse minima (phase 0.0-0.2 and 0.9-1.0), similar to the pulse phase definition used in Bodaghee et al. (2006). In the peak phase as well as the trough phase, the XIS spectra and PIN spectra were rebinned by the same factors used in phase averaged spectra. To study the changes in spectral parameters in the two pulse phases, we used the same models as in the phase averaged spectrum. However, width of the Fe Kα line could not be constrained in the peak phase spectra and was fixed to its phase averaged value. The best fit parameter values of the peak phase spectra and the trough phase spectra for 90% confidence limits (except for $\sigma_{K\alpha}$ and equivalent width of the Fe line for both the spectral models which are given for 1σ confidence limits) for the two spectral models power-law with HIGHECUT and power-law with FDCUT are given in Table 4.1. Figure 4.7 shows the peak phase and trough phase spectra using power-law with HIGHECUT and power-law with FDCUT spectral models, along with the residuals. A softening in the spectrum with an increase in the Fe equivalent width is noticed at the trough phase.
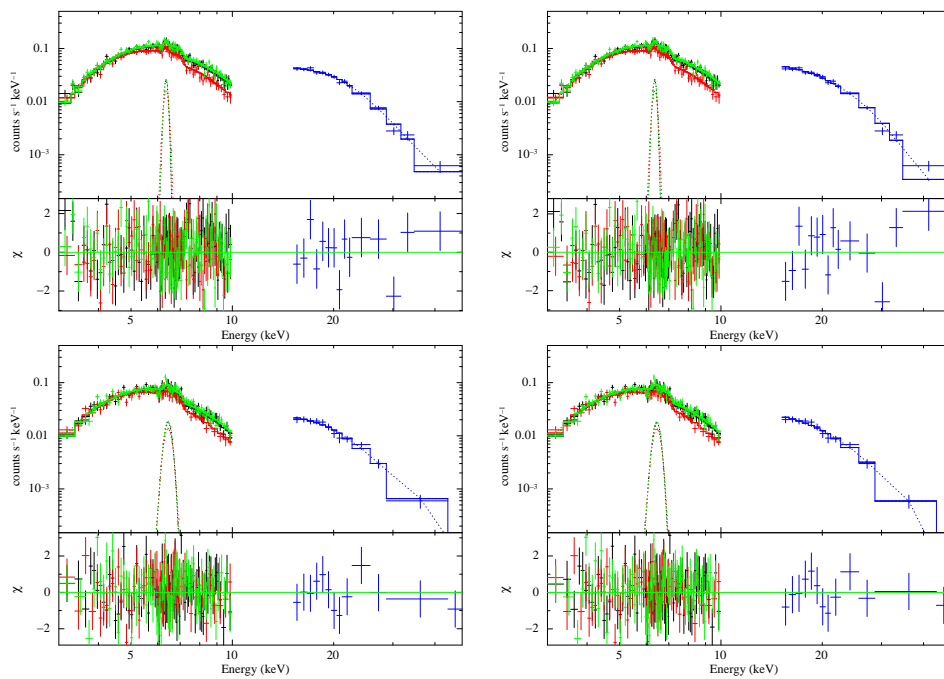
Figure 4.7: Peak phase spectrum of IGR J16393–4643 using power-law with HIGHECUT model (upper left panel) and power-law with FDCUT model (upper right panel) are shown here, along with the contribution of residuals to the χ^2. Same for the trough phase are shown in the two bottom panels.

4.1.8   Discussions

Energy dependent pulse profiles

Figure 4.4 shows the complex double peaked pulse profiles of IGR J16393–4643 in the *Suzaku* energy sub-bands. The pulse fraction increases with energy, from $\sim 33\%$ in XIS 0.3 - 12 keV energy band to $\sim 65\%$ in PIN 12 - 50 keV energy band, which is also seen in many other X-ray pulsars (White et al., 1983; Frontera & Dal Fiume, 1989; Nagase, 1989). There is a narrow dip present in the pulse profiles at pulse phase ~ 0.35, which was also seen in pulse profiles created with *RXTE*–PCA (Thompson et al., 2006) and *XMM*–Newton (Bodaghee et al., 2006). This narrow dip exists even at higher energies as seen in Figure 4.4 and Figure 4.5 for XIS and PIN energy bands. Narrow high energy dips in the pulse profiles are seen in other X-ray pulsars like GX 1+4 (Naik et al., 2005), EXO 2030+375 (Naik et al., 2013), A 0535+262 (Frontera et al., 1985; Cemeljic & Bulik, 1998) and are associated with the intrinsic beaming pattern of the source. From Figure 4.5, we see a phase lag of the soft photons with respect to the hard photons in the energy resolved pulse profiles. Such soft phase lags have been observed in millisecond X-ray pulsars (Cui et al., 1998; Ibragimov et al., 2011). However, further analysis with respect to the actual cause of phase lag is limited by the statistical quality of the data.

Phase resolved spectral characteristics

From phase averaged spectral characteristics of IGR J16393–4643 (Table 4.1 and Figure 4.6), we find very high line of sight column density of absorbing matter $\sim 3 \times 10^{23}$ cm^{-2}. Such high column density of absorbing matter has been found in previous studies of this system by *RXTE*–PCA (Thompson et al., 2006) and by *XMM*–Newton (Bodaghee et al., 2006) and is attributed to the circumstellar environment around the pulsar. The phase averaged spectrum is described by a power-law with spectral index $\Gamma \sim 0.9$ and a high energy cut-off above 20 keV. The presence of the soft excess as detected from the *XMM*–Newton observation (Bodaghee et al., 2006) could not be confirmed in the *Suzaku* observation. Due to limited statistical quality of this *Suzaku* observation, it is difficult

to make an in-depth pulse phase resolved spectral analysis.

Instead, the pulse profile is broadly resolved into peak phase and trough phase and pulse phase dependence of the spectral properties are studied in these two phase-bins (Figure 4.7). While the column density is similar in both the pulse phases, there is a change in the continuum spectral parameters which is observed for both the spectral models in Table 4.1. The spectrum is softer at the trough phase and harder at the peak phase, which may be due the additional softer photons near the off pulse regions. Alternately, this may also imply a deeper and more direct view into the emission region along the magnetic axis at the pulse peak as would be for the case for a fan beam kind of emission pattern (Pravdo et al., 1976). The cut-off parameters (fold energy E_F and cut-off energy E_C) for both power-law with HIGHECUT and power-law with FDCUT spectral models however, remain constant in the two pulse phases. The Fe Kα line is present in both the phases, with the equivalent width higher in trough phase than in peak phase. In contrast with the results obtained in Bodaghee et al. (2006) with the *XMM*–Newton, which operated in the limited energy band of 0.3-10 keV, there is an underlying change in the source spectrum as a function of pulse phase which is brought out from this broad-band *Suzaku* observation.

IGR J16393–4643 makes an interesting candidate for detailed pulse phase resolved spectroscopy with future X-ray missions with broad-band energy coverage. Such in-depth analysis will help in better understanding of the accretion geometry and beaming pattern of these underfilled Roche lobe systems.

4.2   4U 1700–37

4.2.1   Introduction

The orbits of X-ray binaries evolve due to various mechanisms like mass and angular momentum exchange between the compact object and the companion star, tidal interaction between the binary components (Lecar et al., 1976; Zahn, 1977), magnetic braking (Rappaport et al., 1983), stellar wind driven angular momentum loss (Brookshaw & Tavani, 1993; van den Heuvel, 1994), X-ray irradiated wind outflow (Ruderman et al., 1989) and gravitational wave radiation (Verbunt, 1993). In addition to orbital period evolution, the elliptic orbits of X-ray binaries also undergo apsidal motion. The classical apsidal motion is caused by tidal force (Cowling, 1938; Sterne, 1939) and hence the rate of apsidal angle change is directly related to the stellar structure constant of the component stars (Kopal, 1978; Claret & Gimenez, 1993). For an accreting X-ray pulsar, repeated measurements of orbital parameters by pulse timing analysis at separate intervals of time is an efficient way to study the orbital evolution of the binary system (Cen X–3 – Kelley et al. 1983; Her X–1 – Staubert et al. 2009; SMC X–1 – Levine et al. 1993; LMC X–4 – Levine et al. 2000; Naik & Paul 2004; 4U 1538–52 – Mukherjee et al. 2006; SAX J1808.4–3658 – Jain et al. 2008; OAO 1657–415 – Jenke et al. 2012) as well as its rate of apsidal motion (4U 0115+63 – Raichur & Paul 2010a). For eclipsing HMXB pulsars like Vela X–1 (Deeter et al., 1987) and 4U 1538–52 (Falanga et al., 2015), the rate of apsidal motion can also be calculated from the offset in the local eclipse period and the mean sidereal period, which is determined from pulse timing analysis. In case of eclipsing X-ray binaries, eclipse timing technique is used to determine the orbital evolution of binary systems (EXO 0748–676 – Parmar et al. 1991; Wolff et al. 2009; 4U 1822–37 – Jain et al. 2010; XTE J1710–281 – Jain & Paul 2011) as well as estimating parameters of the companion star and masses of the compact object (Coley et al., 2015; Falanga et al., 2015). In eclipse timing technique, the mid-eclipse times are used as fiducial markers to study any change in orbital period of the binary system. Mid-eclipse timing measurements have also been used to determine the rate of apsidal motion and other orbital parameters in case of

eccentric optical eclipsing binaries (Gimenez & Garcia-Pelayo, 1983; Wolf et al., 2004; Zasche et al., 2014). In the absence of pulsations or eclipses, stable orbital modulation curves have also been found useful for measurements of orbital evolution of some X-ray binaries like Cyg X–3 (Singh et al., 2002) and 4U 1820–30 (Peuten et al., 2014).

Orbital decay of the compact HMXBs are also of interest in the context of short GRBs and gravitational wave astronomy as these are the progenitors of double compact binaries. The massive companion will leave behind a second compact star and if the two compact stars survive as a double compact binary, eventual merging of the two stellar components are believed to produce the short GRBs and are also expected to produce the sources for gravitational wave detection (Belczynski et al., 2002; Abadie et al., 2010).

The massive X-ray binary 4U 1700–37 was discovered with *Uhuru* (Jones et al., 1973), which revealed it to be an eclipsing binary system with an orbital period of 3.412 days. The optical companion, HD 153919, is a O6.5 Iaf+ star, situated at a distance of 1.9 kpc and one of the most massive and hottest stars known in an HMXB (Ankay et al., 2001). The nature of the compact object is uncertain due to lack of X-ray pulsations from the system (Rubin et al., 1996). Lack of pulsations from 4U 1700–37 makes it difficult to determine the parameters of the binary orbit, especially eccentricity of the orbit and hence the rate of apsidal motion. Estimation of the orbital parameters using radial velocity measurements of the companion star HD 153919 from the ultraviolet and optical spectral lines (Hutchings, 1974; Heap & Corcoran, 1992; Clark et al., 2002; Hammerschlag-Hensberge et al., 2003) was complex due to extreme mass loss rate of the companion as well as very high stellar wind. Previous measurements of orbital parameters by Hammerschlag-Hensberge et al. (2003) using ultraviolet spectral lines with *International Ultraviolet Explorer*, found it to satisfy an orbital solution with an eccentricity $e \sim 0.22$. 4U 1700–37 is an archetypal system to study the orbital evolution using eclipse timing as it is a bright source with sharp eclipse transitions in the hard X-rays.

Earlier measurements of the mid-eclipse times spanning 20 years, both from the single pointed observations covering one full orbital cycle from *Uhuru* (Jones et al.,

1973), *Copernicus* (Branduardi et al., 1978) and *EXOSAT* (Haberl et al., 1989) as well as continuous observations with the all sky monitors *Granat*/WATCH (Sazonov et al., 1993) and *BATSE* (Rubin et al., 1996), showed an orbital period decay rate of $\dot{P}/P = -3 \times 10^{-6}$ yr^{-1} (Rubin et al., 1996). Recent work by Falanga et al. (2015), using the mid-eclipse measurements from *RXTE*–ASM and *INTEGRAL*, along with the previous mid-eclipse measurements from Rubin et al. (1996), showed a slower orbital decay with a rate of $\dot{P}/P = -1.6 \times 10^{-6}$ yr^{-1}.

We have used the above mentioned mid-eclipse times and new mid-eclipse time measurements to obtain a long term eclipse history and orbital evolution of the system. We then investigated the possibility of deriving or constraining the eccentricity and rate of apsidal motion of 4U 1700–37 using the mid-eclipse timing measurements and the eclipse duration measurements independently with 10 years of *Swift*–BAT light curves.

4.2.2   Mid-eclipse time measurements

We have used the earlier reported mid-eclipse measurements from single pointed observations covering the X-ray eclipse with *Uhuru* (Jones et al., 1973), *Copernicus* (Branduardi et al., 1978) and *EXOSAT* (Haberl et al., 1989). We have also used the mid-eclipse time from a *Copernicus* observation in 1974 (Mason et al., 1976) which was not used in the previous studies (Rubin et al., 1996; Falanga et al., 2015). Mid-eclipse times were also reported from the long term observations with X-ray all sky monitors *Granat*/WATCH (Sazonov et al., 1993), *BATSE* (Rubin et al., 1996) and *INTEGRAL* (Falanga et al., 2015), which are also used in the present analysis.

We have used long term light curves from *RXTE*–ASM, *Swift*–BAT and *MAXI*–GSC to determine new mid-eclipse times of 4U 1700–37. Falanga et al. (2015) had also reported mid-eclipse times from *RXTE*–ASM lightcurves in the energy band of 1.5–12 keV. Due to the photo-electric absorption of X-rays by the dense stellar wind of the companion which affects the soft X-rays photons more than the hard X-rays photons, the eclipse is sharper and more pronounced in the light-curve of *RXTE*–ASM in 5–12 keV energy band compared to its profile seen in the soft X-ray energy band. Therefore,
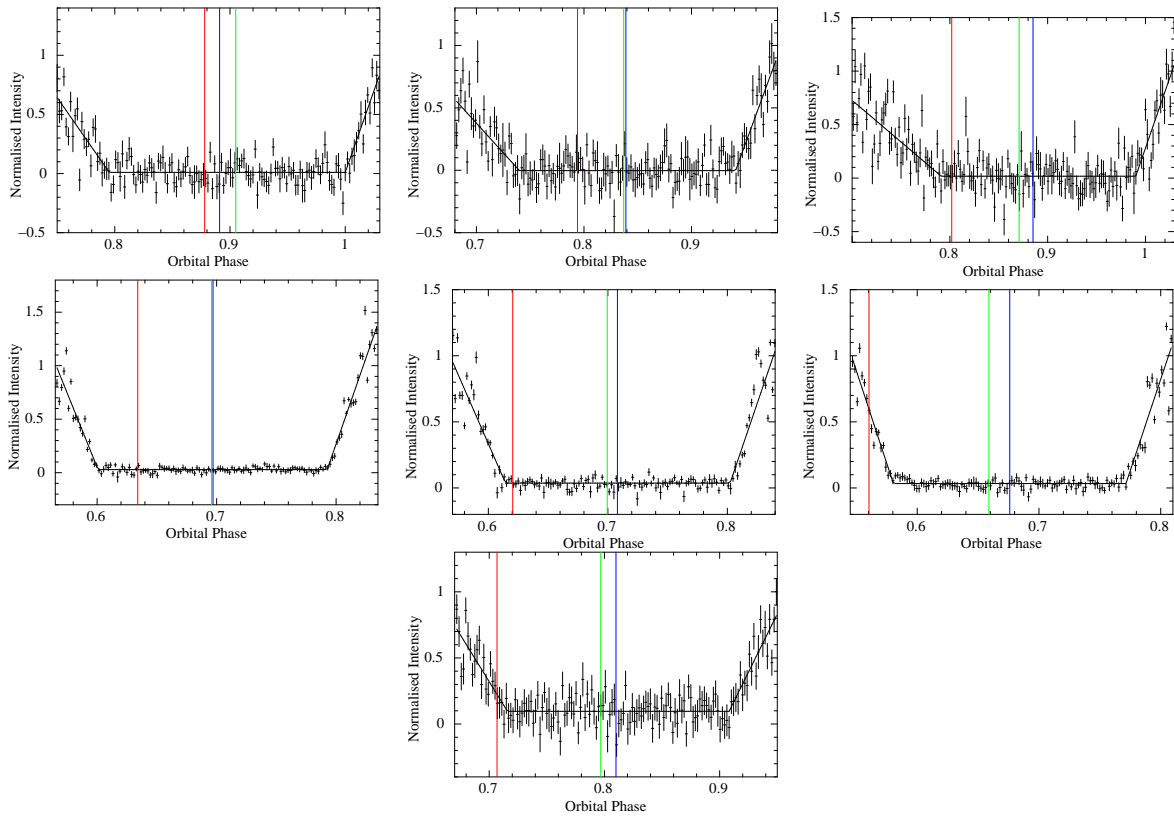
Figure 4.8: Orbital intensity profiles near the eclipse constructed for 3 light curve segments for 5-12 keV *RXTE*–ASM (top panel), 3 light curve segments for 15-50 keV *Swift*–BAT (middle panel) and 5-20 keV *MAXI*–GSC light curve (bottom panel). Blue line denotes the measured mid-eclipse phase, red line denotes the mid-eclipse phase expected from an orbital period change of $\dot{P}/P = -3.3 \times 10^{-6}$ yr^{-1} from Rubin et al. (1996) and green line is the expected mid-eclipse phase from an orbital period change of $\dot{P}/P = -1.6 \times 10^{-6}$ yr^{-1} from Falanga et al. (2015)

.

Table 4.2: Mid-eclipse time measurements along with errors calculated as mentioned in Section 2.1

Satellite	Energy Range	Mid-eclipse Time (MJD) with reported errors	Mid-eclipse Time (MJD) with re-calculated errors	Mid-eclipse Time (MJD) with statistical errors	Reference
Uhuru[⋆]	2-6 keV	41452.64(1)	41452.640(34)	-	Rubin et al. (1996)
Copernicus	2.8-8.7 keV	-	42230.625(34)	-	Mason et al. (1976)
Copernicus[⋆]	2.8-8.7 keV	42609.25(1)	42609.250(34)	-	Branduardi et al. (1978)
Copernicus[⋆]	2.8-8.7 keV	42612.646(10)	42612.646(34)	-	Branduardi et al. (1978)
Copernicus[⋆]	2.8-8.7 keV	43001.604(10)	43001.604(34)	-	Branduardi et al. (1978)
Copernicus[⋆]	2.8-8.7 keV	43005.000(10)	43005.000(34)	-	Branduardi et al. (1978)
EXOSAT	2-10 keV	46160.840(3)	46160.840(34)	-	Haberl et al. (1989)
Granat/WATCH[⋆]	8-20 keV	48722.940(31)	48722.940(34)	-	Sazonov et al. (1993)
BATSE	20-120 keV	48651.365(31)	48651.365(34)	-	Rubin et al. (1996)
BATSE	20-120 keV	49149.425(27)	49149.425(34)	-	Rubin et al. (1996)
INTEGRAL	17-40 keV	52861.29(2)	52861.290(17)	-	Falanga et al. (2015)
INTEGRAL	17-40 keV	53270.69(2)	53270.690(17)	-	Falanga et al. (2015)
INTEGRAL	17-40 keV	53472.00(2)	53472.000(17)	-	Falanga et al. (2015)
INTEGRAL	17-40 keV	53785.82(3)	53785.820(17)	-	Falanga et al. (2015)
INTEGRAL	17-40 keV	54164.55(2)	54164.550(17)	-	Falanga et al. (2015)
INTEGRAL	17-40 keV	54341.97(3)	54341.970(17)	-	Falanga et al. (2015)
RXTE–ASM	5-12 keV	-	50865.485(17)	50865.485(8)	Present Work
RXTE–ASM	5-12 keV	-	52445.102(17)	52445.102(11)	Present Work
RXTE–ASM	5-12 keV	-	54533.033(17)	54533.033(13)	Present Work
Swift–BAT	15-50 keV	-	54028.076(17)	54028.076(1)	Present Work
Swift–BAT	15-50 keV	-	55246.031(17)	55246.031(2)	Present Work
Swift–BAT	15-50 keV	-	56467.395(17)	56467.395(1)	Present Work
MAXI–GSC	5-20 keV	-	55935.181(17)	55935.181(9)	Present Work
RXTE–PCA	2-60 keV	-	51295.331(17)	-	Present Work

⋆ denotes the mid-eclipse times whose errors were re-analysed by Rubin et al. (1996).

we have used 16 years long 5–12 keV light curve with *RXTE*–ASM in this work and divided it into 3 segments, each consisting of about 5.3 years of data. The 10 years of *Swift*–BAT light curve in the 15-50 keV energy band was divided into 3 segments, each of duration 3.3 years. The *MAXI*–GSC light curve for 4.5 years was extracted in 5–20 keV energy band using the *MAXI* on demand data processing[6]. We have applied barycentric corrections to the light-curves using the FTOOLS task 'earth2sun'. The orbital period of the system is estimated separately for each segment of light curve using the FTOOLS task 'efsearch' and then these light-curves are folded with their respective orbital period with the FTOOLS task 'efold' to create orbital intensity profiles. The orbital intensity profiles near the eclipse were fitted with a double ramp function having different linear ingress and egress profiles and a constant count-rate during the eclipse, given in Equation 4.4.

$$
\begin{aligned}
F(X) &= P3 \quad \text{for} \quad (P1 - P2) < X < (P1 + P2) \\
&= P4 \times (X - (P1 + P2)) + P3 \quad \text{for} \quad X > (P1 + P2) \\
&= -P5 \times (X - (P1 - P2)) + P3 \quad \text{for} \quad X < (P1 - P2)
\end{aligned}
\tag{4.4}
$$

where P1 is the mid-eclipse phase, P2 is the half width of the eclipse, P3 is the count-rate during eclipse, P4 is the slope during eclipse egress, P5 is the slope during eclipse ingress. We have also used *RXTE*–PCA observations (ObsId 30094), from April 1999 to August 1999, covering eclipse ingress and egress for 120 days or 11 orbital cycles. The light-curve of *RXTE*–PCA observations is folded with the orbital period estimated for the first segment of *RXTE*–ASM light curve.

Figure 4.8 shows the orbital intensity profiles near the eclipses created from 3 light-curve segments of *RXTE*–ASM, 3 light-curve segments of *Swift*–BAT and the *MAXI*–GSC light-curve, fitted with a two ramp function. The blue vertical line in each panel denotes the measured mid-eclipse phase, red line denotes the mid-eclipse phase expected from the orbital period decay extrapolated from Rubin et al. (1996) and the green line is the expected mid-eclipse phase from the orbital period decay extrapolated from Falanga

---

[6]http://maxi.riken.jp/mxondem/

et al. (2015). All the mid-eclipse times extrapolated from Rubin et al. (1996) and all but one from Falanga et al. (2015) appear before the measured mid-eclipse phase for all the orbital intensity profiles, implying that the orbital period decay is lower than the previously estimated values.

The mid-eclipse times used for the analysis, both the earlier reported values as well as the new mid-eclipse times, are given in Table 4.2. The previously quoted uncertainities on the mid-eclipse times from *Uhuru*, *Copernicus* and *EXOSAT* were re-estimated by Rubin et al. (1996) and were calculated disparately from that of the mid-eclipse times from *Granat*/Watch and *BATSE* observations given in Table 2 in Rubin et al. (1996). The different error bars quoted previously are only the statistical errors. However, eclipse measurements in different energy bands with different instruments are also likely to have some systematic differences. To have a more realistic estimates of error bars and only with the aim of measuring a long term period derivative, we have re-estimated the errors on the mid-eclipse times, which are now likely to include the systematic differences between the different instruments. We have divided the mid-eclipse times into two segments, from MJD: 41452 - 49150 and MJD: 49151 - 56468. A linear fit is done separately on these two segments and the average standard deviation of the data-points from the linear fit is taken as the errors on the mid-eclipse times for these two segments (given in Table 4.2)

Systematic errors associated with the mid-eclipse time measurement with *EXOSAT*–GSPC and *RXTE*–PCA

As seen in top panel of Figure 4.9, the orbital intensity profile of 4U 1700–37 constructed out of long term light curves from the X-ray all sky monitors like *Swift*–BAT show a smooth profile with a sharp eclipse due to averaging effects of observations made over many orbits. However at short timescales, the light curves show strong variations, including flares and dips, characteristic of many HMXBs. Among the light curves of 4U 1700–37, those with single observation covering eclipse like *EXOSAT*–GSPC and *RXTE*–PCA show strong flares and dips (bottom panel of Figure 4.9), which introduces significant uncertainities in the eclipse ingress and egress profiles and hence, in
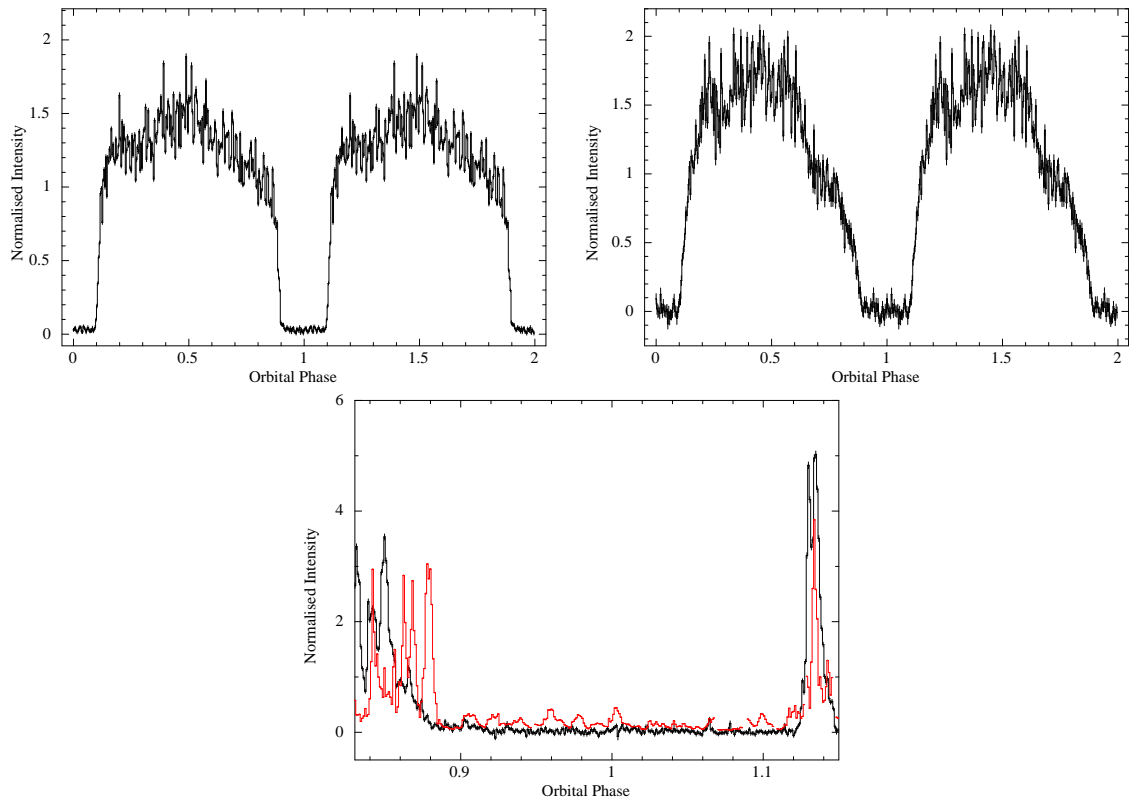
Figure 4.9: *Top panel*: Plot of the orbital intensity profile created out of 10 years of *Swift*–BAT data in 15-50 keV energy band (left panel) and 16 years of *RXTE*–ASM in 5-12 keV energy band (right panel), which shows an averaged smooth profile with sharp eclipse. *Bottom panel*: Plot of the folded orbital intensity profile near the eclipse using *RXTE*–PCA (red line) observations overlaid on the *EXOSAT*–GSPC orbital profile (black line), which shows the presence of flares and dips just outside the eclipse.

Table 4.3: Orbital ephemeris of 4U 1700–37

Epoch	T_0	49149.412 ± 0.006 MJD
Orbital period	P_{orb}	3.411660 ± 0.000004 days
Orbital period decay	$\dot{P}/P$	$-(4.7 \pm 1.9) \times 10^{-7}$ yr^{-1}

the mid-eclipse time determination. The mid-eclipse time estimated from the *EXOSAT* observation in 1985 was quoted to have a statistical error of 0.003 days (Haberl et al., 1989). We have extracted the *EXOSAT*–GSPC light curve in the 8–14 keV band and constructed the orbital intensity profile by folding it with the orbital period mentioned in Haberl et al. (1989). As seen in the right panel of Figure 4.9, the determination of the exact point of ingress and egress of the eclipse is complicated by the presence of flares and/or dips around the eclipse ingress and egress. To further emphasize on the contribution of flares in uncertainities on the mid-eclipse times in case of pointed observations, we have overlaid the orbital intensity profile from the *RXTE*–PCA observations (ObsId:30094) in the same plot. From the right panel of Figure 4.9, we infer that the statistical error of 0.003 days or 260 secs quoted in Haberl et al. (1989) is an underestimate of the actual error on the mid-eclipse time, as there is a larger systematic error owing to flares/dips. Determination of eclipse duration is also complicated by the presence of same flares and/or dips. In fact the eclipse durations determined from single observations with *Uhuru* (Jones et al., 1973), *Copernicus* (Branduardi et al., 1978) and *EXOSAT* (Haberl et al., 1989) are considerably larger with large error bars than those estimated from long term light curves from the all sky monitors.

We have re-calculated the errors on the *EXOSAT* mid-eclipse time as mentioned in the previous Section. It appears that the faster rate of orbital period decay in the earlier estimates (Rubin et al., 1996; Falanga et al., 2015) were results of small statistical error considered for the *EXOSAT* mid-eclipse data.
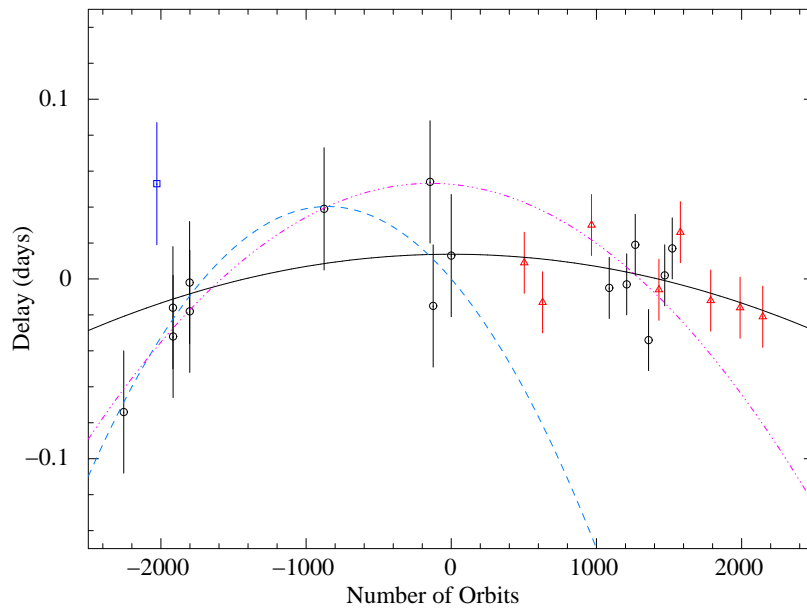
Figure 4.10: Delay in mid-eclipse times with respect to a constant orbital period. The black circles are the archival measurements of the mid-eclipse times and the red triangles are the new measurements of mid-eclipse times. The blue box datapoint is the mid-eclipse time measurement from *Copernicus* 1974 observation, which was not used in previous studies on the orbital evolution of the system but is used in this study. The solid black line is the quadratic component of the best fits to the mid-eclipse times. The blue dashed line and the magenta dot-dashed line are the quadratic components of the best-fits reported in Rubin et al. (1996) and Falanga et al. (2015) respectively.

4.2.3 Orbital evolution of 4U 1700–37

The mid-eclipse times given in Table 4.2 along with their errors are fitted to a quadratic function

$$T_N = T_0 + PN + \frac{1}{2}P\dot{P}N^2 \tag{4.5}$$

where T_N is the mid-eclipse time of the Nth orbital cycle. P is the orbital period in days and $\dot{P}$ is the orbital period derivative, both at time T_0.

The definition of T_0 and orbit number are same as mentioned in Rubin et al. (1996). The best fit to the mid-eclipse times for a constant orbital period gives $T_0 = 49149.412 \pm 0.006$ MJD, orbital period $P = 3.411660 \pm 0.000004$ days with a $\chi^2 = 28.3$ for 22 degrees of freedom. The mid-eclipse times fitted with a quadratic function as in Equation 4.5 gives the values of orbital period decay $\dot{P}/P = -(4.7\pm1.9) \times 10^{-7}$ yr^{-1} with a $\chi^2 = 23.8$ for 21 degrees of freedom. The orbital ephemeris is also tabulated in Table 4.3. For the orbital ephemeris given in Falanga et al. (2015), the value of $\chi^2 = 67.15$ for 24 degrees of freedom. The orbital period decay rate of 4U 1700–37 determined here is smaller compared to the earlier estimates (Haberl et al., 1989; Rubin et al., 1996; Falanga et al., 2015). A plot of the delay in mid-eclipse times with respect to a constant orbital period as a function of the number of orbital cycles, along with the best fit quadratic function is given in Figure 4.10. The quadratic function reported in Rubin et al. (1996) and Falanga et al. (2015) are overlaid on the same plot.

4.2.4 Eccentricity and Apsidal Motion of 4U 1700–37

In a close binary stellar system, the rate of apsidal motion due to tidal forces is given by (Claret & Gimenez, 1993)

$$\frac{\dot{\omega}}{360} = k(\frac{R_\star}{a})^5(15qg(e) + \Omega^2(1+q)f(e)) \quad \text{deg/cycle} \tag{4.6}$$

where e is the eccentricity, $R_\star$ is the companion star radius, a is the binary separation, q is the mass ratio of the compact object to the companion star and Ω is ratio of the

Table 4.4: Stellar parameters for HD 153919 and orbital parameters of 4U 1700–37

Parameter	Value	Reference
$R_\star$	$22 \pm 2\ R_\odot$	Falanga et al. (2015)
$M_\star$	$46 \pm 5\ M_\odot$	Falanga et al. (2015)
M_C	$1.96 \pm 0.19\ M_\odot$	Falanga et al. (2015)
Ω	0.47	Falanga et al. (2015)
log k	-2.2	Claret (2004)
i	66°	Rubin et al. (1996)
a	$35\ R_\odot$	Falanga et al. (2015)
P_{orb}	3.4117 days	

rotational velocity of the companion star to its orbital angular velocity

$$g(e) = (1 + \frac{3}{2}e^2 + \frac{1}{8}e^4)(1 - e^2)^{-5}$$

$$f(e) = (1 - e^2)^{-2}$$

Using the binary parameters of 4U 1700–37 along with its uncertainities ($R_\star$, a, q, P_{orb} from Table 4.4), a reasonable value of stellar constant *log k* of -2.2 corresponding to the companion star HD 153919 type (Claret, 2004) and e in the range of 0.01–0.22, we get an apsidal motion rate of 10 ± 3 degrees/year. For Vela X–1 and 4U 1538–522, using the binary parameters from Table 7 in Falanga et al. (2015), an estimation of the rate of apsidal motion is ~ 1 degree/yr and 5 degree/yr respectively, similar to that measured in these sources (Deeter et al., 1987; Falanga et al., 2015). The major source of uncertainity in estimating the rate of apsidal motion arises from the value of stellar constant k, which for some HMXBs are constrained by observations of apsidal motion in X-ray binaries (Raichur & Paul, 2010a).

The two interesting consequences of a large apsidal advance rate in an eclipsing X-ray binary are that the delay in the mid-eclipse times and the value of eclipse duration both would vary with a period of $360°/\dot{\omega}$. The delay in mid-eclipse times due to apsidal motion

is seen in close eclipsing optical binary stars (Gimenez & Garcia-Pelayo, 1983; Wolf et al., 2004; Zasche et al., 2014). The mid-eclipse times Table 4.2 and the corresponding eclipse duration measurements of 4U 1700–37 have been carried out with a large number of instruments of different sensitivities and in different energy bands. We have mentioned before that this causes significant systematic differences and therefore are not ideal to investigate the effects of apsidal motion. Eclipse duration is also found to be dependent on the energies of the X-rays with some eclipses lasting longer at lower energies than higher energies (van der Meer et al., 2007). So we have used hard X-ray light curve from *Swift*-BAT which has the highest statistical quality (second panel in Figure 4.8) and have divided it into 10 segments of 1 year data and searched for the signatures of an apsidal motion for an eccentric orbit. The yearly measurements of the eclipse data (mid-eclipse time and eclipse duration) are useful to probe an $\dot{\omega}$ in the range of 5-200 degrees per year. Since these 10 measurements are from the data obtained with the same instrument, it is unlikely to have much systematic difference between different data points.

Mid-eclipse time variation due to apsidal motion

For an elliptic orbit of a compact object around the companion star, the angle of periastron is defined as angle from the sky tangent plane L=0 to the apsidal line (left panel of Figure 4.11). We define θ as the orbital conjunction, which is related to the mid-eclipse times. For an orbital inclination of 90°, $\theta = 180°$ for X-ray eclipse (*i.e* the companion star occulting the compact object). For a system having small eccentricity and undergoing apsidal motion, and assuming an orbital inclination $i = 90°$, the mid-eclipse times can be written as (Equation 19 in Gimenez & Garcia-Pelayo 1983)

$$T_N = T_0 + PN + \frac{eP_a}{\pi}\cos(\omega_0 + \Delta\omega N) \qquad (4.7)$$

where $\Delta\omega$ is the change in ω in one orbital cycle. P_a is the anomalistic orbital period defined by the interval of time between two consecutive periastron passages and given
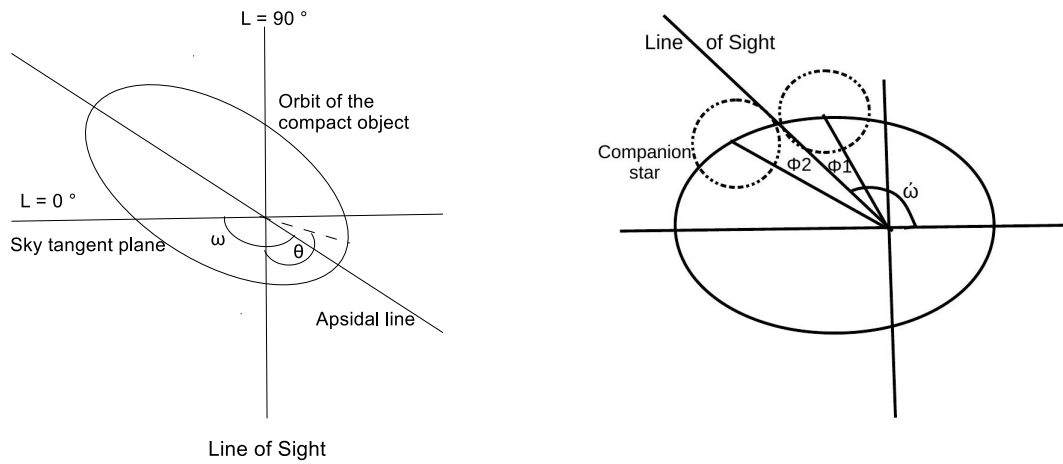
Figure 4.11: *Left Panel :* Schematic orbit of the compact object around the companion star. *Right Panel :* The ellipse represents the motion of the companion star with respect to the compact star at the focus. See text for description of the various angles.

by :

$$P_a = \frac{P}{(1 - \frac{\Delta\omega}{2\pi})} \tag{4.8}$$

For moderate values of $\Delta\omega$, $P_a \sim P$ (orbital period). After subtracting the linear component, Equation 4.7 reduces to:

$$T_N - (T_0 + PN) = \frac{eP}{\pi}\cos(\omega_0 + \Delta\omega N) \tag{4.9}$$

The orbital inclination of the binary system 4U 1700–37 is of the order of 60°–70° (Rubin et al., 1996; Falanga et al., 2015). Hence, including the orbital inclination term in Equation 4.7 will lead to a change in the estimation of ω_0 of the system. However, the estimation of $\Delta\omega$ and eccentricity e is independent of the orbital inclination of the system.

Variation in eclipse duration due to apsidal motion

Considering the motion of the companion star around the compact object, we calculated the eclipse durations as a function of the angle of periastron for different values of e for an orbital inclination of 90°. In the right panel of Figure 4.11, the ellipse represents the motion of the companion star with respect to the compact star at the centre. ϕ_1 and ϕ_2 represent the eclipse ingress and egress, $R_\star$ is the companion star radius and ω' is the angle between the periastron and the line of sight.

$$\omega' = \omega - \frac{\pi}{2} \tag{4.10}$$

If θ is the position angle of the companion star, the eclipse ingress and egress ($\phi_{1,2}$) can be determined from

$$\sin\phi_{1,2} = \beta(1 + e\cos\theta_{1,2}) \tag{4.11}$$

where $\beta = \frac{R_\star}{a(1-e^2)}$.

The eclipse duration can be estimated as:
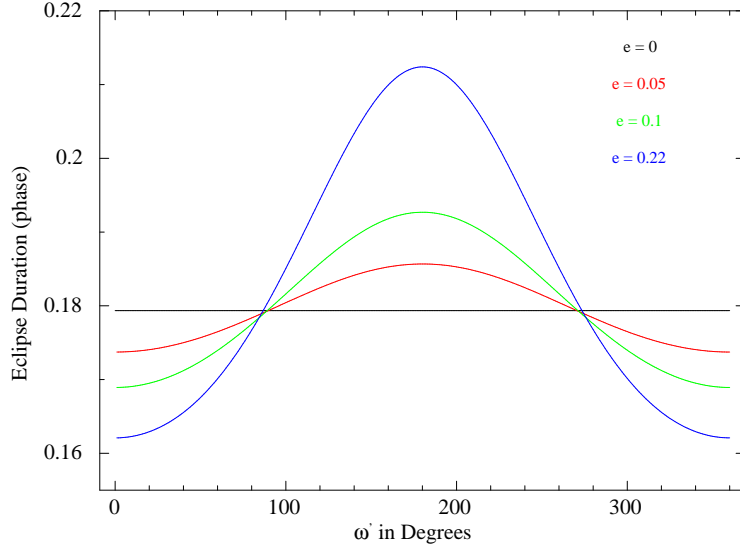
Figure 4.12: Plot of variation of eclipse duration as a function of ω' for different value of eccentricity, assuming an orbital inclination of 90°. Increasing values of eccentricity increases the ratio of maximum to minimum eclipse duration.

$$\Delta T(\omega') = \frac{a^2(1-e^2)^2}{L} \int_{\omega'-\phi_1}^{\omega'+\phi_2} \frac{d\theta}{(1+e\cos\theta)^2} \tag{4.12}$$

where $L = (G(M_\star + M_C)a(1-e^2))^{\frac{1}{2}}$.

Inclusion of the orbital inclination of the system would lead to a change in the projected semi-major axis $a_x \sin i$ instead of a in Equation 4.12. However, the ratio of maximum value of the eclipse duration to its minimum value will remain the same, which is used to estimate the eccentricity of the system. Using the values of the binary parameters ($M_\star, M_C, i,$ and a from Table 4.4), we have calculated the eclipse duration as a function of ω' for different values of eccentricity, shown in Figure 4.12. The maximum value of eclipse duration to its minimum value is approximately equal to $\frac{1+e}{1-e}$.

The *Swift*–BAT eclipse data

The mid-eclipse time measurements from the 10 segments of 1 year *Swift*–BAT light curve are shown in the left panel of Figure 4.13 after subtracting the linear component.

Table 4.5: Mid-eclipse time and eclipse duration measurements along with errors (1 σ confidence limit) for 10 segments of 1 year each *Swift*–BAT data

Experiment	Mid-eclipse Time (MJD)	Eclipse Duration (in Phase)
Segment 1	53601.624±0.001	0.204±0.002
Segment 2	53970.078±0.001	0.190±0.002
Segment 3	54335.115±0.002	0.188±0.002
Segment 4	54700.164±0.002	0.196±0.002
Segment 5	55068.624±0.002	0.200±0.002
Segment 6	55433.678±0.003	0.186±0.004
Segment 7	55798.726±0.003	0.186±0.004
Segment 8	56163.759±0.002	0.192±0.002
Segment 9	56528.811±0.002	0.192±0.004
Segment 10	56893.847±0.002	0.192±0.002
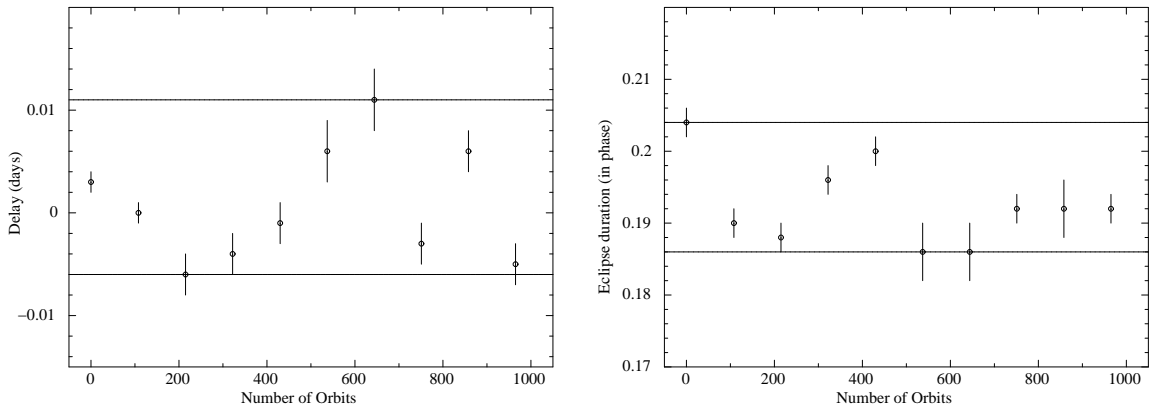
Figure 4.13: *Left Panel :* Delay in mid-eclipse times with respect to a constant orbital period for 10 segments of 1 year *Swift*–BAT light curves plotted as function of number of orbits, along with solid lines showing the maximum and minimum value of the delay. This limit is compared to the amplitude $\left(\frac{eP}{\pi}\right)$ in Equation 4.9 to give an eccentricity value of 0.008. *Right Panel :* Plot of eclipse duration as function of orbit number calculated from 10 segments of 1 year *Swift*–BAT light curves, along with solid lines showing the maximum and minimum value of the eclipse duration. This limit is compared to $\frac{1+e}{1-e}$ to give an eccentricity value of 0.05.

It shows a maximum variation of about $\pm$ 0.01 days. The eclipse durations measured from the same time segments obtained by fitting the same ramp function as described in Section 3.5.1 are shown in right panel of Figure 4.13. The maximum variation in eclipse duration is less than $\pm$ 5%. These two data sets, of mid-eclipse time variation and variation of eclipse duration also given in Table 4.5, do not show any periodic variation with a same period. It is therefore not possible to determine any apsidal motion rate from these data. However, the maximum variation in both the plots can be used to put upper limits on the eccentricity by comparing them with the amplitude term $(\frac{eP}{\pi})$ in Equation 4.9 and to $\frac{1+e}{1-e}$ respectively.

The upper limit on eccentricity of 4U 1700–37, obtained from the two methods are 0.008 and 0.05 respectively. We note here that these limits are applicable for apsidal motion rate greater than about 5 degrees per year. The limits are much smaller than the eccentricity reported from Doppler velocity measurements of the companion star by Hammerschlag-Hensberge et al. (2003).

4.2.5   Possible Causes of Orbital Period Decay

Orbital period changes are found to occur in High Mass X-ray binaries like Cen X–3, SMC X–1 (Raichur & Paul, 2010b), LMC X–4 (Naik & Paul, 2004), OAO 1657–415 (Jenke et al., 2012) and in Low Mass X-ray binaries like Her X–1 (Staubert et al. 2009), EXO 0748–676 (Wolff et al., 2009), 4U 1822–37 (Jain et al., 2010), and SAX J1808.4–3658 (Jain et al., 2008). In case of Low Mass X-ray binaries, the orbital evolution is assumed to occur mainly due to conservative mass transfer from the companion star to the neutron star or due to mass loss from disk winds.

In case of High Mass X-ray binaries, orbital period decay occurs due to stellar wind driven angular momentum loss and/or strong tidal interactions between the binary components. Tidal interactions between binary components of Cen X–3, LMC X–4 and SMC X–1 are the primary cause of orbital period evolution because these are the short orbital period HMXBs with strong tidal effects and the mass loss rate of $10^{-7} - 10^{-6}$ $M_{\odot}$ yr^{-1} in these sources is not sufficient to account for the orbital period decay due to wind driven

angular momentum loss (Kelley et al., 1983; Levine et al., 1993, 2000). The orbital period decay estimated in these systems are of the order $(0.9 - 3.4) \times 10^{-6}$ yr^{-1} (Falanga et al., 2015). The orbital period decay seen in 4U 1700–37 is smaller than that seen in these systems, inspite of it having the largest (R$_\star$/a) ratio compared to the other binaries. On the other hand, the orbital period decay seen in OAO 1657–415, which has a larger orbital period of 10.44 days, can be explained with wind driven angular momentum loss (Jenke et al., 2012). In case of 4U 1700–37, the earlier estimate of $\dot{P}/P = -3 \times 10^{-6}$ yr^{-1} by Rubin et al. (1996) was accounted by wind driven angular momentum loss. As mentioned in Rubin et al. (1996), by taking into account the uncertainies in various factors contributing to orbital period decay due to stellar wind driven angular momentum loss, the mass loss rate can be as less as 10% of the total and the present estimated orbital period decay could be solely driven by it. It would be interesting to investigate the models evaluating the contribution of stellar wind driven angular momentum loss and tidal interactions in the orbital decay rate seen for this binary system (Lecar et al., 1976; Hut, 1981; van der Klis & Bonnet-Bidaud, 1984; Brookshaw & Tavani, 1993; van den Heuvel, 1994).

4.2.6 Eccentricity of the binary orbit

The upper limit on eccentricity of the orbit of 4U 1700–37 put from the limits of residuals in the mid-eclipse times and limits on variation in the eclipse duration is quite low; $e \sim$ 0.008 and 0.05 respectively. This is in contrast with $e \sim 0.22$ from the radial velocity measurements with *IUE* data (Hammerschlag-Hensberge et al., 2003). In the presence of a significant apsidal motion, the radial velocity measurements at different orbital phases (with respect to the mid-eclipse times) in data spread over several years can not be put together in a simple way. The *IUE* data from which an eccentricity of 0.22 was reported are not sampled densely enough for a joint fit to measure eccentricity. The present work with *Swift*-BAT indicates a nearly circular orbit for this system if the apsidal motion rate is in the range of 5-200 degrees per year. An even higher rate of apsidal motion along with a significant eccentricity can be ruled out from the fact that edges of the eclipse

ingress and egress are quite sharp. In the presence of a large apsidal motion rate and eccentricity, the edges of the eclipse profiles with *Swift*–BAT shown in the second panel of Figure 4.8 would be smoothed out. Measurement of correct orbital parameters of the system would require new radial velocity measurements with good orbital coverage in a single epoch. In addition, the LAXPC instrument of the recently launched mission *ASTROSAT* (Singh et al., 2002; Paul, 2013) will either detect or lower the upper limit of pulse fraction of 4U 1700–37 in a wide X-ray energy band of 3-80 keV. We note here that accurate determination of the orbital parameters of this source and hence the mass of the compact object, is of high interest as it is either a very high mass neutron star or a very low mass black hole (Clark et al., 2002).

Chapter 5

Effect of variability of X-ray binaries on X-ray luminosity functions of the Milky Way[1]

5.1 Introduction

X-ray emission from a normal galaxy i.e in absence of an AGN or X-ray emitting hot gas, is dominated by collective emission from its X-ray emitting point sources, majority of them being X-ray binaries (Fabbiano, 2006). The left panel of Figure 5.1 is a *Chandra* ACIS image of the Antennae galaxies, color coded to indicate the energy of the detected photons. The diffuse X-ray emission from the hot ISM is seen in red color and embedded in this diffuse X-ray emission, are the point-like X-ray sources, majority of them being X-ray binaries. In the right panel of Figure 5.1 is the number-luminosity distribution of the X-ray binary population of a galaxy also called the X-ray luminosity function (XLF).

These XLFs can also act as indicators of the star formation rate, stellar mass and evolution of these galaxies (Grimm et al., 2003; Ranalli et al., 2003; Gilfanov, 2004; Mineo et al., 2012; Kim & Fabbiano, 2010). In spite of the high angular resolution and sensitivity of these X-ray telescopes, the large distances to these galaxies limits us to

---

[1]The work presented in this Chapter is published as a paper (2016, New Astronomy, pp. 81-87)
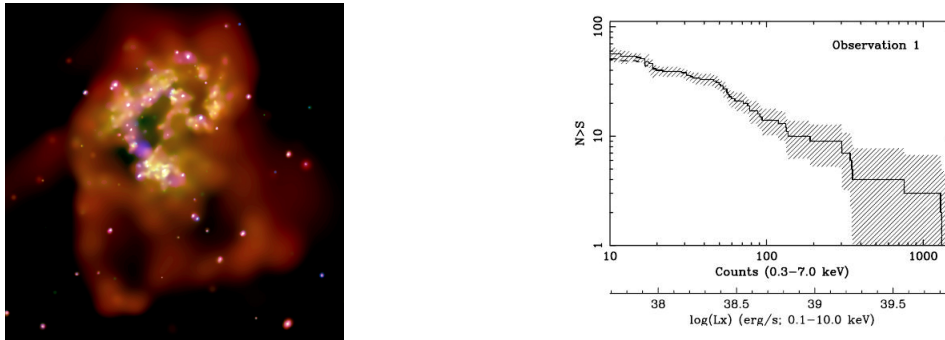
Figure 5.1: *Left Panel : Chandra* ACIS image of the interacting Antennae galaxies (NGC 4038/4039), color coded as follows: low (0.3-1 keV) as red, medium (1-2 keV) as green and high (2-8 keV) as blue. The soft X-rays are due to diffuse emission from hot ISM and the point sources are accreting X-ray binary systems.
Image credit: NASA/CXC http://chandra.harvard.edu/photo/category/galaxies.html.
Right Panel : X-ray luminosity function of the X-ray binary population in the Antennae galaxies constructed out of a *Chandra* observation. Image credit: Zezas et al. (2007).

probe higher luminosity end of their X-ray binary population. On the contrary, X-ray luminosity functions over a wide luminosities range can be constructed with the galactic X-ray binaries, the main hurdle of such an attempt being the distance uncertainity to these galactic sources. Initial attempts in constructing Log N-Log S relation for galactic X-ray binaries were made using X-ray sources from *Uhuru* catalog (Matilsky et al., 1973) and *ASCA* survey (Ogasaka et al., 1998; Sugizaki et al., 2001). Grimm et al. (2002) had constructed XLFs for X-ray binaries in Milky Way by averaging over their count-rates with the first five years of data of the *RXTE*–ASM . Galactic X-ray luminosity functions are also constructed using 15-50 keV *Swift*–BAT (Voss & Ajello, 2010) and 17-60 keV *INTEGRAL* surveys (Revnivtsev et al., 2008; Lutovinov et al., 2013).

Multiple *Chandra* and *XMM–Newton* observations show that a large fraction of sources in external galaxies are also variable and includes many transient sources (Voss & Gilfanov, 2007; Williams et al., 2006). The X-ray luminosity functions for external galaxies are constructed out of tens of kilosec exposure of *Chandra* and *XMM-Newton*

X-ray telescopes, which are essentially snapshot observations of extragalactic X-ray binaries. However, the galactic XLFs constructed by averaging luminosities of galactic X-ray binaries over 5 years of *RXTE*–ASM observations (Grimm et al., 2002), do not represent the true positions of X-ray binaries luminosities. In this Chapter, we have constructed the XLFs of Milky Way, taking into account the variability of X-ray binaries using their long term light-curves with *RXTE*–ASM .

5.2 Data and Analysis

5.2.1 Construction of differential and integral probability distributions of count-rates

The cumulative X-ray luminosity function (XLF) for the X-ray binary population in a galaxy is defined as the number distribution N($> L$) of X-ray binaries in a galaxy with luminosity greater than L, which is used throughout this Chapter. The X-ray luminosity functions for the Milky Way are constructed separately with 84 High Mass X ray Binaries and 116 Low Mass X ray Binaries whose distances are found in literature with reasonable accuracy (given in **Appendix** along with references). The light-curves of these sources are extracted from the dwell light-curves and are binned with 1 day bin time.

We quantify the variability in luminosities of each sources in the following way. We first determine the frequency of occurrence of each count rate, taking into account the errors in the count-rate given in the one day binned light-curve of each source. The errors on the count-rate in *RXTE-ASM* data consists of counting statistics along with systematic errors. For the same value of count-rate of a source, we see different values of errors in the ASM light-curves, which makes it difficult to implement Maximum Likelihood method for determination of distribution of sources in presence of systematic errors, in the form suggested by Murdoch et al. (1973). Though it is not clear if the errors in the ASM light curve are gaussian, in the absence of any obvious alternative and for the sake of simplicity, the errors are assumed to be normally distributed for each count-rate.

The true count-rate of the source corresponding to each data point in the light-curve, is then assumed to be normally distributed with the observed count rate as the mean of the distribution and the error associated with the count-rate as σ of the gaussian distribution. To find the probability distribution corresponding to true count-rate, the gaussian distribution of each data point are integrated and summed up for all events as given by Equation 5.1.

$$y(a) = \frac{1}{N} \sum_{i=1}^{N} \frac{1}{\sqrt{2\pi}\sigma_i} \int_{a-0.05}^{a+0.05} exp[\frac{-(x-c_i)^2}{2\sigma_i^2}]dx \qquad (5.1)$$

where N is the total number of data points in one day binned light-curve, c_i is the ith count rate, σ_i is the error associated with each c_i and a is the true count-rate bin along x-axis. The bin step for integration is taken to be 0.1 ASM count-rate and the integration for every true count-rate is carried out from half of the bin step preceding the count-rate (a-0.05) to half of the bin step after the count-rate (a+0.05).

The probability distribution of count-rates extending below zero obtained by this method are summed up for all datapoints and is taken to be zero. The events which are registered as NULL in the ASM count rate, are neglected in the analysis. These events indicate the absence of any measurement for example, if the source is close to the Sun.

The probability distribution of count-rates constructed by this procedure is called differential probability distribution. From differential probability distribution, integral probability distribution is constructed which denotes the probability distribution of a source having count-rate greater than the c_x (count-rate bin along X axis).

The differential and integral probability distributions are constructed for 84 High Mass X ray Binaries and 116 Low Mass X ray Binaries (including field LMXBs as well as Globular clusters LMXBs).

The distributions along with their light curves are shown for Cyg X–1 and Cyg X–3 in Figure 5.2. In Figure 5.2, the middle panel shows the comparison between differential
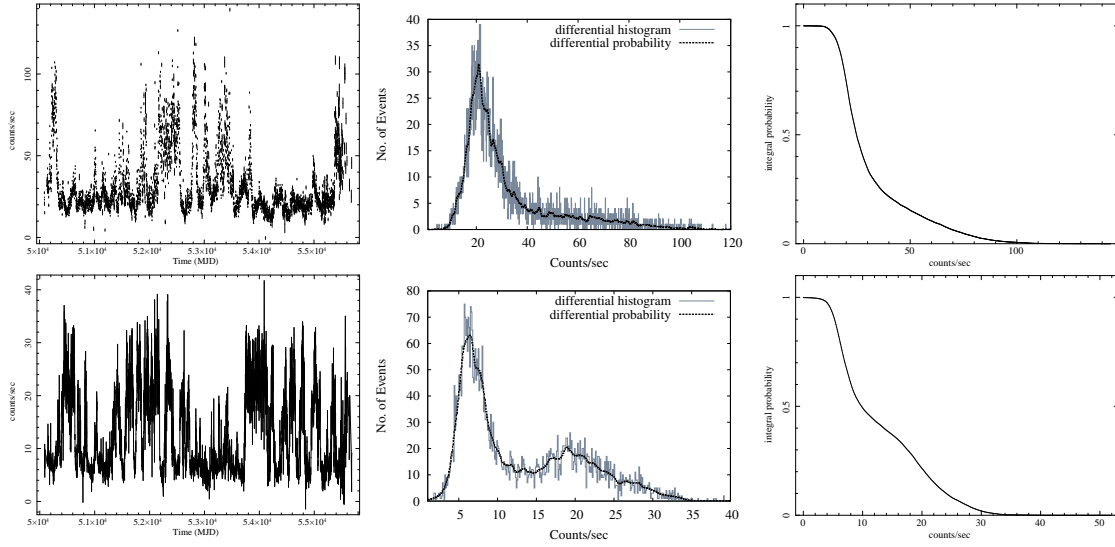
Figure 5.2: Light curve of Cyg X–1 (upper left panel) and Cyg X–3 (lower left panel), comparison between differential probability distribution and differential histogram (upper middle panel for Cyg X–1 and lower middle panel for Cyg X–3) and integral probability distribution (upper right panel for Cyg X–1 and lower right panel for Cyg X–3) are shown here.

probability distribution for Cyg X–1 and Cyg X–3 and binned differential histogram of count-rates without accounting for errors on the count-rates.

A uniformly distributed random number between 0 and 1 is then compared with the integral probability distribution of each source and the corresponding count-rate is selected. The one day binned ASM count rate is converted to flux by assuming a Crab-like spectrum for the sources and using the observed Crab count rate. The Crab flux of 2.4×10^{-8} erg cm^{-2} s^{-1} gives a count-rate of 75 counts/sec in 2-10 keV band of *RXTE–ASM* and is used for count-rate to flux conversion as given in Equation 5.2 Grimm et al. (2002).

$$F[erg s^{-1} cm^{-2}] = 3.2 \times 10^{-10}.R[\text{counts} \quad \text{s}^{-1}] \tag{5.2}$$

The flux of the sources determined by Equation 5.2 are then converted to luminosities

with their distances (given in **Appendix**), assuming an isotropic emission.

This process is repeated for each HMXB and LMXB sources and the corresponding se-
lected luminosities are then used in construction of X ray luminosity distributions for one
iteration. The XLFs constructed in this procedure are equivalent to XLFs constructed
for snapshot observations of Milky Way from the viewpoint of an outside observer.

5.2.2   Completeness Correction

Due to the flux limited nature of the ASM sample and the incompleteness in the dis-
tance measurements to the X-ray binaries, the X-ray luminosity distribution derived in
the previous section needs to be corrected for the X-ray binaries not visible to ASM. The
spatial distribution of HMXBs and LMXBs in the Milky Way is discussed in Section 1.7
in Chapter 1. Grimm et al. (2002) had constructed a model of spatial distribution of
the X-ray binaries by employing the three component model of the stellar mass distribu-
tion in the Galaxy (Bahcall & Soneira, 1980) consisting of bulge, disk and spheroid and
the parameters where chosen appropriately to model the distribution of X-ray binaries.
The HMXB spatial distribution is modeled by disk density distribution parameterized
in Dehnen & Binney (1998), with 100% modulation by galactic spiral arms densities
(spiral arms computed from Taylor & Cordes (1993)). The LMXB spatial distribution is
modeled by three component model of Bahcall & Soneira (1980), where the parameters
of bulge, disk and spheroid were appropriately chosen to fit the observed LMXB distri-
bution. The LMXB disk density distribution was 20% modulated by the galactic spiral
arm densities. Figure 5.3 is the plot of the fraction of mass visible to ASM on account
of flux limitation and distance incompleteness beyond 10 kpc.

From Equation 5.3 taken from Grimm et al. (2002)

$$(\frac{dN}{dL})_{obs} = (\frac{dN}{dL}) \times (\frac{M(< D(L))}{M_{tot}}) \tag{5.3}$$

where $\frac{dN}{dL}$ is the true luminosity function, $(\frac{dN}{dL})_{obs}$ is the flux luminosity distribution
constructed from snapshot $RXTE$–ASM measurements and $(\frac{M(<D(L))}{M_{tot}})$ is the fraction of
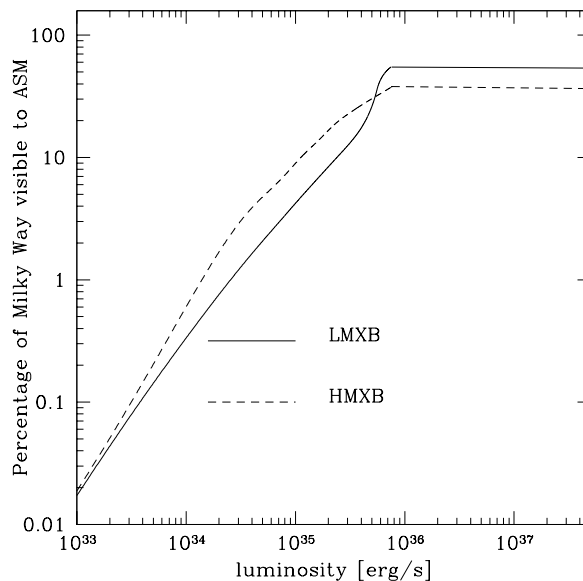
Figure 5.3: Fraction of the mass of the Galaxy visible to ASM due to flux and volume incompleteness as a function of source luminosity. Figure taken from Grimm et al. (2002).

mass visible to ASM on account of flux limitation and distance incompleteness beyond 10 kpc. From Figure 5.3, we see that both the LMXB and HMXB mass fraction has a flat part of the curve above 10^{36} ergs/s. Below 10^{36} ergs/s, the mass fraction of both LMXBs and HMXBs visible to ASM rapidly decreases. To avoid any artifacts in the snapshot luminosity functions and to ensure that the change in the parameters of the luminosity functions is introduced by the luminosity variations in the sources alone, we have constructed the galactic X-ray luminosity functions from 10^{36} to 10^{39} ergs/sec luminosity regime (flat part of the mass fraction of galaxy visible to ASM).

5.2.3 Construction of Snapshot Observations

The randomly selected luminosities of all HMXBs and LMXBs sources in one iteration are used to determine the parameters of X-ray luminosity functions for one snapshot observation. Using the same model functions as used in Grimm et al. (2002), the HMXB

distribution is then fitted with a power-law in luminosity range $10^{36} - 10^{39}$ erg/s.

$$N(> L) = K.(\frac{L}{10^{36}})^{-a} \tag{5.4}$$

The LMXB distribution is fitted with a power-law with a cut-off in the luminosity range $10^{36} - 10^{39}$ erg/s.

$$N(> L) = K.[(\frac{L}{10^{36}})^{-a} - (\frac{L_{max}}{10^{36}})^{-a}] \tag{5.5}$$

We calculate the best fit values of the parameters by using the Maximum-Likelihood (ML) method in the form suggested by Crawford et al. (1970). The main advantage of using this implementation of ML is that we use ungrouped data (luminosities) in parameter estimation. The value of slope of the power-law (power-law with a cut-off in case of LMXB) is calculated by solving the following Equation (Crawford et al., 1970)

$$\frac{M}{a} - \sum_i \ln s_i - \frac{M \ln b}{b^a - 1} = 0 \tag{5.6}$$

where M is the total number of HMXB or LMXB sources in a snapshot observation having luminosity greater than 10^{36} ergs/sec, s_i is the luminosities of each source in units of 10^{36} and b (in units of 10^{36}) is the maximum value of luminosity present in each iteration. The statistical error on slope a is Crawford et al. (1970)

$$\Sigma_a = \frac{a}{\sqrt{M}}(1 - \frac{a^2(\ln b)^2}{b^a})^{-\frac{1}{2}} \tag{5.7}$$

As mentioned in Grimm et al. (2002), the cut-off of the LMXB distribution is taken as the maximum luminosity of the sample in a given iteration. The normalisation K of the HMXB XLFs for a given iteration is taken to be the number of sources (including completeness corrections obtained from Figure 5.3) having luminosities greater than 10^{36} ergs/sec. For the LMXB XLFs, it is the number of sources (including completeness corrections obtained from Figure 5.3 greater than 10^{36} ergs/sec divided by $(1 - L_{max}^{-a})$. A plot of the XLF and the best fit model for one arbitrarily chosen iteration, without
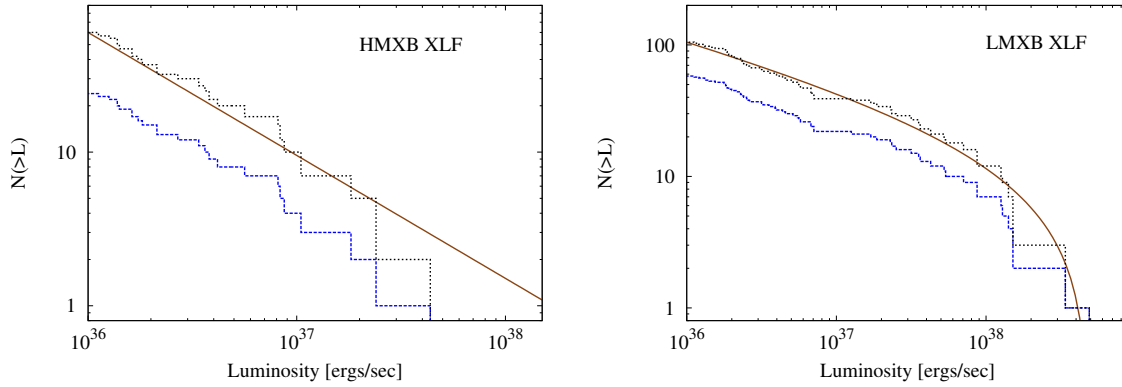
Figure 5.4: The observed (dashed line) and volume corrected (dotted line) Log N-Log L distribution of HMXB (left panel) and LMXB (right panel) for one arbitrarily chosen iteration. Solid line represents the best fit to the distribution with the parameter values obtained from M-L method, power-law model given by Equation 5.4 for HMXBs and power-law with a cut-off model given by Equation 5.5 for LMXBs.

and with completeness corrections, is shown for HMXBs and LMXBs in Figure 5.4.

Using different seeds in the random number generator, the above process is repeated 10,000 times and for each iteration, different values of slopes are obtained from Equation 5.6 along with its statistical error. The parameter values obtained for different iterations are plotted as histograms. The mean value and standard deviation (σ) of parameters are calculated from their respective histograms. The mean values of parameters along with their σ are tabulated in Table 5.1 and the histogram of parameters are shown in Figure 5.5 for LMXB XLFs and HMXB XLFs respectively. We have also calculated the mean of statistical error Σ_a on the values of slopes for each iteration.

To determine the goodness of fit of models given by Equation 5.4 to the HMXB XLFs and Equation 5.5 to the LMXB XLFs, we have performed Kolmogorov-Smirnoff test (KS test) on the data and compared it with its respective model. The average KS probability (p) value for 10000 iterations of HMXB XLFs is ~ 0.44 and the average p value for 10000 iterations of LMXB XLFs is ~ 0.41. Out of the total 10000 iterations for each type, 9359 of the HMXB XLFs and 9548 of the LMXB XLFs have $p > 0.1$.
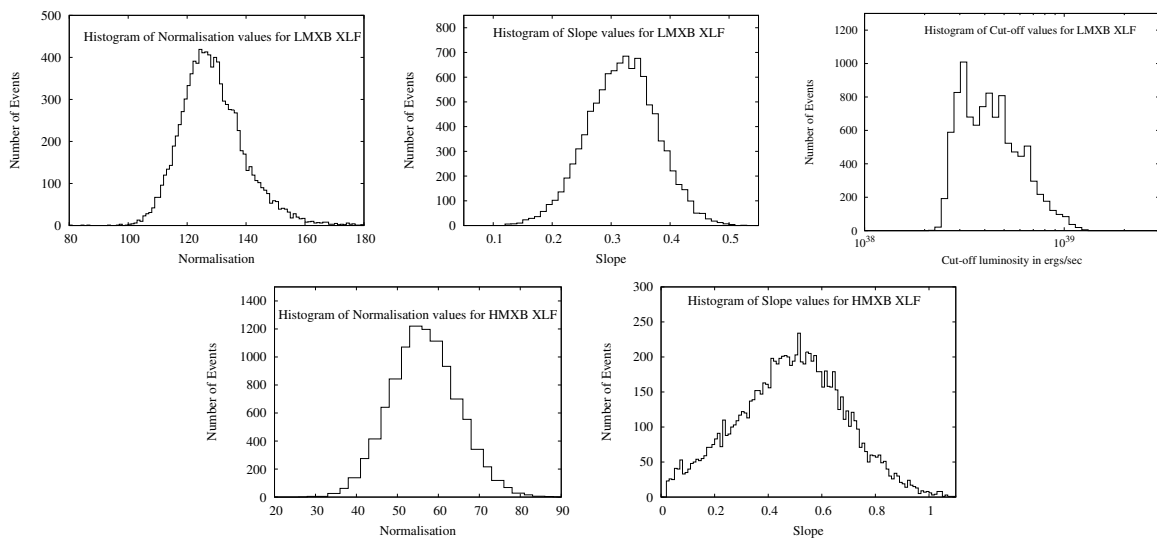
Figure 5.5: Histograms of LMXB XLFs and HMXB XLFs parameter values for 10,000 iterations. Top panel shows the distribution of Normalisation (left panel), Slope (middle panel) and Cut-off (right panel) of LMXB XLFs. Lower panel shows the distribution of Normalisation (left panel) and Slope (right panel) of HMXB XLFs.

5.3   Discussions and Conclusions

Previous work by Grimm et al. (2002) had utilized the first 5 years of *RXTE*–ASM data for constructing the averaged XLFs separately using 25 HMXBs and 84 LMXBs. However, these galactic XLFs do not include the variability effects of X-ray binaries and for a transient X-ray binary, the averaged count-rates do not represent the true

Table 5.1: Mean parameters values with their σ for 10,000 iterations. Σ_a is the averaged statistical error on the value of slope a

Sample	a	σ_a	Σ_a	K	σ_K	L_{max} (10^{38} ergs/sec)	$\sigma_{L_{max}}$ (10^{38} ergs/sec)
HMXB	0.48	0.19	0.11	54	8	-	-
LMXB	0.31	0.07	0.05	127	8	4.28	1.6

positions of such systems in the XLF. Therefore, we have used 16 years light-curves of 2-10 keV energy band of *RXTE*–ASM of 84 HMXBs and 116 LMXBs to construct multiple realizations of the XLFs for the Milky Way by incorporating the variable nature of X-ray binaries. The differential and integral probability distributions of count-rates in 2-10 keV *RXTE*–ASM light-curves are constructed for each source. The snapshot luminosity distribution are constructed separately for galactic HMXBs and LMXBs and includes completeness corrections for flux limited nature of ASM sample. For each iteration of the HMXBs, the XLF is fitted with a power-law, whereas for the LMXBs, the XLF is fitted with a power-law with cut-off. The value of slope of the power-law and power-law with cut-off is estimated from Maximum Likelihood analysis, along with the statistical error on the value of slope. This process is repeated for 10,000 realizations of XLFs of Milky Way and obtain values of XLFs parameters for all these realizations. The mean and σ of each parameter is estimated from these values of 10,000 realizations. For each realization, we also obtain the statistical error on the value of slope Σ_a, which is then averaged.

The HMXB luminosity function taking into account variability of High Mass X-ray binaries, in luminosity range $10^{36} - 10^{39}$ erg/s is given by:

$$N(> L) = (54 \pm 8)(\frac{L}{10^{36} erg/s})^{-(0.48\pm0.19)} \tag{5.8}$$

The LMXB luminosity function taking into account the variability of Low Mass X-ray binaries, in luminosity range $10^{36} - 10^{39}$ erg/s is given by:

$$N(> L) = (127 \pm 8)((\frac{L}{10^{36} erg/s})^{-(0.31\pm0.07)} - ((4.28 \pm 1.6) \times 10^3)^{-(0.31\pm0.07)}) \tag{5.9}$$

The value of σ quoted here as the spread in the value of slope for the HMXB and LMXB luminosity functions is mainly due to the variations in the XLFs arising from the variability effects of X-ray binaries. This is different from the statistical error on the value of slope Σ_a, given in Equation 5.7, arising due to finite N sample effects. As seen in Table 5.1, the spread in the slope seen due to variability of X-ray binaries is marginally

larger than the averaged Σ_a for both HMXB and LMXB XLFs.

For LMXB distribution, the most luminous source in X-rays for a given iteration determines the cut-off of the distribution. The most luminous and persistent LMXB X-ray source in 2-10 keV energy band of *RXTE*–ASM in our Galaxy is Sco X–1, which determines the cut-off of LMXB distribution for a majority of the snapshots. However, some of the galactic LMXB transients (like Aql X–1 and other Black hole binaries like GRS 1915+105) during outbursts occasionally outshines Sco X–1, which in turn influences the cut-off of the LMXB distribution for the snapshots in which such luminosities are included. As shown in Table 5.1, the cut-off of the LMXB distribution is of the order of Eddington luminosity for 1.4 $M_\odot$ neutron star in LMXB accreting Helium.

The slope of the LMXB XLF is similar to that found in previous study by Grimm et al. (2002). However, the slope of the HMXB XLF is smaller than that of HMXB XLF given in Grimm et al. (2002). This discrepancy could be due to inclusion of more Be–HMXBs in the sample, which have high luminosity during the outbursts and are non-detectable with ASM during their quiescence. Also HMXBs like LSI +61303, X Per and Supergiant Fast X-ray Transients like IGR J18483–0311, are included in some snapshot observations when they are in high luminosity states.

From Figure 5.5, we see that the slope histogram of HMXB XLFs have a larger spread than the slope histogram of LMXB XLFs. Since two-thirds of the galactic HMXB population consists of Be-HMXBs and HMXB XLFs are mostly influenced by the collective emission properties of these stellar wind driven Be-HMXB systems, we can infer that a large fraction of transients in the underlying population of HMXBs leads to larger spread in HMXB XLFs than that seen in LMXB XLFs. Postnov (2003) and Bhadkamkar & Ghosh (2012) have shown that the power law shape of the HMXB XLF can be explained by the stellar wind properties of massive stars. Most of the HMXBs systems are NS-HMXBs, with only 6 HMXB having black holes. Cyg X–1 and Cyg X–3 are the most luminous HMXB systems and therefore always occupy higher end of HMXB XLFs.

The LMXB population consists of both field LMXBs as well as Globular Clusters (GCs) LMXBs. The LMXBs in GCs have different XLF behaviour compared to field

LMXBs as seen in the study of LMXBs in the bulge of M 31 Voss & Gilfanov (2007). Since there are only 12 LMXBs in the catalogue of galactic LMXBs Liu et al. (2007), we have ignored the possible effects of LMXBs in GCs on the LMXB XLFs. The LMXB XLFs are mostly influenced by the collective emission properties of these NS-LMXBs with the break in the XLF either due to the change in the mass transfer rate in the binary systems Postnov & Kuranov (2005) or due to fraction of Giant donors in population of LMXBs Revnivtsev et al. (2011). There are also an appreciable number of transient BH LMXBs, which are either in quiescence and occupy very low luminosity states or undergo outbursts for a brief period of time and occupy high luminosity end of XLFs.

5.4   Differential probability distribution

In Section 5.2.1, we describe the procedure used for the construction of differential probability distribution of count-rates for LMXBs and HMXBs using 16 years of *RXTE*–ASM light-curves of the sources. These distribution of count-rates signify the duty cycle of these sources *i.e* the fraction of time spent by the source in a particular luminosity state for *RXTE*–ASM . Figure 5.6 and Figure 5.7 show the differential probability distribution of count-rates or luminosities of HMXBs and LMXBs respectively. While most of the sources have an exponentially falling distribution, we do see some interesting patterns for some sources in these plots. In case of HMXBs, Cyg X–1 shows a unimodal distribution with a peak around 5 $\times 10^{38}$ ergs/sec, whereas Cyg X–3 show a bimodal distribution with peaks at 10^{37} ergs/sec and 3 $\times 10^{38}$ ergs/sec. Be HMXBs like EXO 2030+375, V 0332+53, X 0115+63, X 0535+262 are transient systems and once in a while undergo huge outbursts (Figure 1.1 in Chapter 1). So their distribution of count-rates extend to higher luminosities as compared to smoothly falling profile of persistent systems like Vela X–1, Cen X–3. Some sources like some sources like Cen X–3, Her X–1 show an high luminosity abrupt cut-off in the distribution, which might indicate a saturation luminosities in their high states. In case of LMXBs, Cyg X–2, GRS 1915+105, GX 5–1, GX

13+1, GX 17+2, GX 340+0, GX 349+2, Ser X–1 and Sco X–1 show unimodal distribution whereas GX 9+1 and GX 3+1 show bimodal distribution. There are a few curious cases with a very narrow peak at higher luminosity, like for Cir X–1, GX 301–2,XTE J0421+560, X 1658-298, GX 9+9 and X 1246-588, which remains to be investigated.
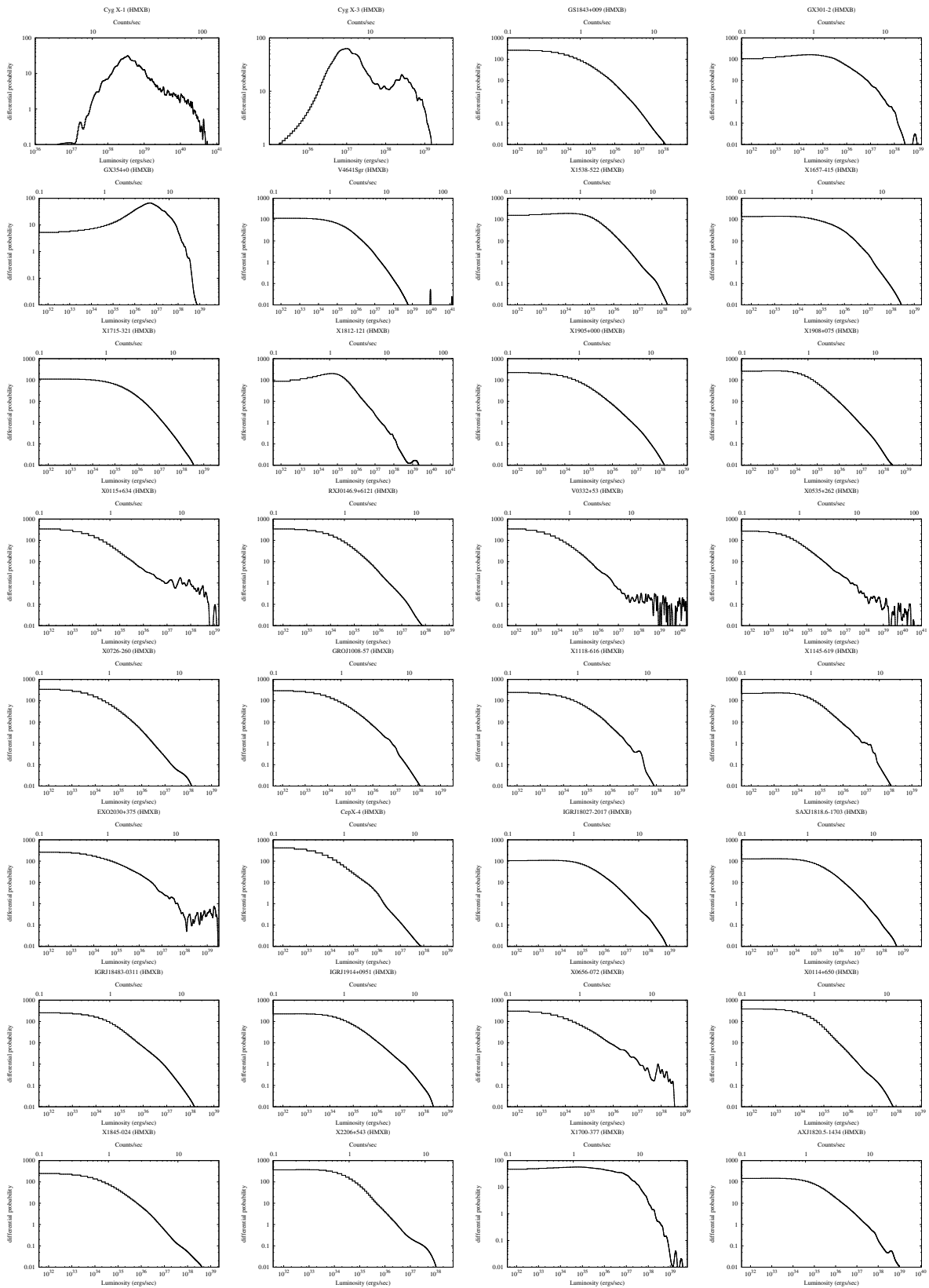
Figure 5.6: Differential probability distribution of count-rates for HMXBs constructed from 16 years *RXTE*–ASM light-curves
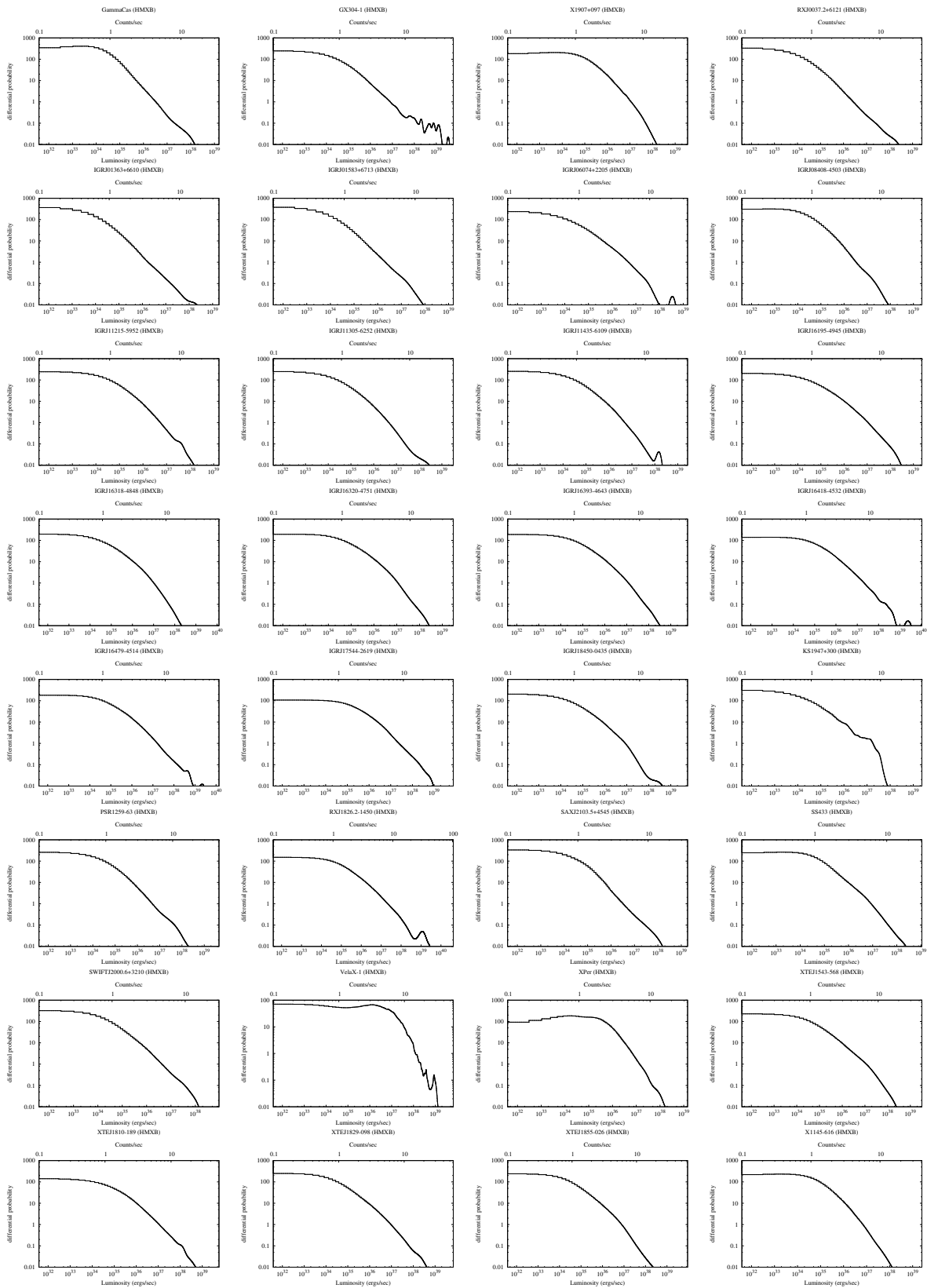
Differential probability distribution of count-rates for HMXBs constructed from 16 years *RXTE*–ASM light-curves
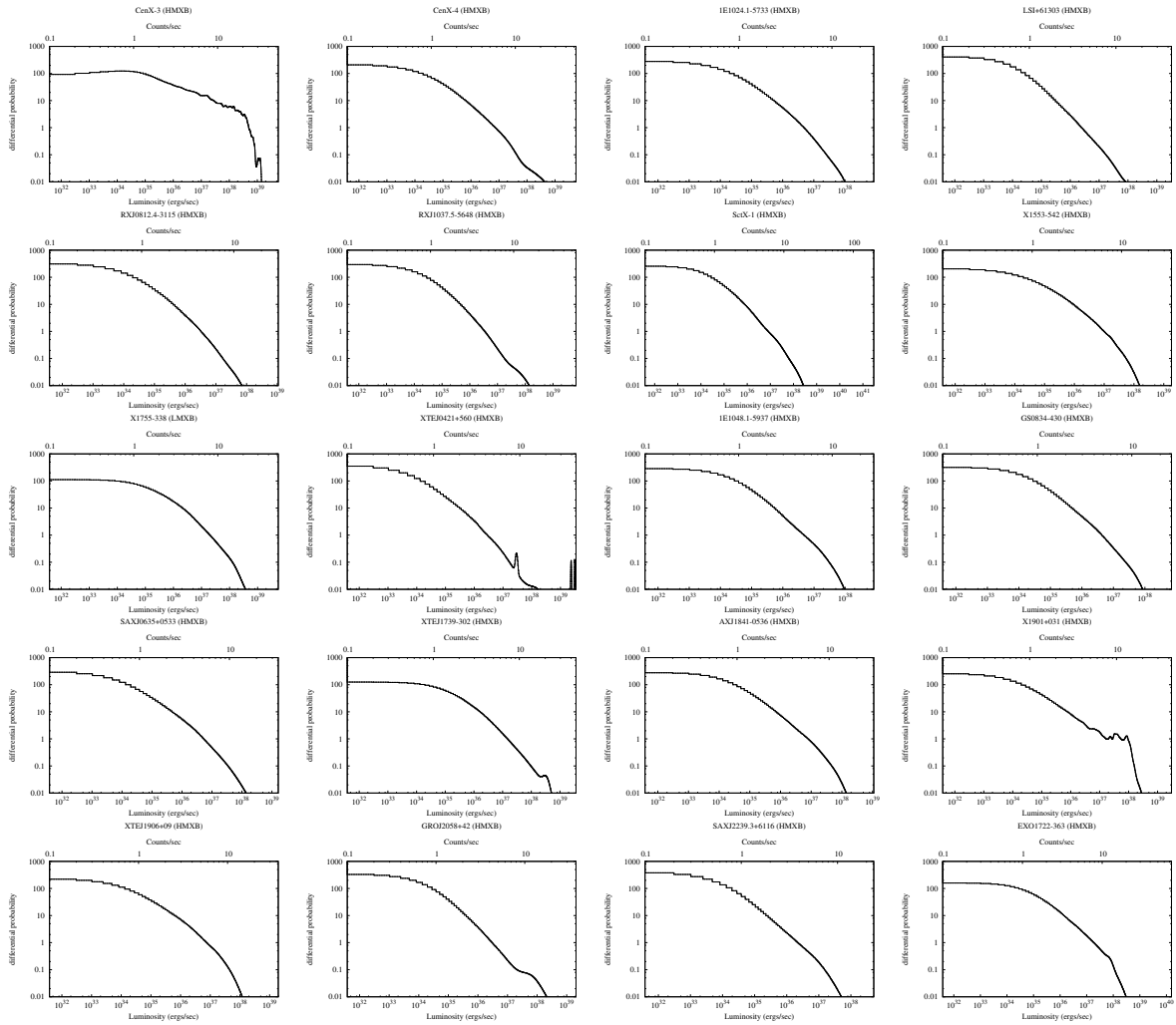
Differential probability distribution of count-rates for HMXBs constructed from 16 years *RXTE*–ASM light-curves
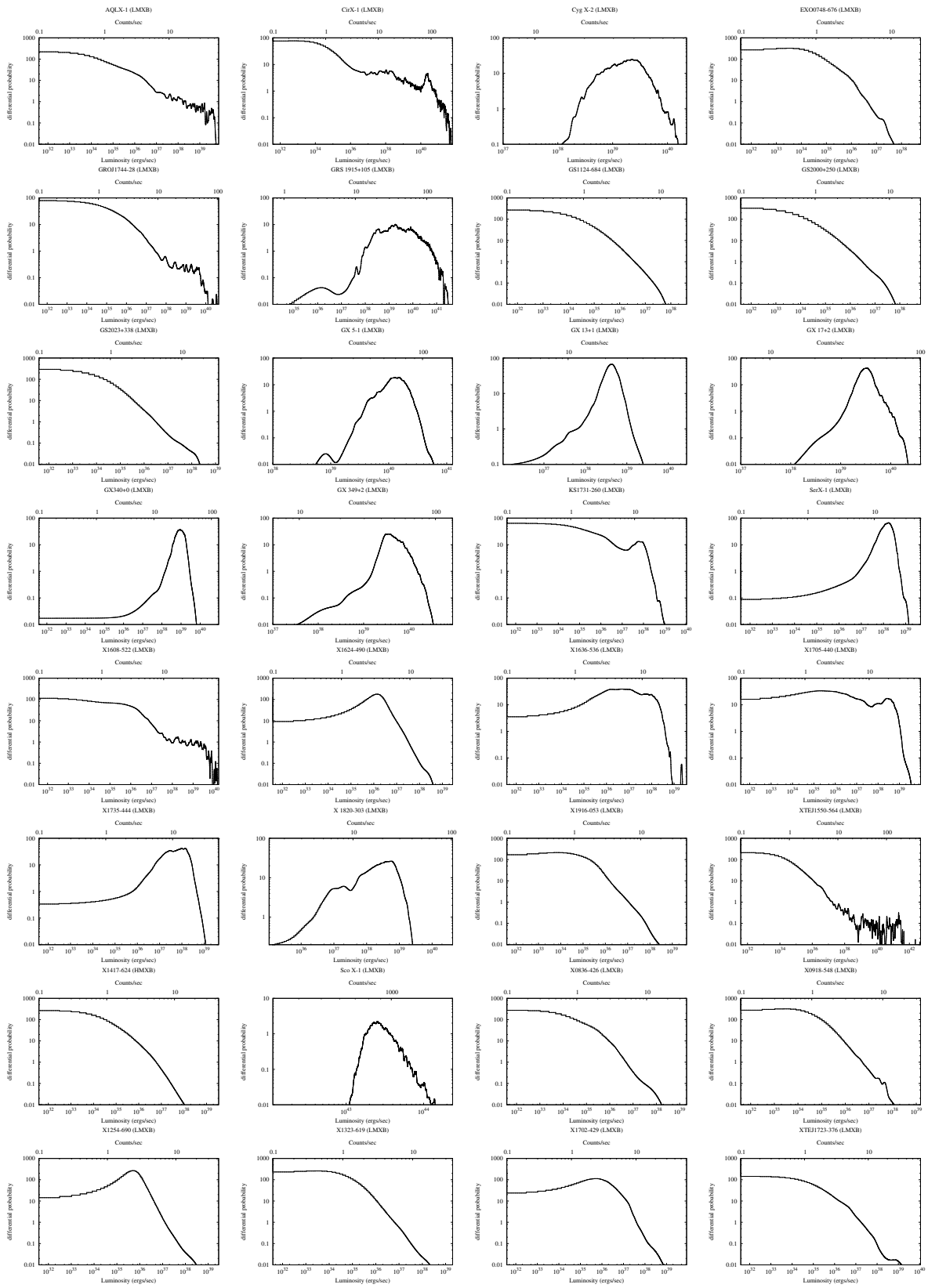
Figure 5.7: Differential probability distribution of count-rates for LMXBs constructed from 16 years *RXTE*–ASM light-curves
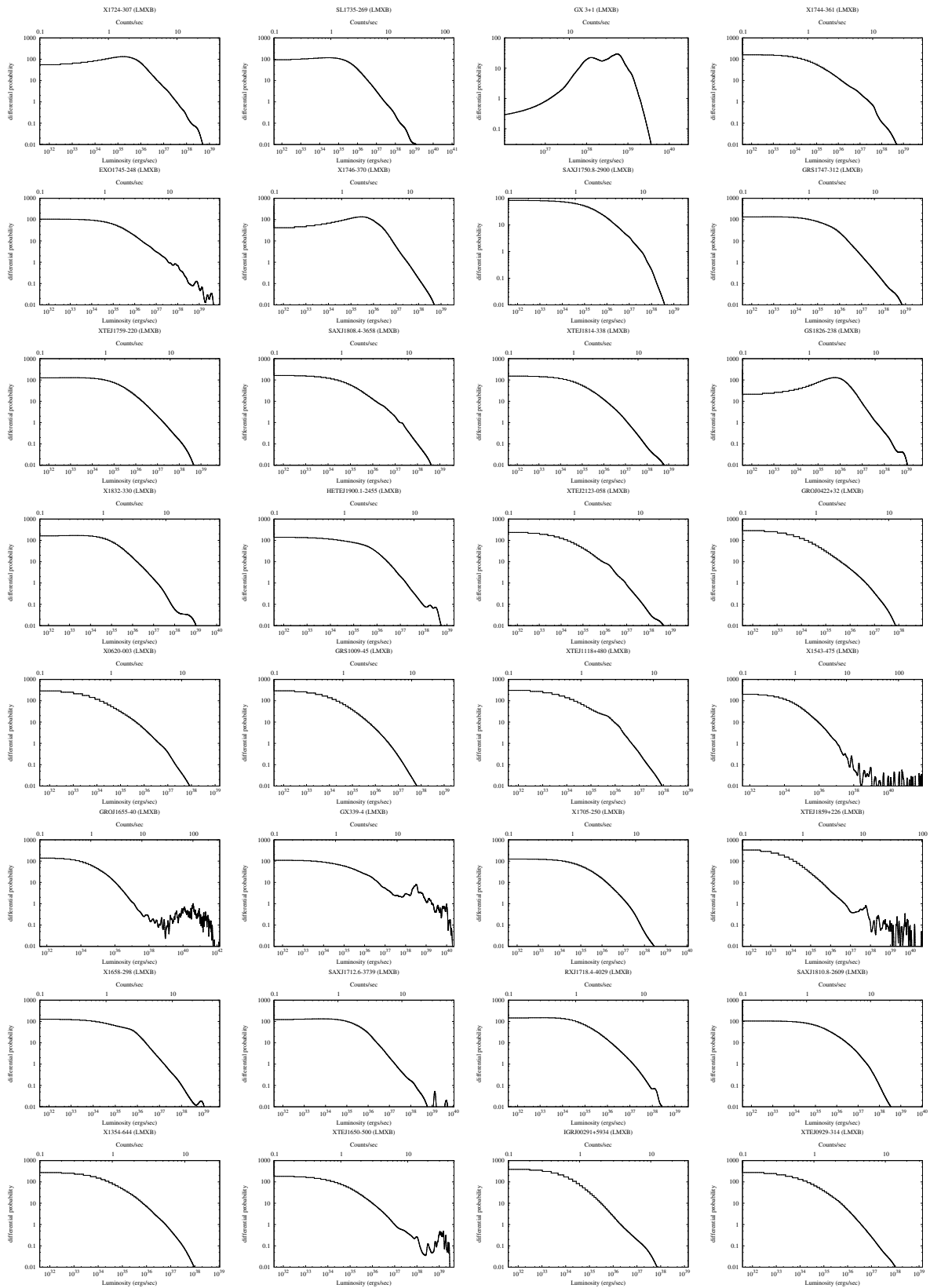
Differential probability distribution of count-rates for LMXBs constructed from 16 years *RXTE*–ASM light-curves
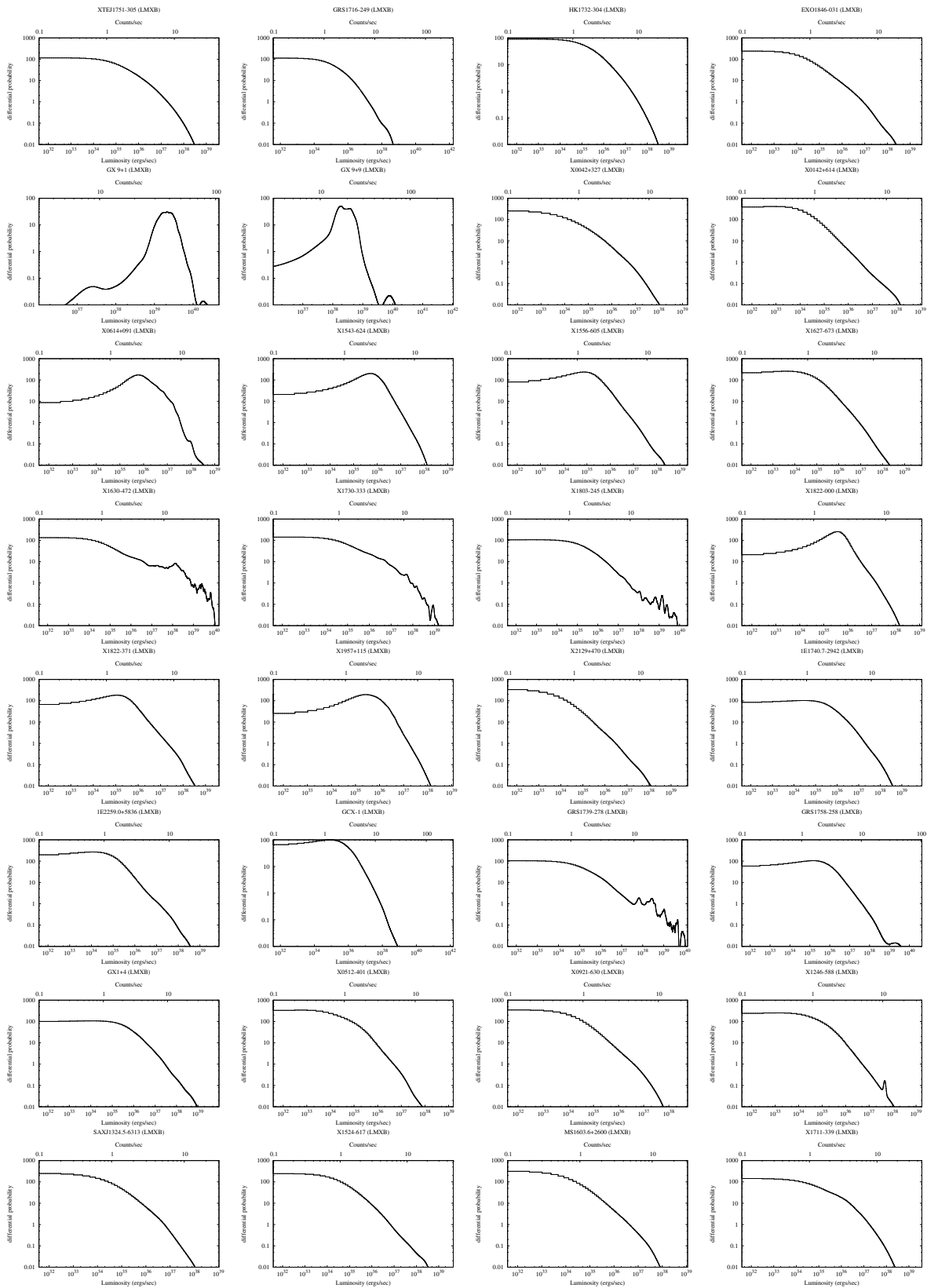
Differential probability distribution of count-rates for LMXBs constructed from 16 years *RXTE*–ASM light-curves
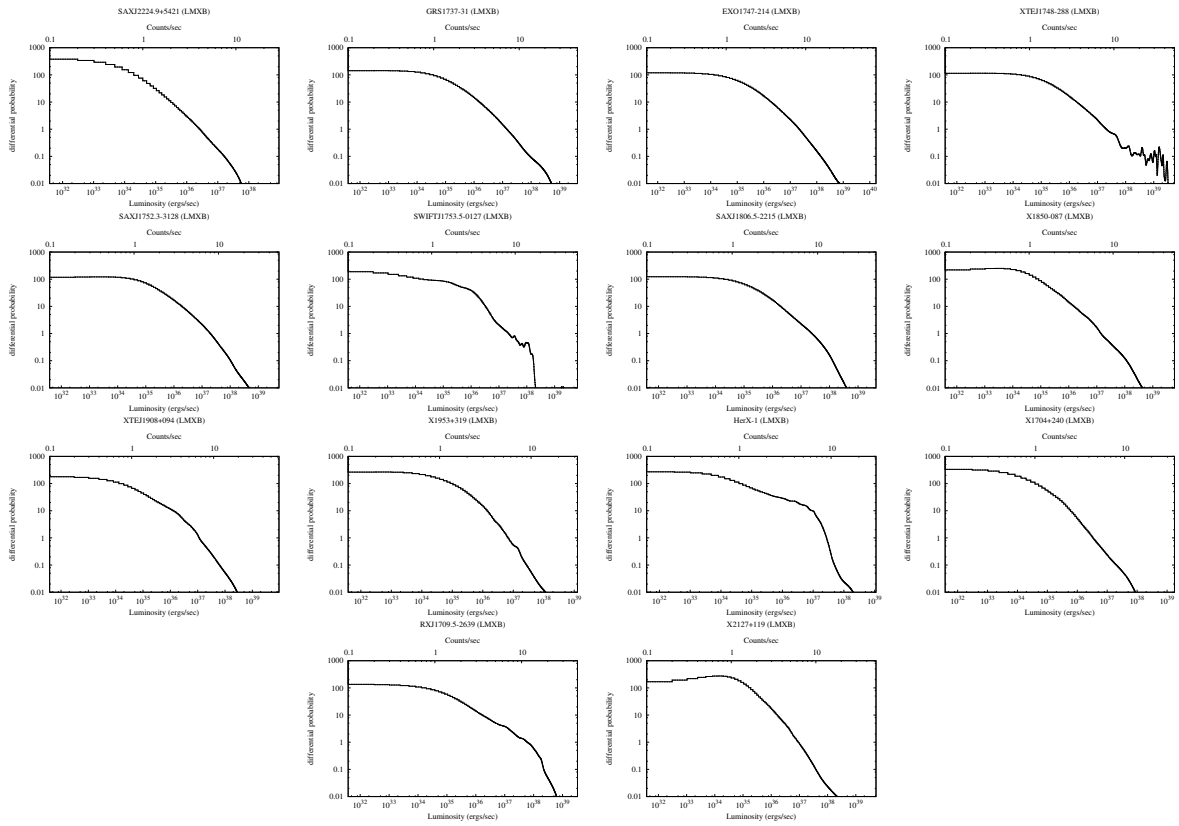
Differential probability distribution of count-rates for LMXBs constructed from 16 years *RXTE*–ASM light-curves

Appendix: Distances to X ray binaries

X ray sources	Distance(Kpc)	Type	References
AqlX-1	3.4	LMXB	van Paradijs & White (1995)
CirX-1	10.9	LMXB	van Paradijs & White (1995)
CygX-1	2.1	HMXB	Grimm et al. (2002)
CygX-2	11.3	LMXB	van Paradijs & White (1995)
CygX-3	9.0	HMXB	van Paradijs & White (1995)
EXO0748-676	7.6	LMXB	Galloway et al. (2008)
GROJ1744-28	8.5	LMXB	van Paradijs & White (1995)
GRS1915+105	12.5	LMXB	Grimm et al. (2002)
GS1124-684	5.5	LMXB	van Paradijs & White (1995)
GS1843+009	12.5	HMXB	Grimm et al. (2002)
GS2000+250	2.7	LMXB	Liu et al. (2007)
GS2023+338	4.3	LMXB	van Paradijs & White (1995)
GX5-1	7.2	LMXB	Grimm et al. (2002)
GX13+1	7.0	LMXB	Grimm et al. (2002)
GX17+2	9.5	LMXB	Galloway et al. (2008)
GX301-2	3.1	HMXB	Coleiro & Chaty (2013b)
GX340+0	11.0	LMXB	van Paradijs & White (1995)
GX349+2	9.2	LMXB	Grimm et al. (2002)
GX354+0	5.7	HMXB	Grimm et al. (2002)
KS1731-260	5.6	LMXB	Galloway et al. (2008)
SerX-1	8.4	LMXB	Grimm et al. (2002)
V4641Sgr	9.9	HMXB	Grimm et al. (2002)
X1538-522	4.5	HMXB	Bodaghee et al. (2012b)
X1608-522	4.0	LMXB	van Paradijs & White (1995)
X1624-490	13.5	LMXB	Grimm et al. (2002)
X1636-536	5.95	LMXB	Galloway et al. (2008)
X1657-415	7.1	HMXB	Bodaghee et al. (2012b)
X1705-440	7.4	LMXB	Grimm et al. (2002)
X1715-321	6.1	HMXB	Grimm et al. (2002)
X1735-444	6.5	LMXB	Galloway et al. (2008)
X1812-121	3.8	HMXB	Grimm et al. (2002)
X1820-303	4.94	LMXB	Galloway et al. (2008)
X1905+000	7.7	HMXB	Grimm et al. (2002)
X1908+075	6.4	HMXB	Grimm et al. (2002)
X1916-053	6.8	LMXB	Galloway et al. (2008)

Appendix: Distances to X ray binaries

X ray sources	Distance(Kpc)	Type	References
XTEJ1550-564	5.3	LMXB	Grimm et al. (2002)
X0115+634	5.3	HMXB	Coleiro & Chaty (2013b)
RXJ0146.9+6121	2.3	HMXB	Negueruela (1998)
V0332+53	7.0	HMXB	Negueruela (1998)
X0535+262	3.8	HMXB	Coleiro & Chaty (2013b)
X0726-260	5.0	HMXB	Coleiro & Chaty (2013b)
GROJ1008-57	5.0	HMXB	Negueruela (1998)
X1118-616	3.2	HMXB	Coleiro & Chaty (2013b)
X1145-619	4.3	HMXB	Coleiro & Chaty (2013b)
X1417-624	7.0	HMXB	Coleiro & Chaty (2013b)
EXO2030+375	3.1	HMXB	Coleiro & Chaty (2013b)
CepX-4	3.7	HMXB	Coleiro & Chaty (2013b)
ScoX-1	2.8	LMXB	Grimm et al. (2002)
X0836-426	8.2	LMXB	Galloway et al. (2008)
X0918-548	4.0	LMXB	Galloway et al. (2008)
X1254-690	15.5	LMXB	Galloway et al. (2008)
X1323-619	11.0	LMXB	Galloway et al. (2008)
X1702-429	4.19	LMXB	Galloway et al. (2008)
XTEJ1723-376	10.0	LMXB	Galloway et al. (2008)
X1724-307	5.0	LMXB	Galloway et al. (2008)
SL1735-269	5.6	LMXB	Galloway et al. (2008)
XTEJ1739-285	7.3	LMXB	Galloway et al. (2008)
SAXJ1747-2853	5.2	LMXB	Galloway et al. (2008)
IGRJ17473-2721	4.9	LMXB	Galloway et al. (2008)
SL1744-300	8.4	LMXB	Galloway et al. (2008)
GX3+1	5.0	LMXB	Galloway et al. (2008)
X1744-361	8.4	LMXB	Galloway et al. (2008)
EXO1745-248	4.73	LMXB	Galloway et al. (2008)
X1746-370	16.0	LMXB	Galloway et al. (2008)
SAXJ1750.8-2900	5.21	LMXB	Galloway et al. (2008)
GRS1747-312	9.0	LMXB	Galloway et al. (2008)
XTEJ1759-220	16.0	LMXB	Galloway et al. (2008)
SAXJ1808.4-3658	2.77	LMXB	Galloway et al. (2008)
XTEJ1814-338	7.9	LMXB	Galloway et al. (2008)
GS1826-238	6.7	LMXB	Galloway et al. (2008)

Appendix: Distances to X ray binaries

X ray sources	Distance(Kpc)	Type	References
X1832-330	6.7	LMXB	Galloway et al. (2008)
HETEJ1900.1-2455	3.6	LMXB	Galloway et al. (2008)
XTEJ2123-058	14.0	LMXB	Galloway et al. (2008)
IGRJ18027-2017	12.4	HMXB	Torrejón et al. (2010)
SAXJ1818.6-1703	2.7	HMXB	Coleiro & Chaty (2013b)
IGRJ18483-0311	2.83	HMXB	Torrejón et al. (2010)
IGRJ1914+0951	3.6	HMXB	Torrejón et al. (2010)
GROJ0422+32	2.5	LMXB	Jonker & Nelemans (2004)
X0620-003	1.2	LMXB	Jonker & Nelemans (2004)
GRS1009-45	5.7	LMXB	Jonker & Nelemans (2004)
XTEJ1118+480	1.8	LMXB	Jonker & Nelemans (2004)
X1543-475	7.5	LMXB	Jonker & Nelemans (2004)
GROJ1655-40	3.2	LMXB	Jonker & Nelemans (2004)
GX339-4	6.0	LMXB	Jonker & Nelemans (2004)
X1705-250	8.6	LMXB	Jonker & Nelemans (2004)
XTEJ1859+226	6.3	LMXB	Jonker & Nelemans (2004)
X1658-298	8.4	LMXB	Jonker & Nelemans (2004)
SAXJ1712.6-3739	5.9	LMXB	Jonker & Nelemans (2004)
RXJ1718.4-4029	6.4	LMXB	Jonker & Nelemans (2004)
SAXJ1810.8-2609	5.1	LMXB	Jonker & Nelemans (2004)
X0656-072	3.9	HMXB	Grimm et al. (2002)
X1354-644	27.0	LMXB	Wu et al. (2010)
XTEJ1650-500	2.6	LMXB	Wu et al. (2010)
IGRJ00291+5934	2.6	LMXB	Wu et al. (2010)
XTEJ0929-314	10.0	LMXB	Wu et al. (2010)
XTEJ1751-305	8.5	LMXB	Wu et al. (2010)
X0114+650	6.5	HMXB	Coleiro & Chaty (2013b)
X1845-024	10.0	HMXB	Bodaghee et al. (2012b)
X2206+543	3.4	HMXB	Coleiro & Chaty (2013b)
X1700-377	1.8	HMXB	Coleiro & Chaty (2013b)
AXJ1820.5-1434	8.2	HMXB	Bodaghee et al. (2012b)
GammaCas	0.17	HMXB	Coleiro & Chaty (2013b)
GX304-1	1.3	HMXB	Coleiro & Chaty (2013b)
X1907+097	5.0	HMXB	Bodaghee et al. (2012b)
RXJ0037.2+6121	3.0	HMXB	Bodaghee et al. (2012b)

Appendix: Distances to X ray binaries

X ray sources	Distance(Kpc)	Type	References
IGRJ01363+6610	2.0	HMXB	Bodaghee et al. (2012b)
IGRJ01583+6713	4.1	HMXB	Coleiro & Chaty (2013b)
IGRJ06074+2205	4.5	HMXB	Coleiro & Chaty (2013b)
IGRJ08408-4503	3.4	HMXB	Coleiro & Chaty (2013b)
IGRJ11215-5952	7.3	HMXB	Coleiro & Chaty (2013b)
IGRJ11305-6252	3.6	HMXB	Coleiro & Chaty (2013b)
IGRJ11435-6109	9.8	HMXB	Coleiro & Chaty (2013b)
IGRJ16195-4945	4.5	HMXB	Bodaghee et al. (2012b)
IGRJ16318-4848	1.6	HMXB	Bodaghee et al. (2012b)
IGRJ16320-4751	3.5	HMXB	Bodaghee et al. (2012b)
IGRJ16393-4643	10.6	HMXB	Bodaghee et al. (2012b)
IGRJ16418-4532	13.0	HMXB	Bodaghee et al. (2012b)
IGRJ16479-4514	2.8	HMXB	Bodaghee et al. (2012b)
IGRJ17544-2619	3.2	HMXB	Bodaghee et al. (2012b)
IGRJ18450-0435	6.4	HMXB	Coleiro & Chaty (2013b)
KS1947+300	8.5	HMXB	Coleiro & Chaty (2013b)
PSR1259-63	1.7	HMXB	Coleiro & Chaty (2013b)
RXJ1826.2-1450	2.5	HMXB	Bodaghee et al. (2012b)
SAXJ2103.5+4545	8.0	HMXB	Coleiro & Chaty (2013b)
SS433	5.5	HMXB	Bodaghee et al. (2012b)
SWIFTJ2000.6+3210	8.0	HMXB	Bodaghee et al. (2012b)
VelaX-1	2.2	HMXB	Coleiro & Chaty (2013b)
XPer	1.2	HMXB	Coleiro & Chaty (2013b)
XTEJ1543-568	10.0	HMXB	Bodaghee et al. (2012b)
XTEJ1810-189	11.5	HMXB	Bodaghee et al. (2012b)
XTEJ1829-098	10.0	HMXB	Bodaghee et al. (2012b)
XTEJ1855-026	10.8	HMXB	Coleiro & Chaty (2013b)
X1145-616	8.5	HMXB	Bodaghee et al. (2012b)
CenX-3	9.0	HMXB	Grimm et al. (2002)
CenX-4	1.6	HMXB	Grimm et al. (2002)
GRS1716-249	2.4	LMXB	Liu et al. (2001)
HK1732-304	5.2	LMXB	Liu et al. (2001)
1E1024.1-5733	3.0	HMXB	Grimm et al. (2002)
EXO1846-031	7.0	LMXB	Grimm et al. (2002)
GX9+1	7.2	LMXB	Grimm et al. (2002)

Appendix: Distances to X ray binaries

X ray sources	Distance(Kpc)	Type	References
GX9+9	7.0	LMXB	Grimm et al. (2002)
LSI+61303	2.3	HMXB	Grimm et al. (2002)
RXJ0812.4-3115	8.6	HMXB	Coleiro & Chaty (2013b)
RXJ1037.5-5648	5.0	HMXB	Grimm et al. (2002)
SctX-1	10.0	HMXB	Grimm et al. (2002)
X1630-472	4.0	LMXB	Grimm et al. (2002)
X0042+327	7.0	LMXB	Grimm et al. (2002)
X0142+614	1.0	LMXB	Grimm et al. (2002)
X0614+091	3.0	LMXB	Grimm et al. (2002)
X1543-624	10.0	LMXB	Grimm et al. (2002)
X1553-542	10.0	HMXB	Grimm et al. (2002)
X1556-605	10.0	LMXB	Grimm et al. (2002)
X1627-673	8.0	LMXB	Grimm et al. (2002)
X1730-333	8.0	LMXB	Grimm et al. (2002)
X1755-338	6.0	LMXB	Grimm et al. (2002)
X1803-245	8.0	LMXB	Grimm et al. (2002)
X1822-000	4.0	LMXB	Grimm et al. (2002)
X1822-371	2.5	LMXB	Grimm et al. (2002)
X1957+115	7.0	LMXB	Grimm et al. (2002)
X2129+470	2.2	LMXB	Grimm et al. (2002)
XTEJ0421+560	1.0	HMXB	Grimm et al. (2002)
1E1048.1-5937	3.0	HMXB	Grimm et al. (2002)
1E1740.7-2942	8.5	LMXB	Grimm et al. (2002)
1E2259.0+5836	4.0	LMXB	Grimm et al. (2002)
GCX-1	8.5	LMXB	Grimm et al. (2002)
GS0834-430	7.1	HMXB	Coleiro & Chaty (2013b)
GRS1739-278	6.0	LMXB	Grimm et al. (2002)
GRS1758-258	8.5	LMXB	Grimm et al. (2002)
GX1+4	10.0	LMXB	Grimm et al. (2002)
X0512-401	12.2	LMXB	Liu et al. (2007)
X0921-630	7.0	LMXB	Liu et al. (2007)
X1246-588	5.0	LMXB	Liu et al. (2007)
SAXJ1324.5-6313	6.2	LMXB	Liu et al. (2007)
X1524-617	4.4	LMXB	Liu et al. (2007)
MS1603.6+2600	5.0	LMXB	Liu et al. (2007)

Appendix: Distances to X ray binaries

X ray sources	Distance(Kpc)	Type	References
X1711-339	7.5	LMXB	Liu et al. (2007)
SAXJ2224.9+5421	7.1	LMXB	Liu et al. (2007)
GRS1737-31	8.5	LMXB	Liu et al. (2007)
EXO1747-214	11.0	LMXB	Liu et al. (2007)
XTEJ1748-288	8.0	LMXB	Liu et al. (2007)
SAXJ1752.3-3128	9.0	LMXB	Liu et al. (2007)
SWIFTJ1753.5-0127	6.0	LMXB	Liu et al. (2007)
SAXJ1806.5-2215	8.0	LMXB	Liu et al. (2007)
XTEJ1817-330	1.0	LMXB	Liu et al. (2007)
SAXJ1818.7+1424	9.4	LMXB	Liu et al. (2007)
X1850-087	8.2	LMXB	Liu et al. (2007)
XTEJ1908+094	3.0	LMXB	Liu et al. (2007)
X1953+319	1.7	LMXB	Liu et al. (2007)
SAXJ0635+0533	2.5	HMXB	Liu et al. (2006)
XTEJ1739-302	2.3	HMXB	Liu et al. (2006)
AXJ1841-0536	10.0	HMXB	Liu et al. (2006)
X1901+031	10.0	HMXB	Liu et al. (2006)
XTEJ1906+09	10.0	HMXB	Liu et al. (2006)
GROJ2058+42	9.0	HMXB	Liu et al. (2006)
SAXJ2239.3+6116	4.4	HMXB	Liu et al. (2006)
HerX-1	6.6	LMXB	Reynolds et al. (1997)
EXO1722-363	8.0	HMXB	Bodaghee et al. (2012b)
X1704+240	0.42	LMXB	Liu et al. (2007)
RXJ1709.5-2639	11.0	LMXB	Liu et al. (2007)
X2127+119	5.8	LMXB	Galloway et al. (2008)

Chapter 6

Long term averaged and composite spectra of Galactic X-ray binaries

6.1   Introduction

The energy spectra of X-ray binaries have been investigated during the last few decades with many observatories in different energy bands and with different energy resolutions. However, these studies are carried out in selected states of XRBs like during outbursts, transitions, quiescent states, and are always done in limited time windows of pointed observations. The wide field monitoring of all sky with *MAXI*, along with good spectral capabilities, have made it possible to investigate the true long term averaged spectral properties of X-ray binaries. Using 5 years of *MAXI*–GSC data, we have investigated long term averaged spectral properties of 57 X-ray binaries. We have also constructed the composite X-ray spectra of galactic X-ray binaries, using the same 5 years of *MAXI*–GSC data, separately for 17 HMXBs and 40 LMXBs.
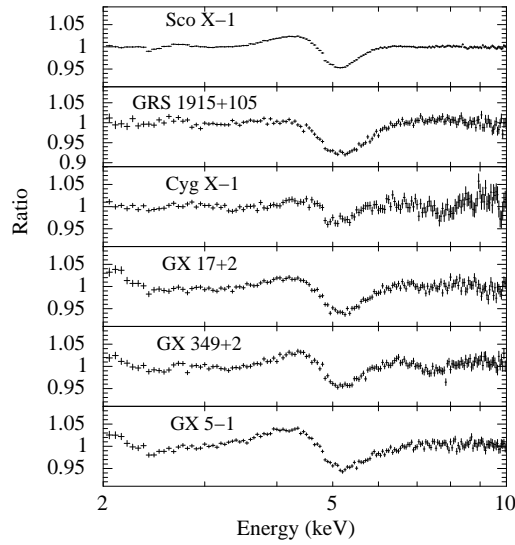
Figure 6.1: Ratio plot of data in the 2-20 keV band and the best fit model fitted ignoring the energy channels 3.0–5.5 keV. The x axis is plotted from 2–10 keV to show the strong residuals around 4.5 keV in long term averaged spectra of Sco X–1, GRS 1915+105, Cyg X–1, GX 17+2, GX 349+2, GX 5–1.

6.2 Long term averaged X-ray binaries spectrum

6.2.1 Data and Analysis

We have extracted the spectra of 57 X-ray binaries from MJD:55058 to 56970, using the *MAXI* on-demand data processing (Nakahira et al., 2012). [1] There are 17 High Mass X-ray binaries and 40 Low Mass X-ray binaries in the sample, whose long term averaged spectra is extracted and fitted with suitable models (given in Table 6.1 and Table 6.2 along with best fit parameter values). **As shown in Figure 6.1, in some of the long term averaged spectra, we see strong residuals around 4.5 keV. Contribution of these residuals in the ratio plot of the spectra is upto 8% and the nature of these residuals are unclear, though its likely to be due to instrumental effects**. We have ignored energy range 3.5–5.5 keV in such cases.

---

[1]http://maxi.riken.jp/mxondem/
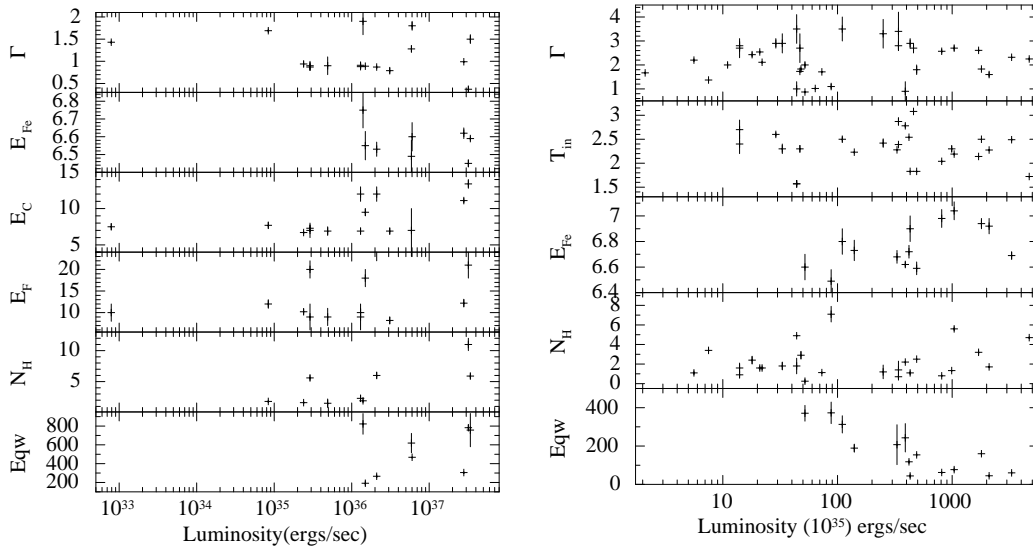
Figure 6.2: *Left Panel :* Plot of Photon index (Γ), Line energy of Fe fluorescence line (E_{Fe} in keV), cut-off energy (E_C), fold energy (E_F), equivalent column density of hydrogen (N_H in units of 10^{22} cm^{-2}) and Equivalent width of Fe fluorescence line (Eqw in units of eV) as function of luminosities of HMXBs. *Right Panel :* Plot of Photon index (Γ), inner disk temperature (E_{in} in keV), Line energy of Fe fluorescence line (E_{Fe} in keV), equivalent column density of hydrogen (N_H in units of 10^{22} cm^{-2}) and Equivalent width of Fe fluorescence line (Eqw in units of eV) as function of luminosities of LMXBs.

6.2.2 Averaged spectra of galactic HMXBs

Majority of the HMXBs are accretion powered pulsars and their averaged spectra is fitted with a spectral model consisting of a power-law with a high energy cut-off modified by photo-electric absorption by column density of absorbing matter along the line of sight. In cases where the photo-electric absorption cannot be constrained from the spectra, the nH is fixed to the column density of interstellar Galactic HI along the line of sight (DL-nH) [2]. A Fe Kα line is found present in the spectra of most of the HMXBs, which is modelled with a gaussian emission line. The residuals to the spectral fitting for Vela X–1, GX 301–2 and 4U 1700–37 shows presence of soft excess which is then modelled with a blackbody component. The long term averaged spectra of 17 HMXBs are shown

---

[2]nH tool in HEASARC: http://heasarc.gsfc.nasa.gov/cgi-bin/Tools/w3nh/w3nh.pl

in Figure 6.5 and the best fit values of the paremeters are tabulated in Table 6.1. **The best fit values of spectral parameters are plotted as function of luminosities in Figure 6.2. The least luminous sources in the sample are XPer and Gamma Cas ($\sim 10^{32}$ ergs/sec), which determines the flux completeness of the sample**.

The galactic black hole high mass X-ray binary Cyg X–1 has two distinct spectral states: high soft and low hard states (Remillard & McClintock, 2006). High soft state is dominated by thermal X-ray spectrum from the accretion disk with a weak power-law component whereas the low hard state mainly consists of a power-law spectrum. The typical photon index Γ of the power-law component in the high soft state and that in the low hard state is in the range of 1.7~3.5. The long term averaged spectrum of Cyg X–1 over both the above spectral states is described as sum of two power-laws and a multi color disk blackbody model having photon indices of $\Gamma_1 \sim$3.6 and $\Gamma_2 \sim$1.8 and an inner disk temperature of 0.5 keV. Cyg X–3, another bright HMXB BHC, is modelled by a multi color disk blackbody with inner disk temperature 1.8 keV, a blackbody with kT $\sim$ 0.2 keV and a power-law with photon index $\sim$ 1.5.

Spectra of Cyg X–1, Cyg X–3, Vela X–1, GX 301–2, Cen X–3, OAO 1657–415, IGR J18410–0535 and 4U 1700–37 show the presence of a Fe Kα line with equivalent width from 100 eV to 800 eV. The photon indices of the spectra are $\sim$ 1.0, similar to that expected for accreting X-ray pulsars with the cut-off energy E_C in the range of 5–12 keV and the fold energy E_F is in the range of 10–30 keV. For Cyg X–3, Vela X–1, GX 301–2, 4U 1538–52 and A 0535+262, the photo-electric absorption column density is of the order of 10^{23} cm^{-2}, which is much larger than the column density of interstellar Galactic HI along the line of sight. Detailed studies of the orbital dependence of absorption column density have been carried out with *MAXI* for Vela X–1 (Doroshenko et al., 2013) and 4U 1538–52 (Rodes-Roca et al., 2015), similar to that we have carried for GX 301–2 presented in Chapter 3.

6.2.3 Averaged spectra of galactic LMXBs

Since accretion in LMXBs occur due to Roche lobe overflow, forming an accretion disk around the compact object, the averaged spectra of galactic LMXBs are modelled by a multi-color disk blackbody and a power-law component modified by photo-electric absorption by column density of absorbing matter along the line of sight, **except for some sources like GX 1+4 having a high magnetic field neutron star as the compact object**. In cases where the photo-electric absorption cannot be constrained from the spectra, the nH is kept fixed to the column density of interstellar Galactic HI along the line of sight (DL-nH). Fe fluorescence line present in the spectra of some LMXBs is modelled by a gaussian emission line. The long term averaged spectra of 40 LMXBs are shown in Figure 6.6 and the best fit values of the paremeters are tabulated in Table 6.2. **The best fit values of spectral parameters are plotted as function of luminosities in Figure 6.2. The average luminosities of LMXBs is $\sim 10^{37}$ ergs/sec, an order higher than the average luminosities of HMXBs. GRS 1915+105, Sco X–1, GX 17+2, GX 349+2, GX 340+0 and GX 5–1 have average luminosities greater than 10^{38} ergs/sec.**

The long term averaged spectra of the galactic microquasar GRS 1915+105 is modelled with a spectral model consisting of a multi-color disk blackbody with an inner disk temperature 1.7 keV, a power-law component with $\Gamma \sim$ 2 and a blackbody component with kT $\sim$ 0.1 keV. The long term averaged spectra of NS LMXB Sco X–1 is modelled with a spectral model consisting of a multi-color disk blackbody with an inner disk temperature 2.3 keV, a power-law component with $\Gamma \sim$ 2.3 and a blackbody component with kT $\sim$ 0.9 keV. There are two Fe fluorescence lines present in the spectra at 6.6 keV and 7.3 keV and an equivalent width of 60 eV and 200 eV respectively.

6.2.4   Construction of Composite X-ray binary spectra

Our objective is to construct the total composite X-ray binary spectra accounting for circumstellar absorption, separately for High Mass X-ray binaries and Low Mass X-ray binaries. **Fe fluorescence lines are produced by the reprocessing of the radiation by the surrounding matter and is more related to the property of the matter than the source spectrum. Since we are interested in constructing the composite spectra from X-ray binaries, we have removed these Fe fluorescence lines from the spectra.** The total photo-electric absorption consists of column density of interstellar Galactic HI along the line of sight along with the circumstellar matter around the X-ray binary. We have removed the effect of the interstellar Galactic HI from the total photo-electric absorption and the resultant spectra are scaled to the Galactic centre distance of 8.5 kpc and then added up to construct composite X-ray binary spectra accounting for circumstellar absorption. Figure 6.3 shows the composite X-ray binary spectra constructed separately for galactic HMXB and LMXB population. Overlaid on the composite HMXB SED (left panel) are the spectra of 5 most luminous HMXBs, Cyg X–1, Cyg X–3, Cen X–3, Vela X–1 and GX 301–2 normalised to the galactic centre distance. Overlaid on the composite LMXB SED (right panel) are the spectra of 5 most luminous LMXBs, GRS 1915+105, Sco X–1, GX 5–1, GX 17+2 and GX 349+2 normalised to the galactic centre distance.

The composite HMXB SED is described empirically by the following function is the energy range of 2–20 keV.

$$
\begin{aligned}
F(E) &= 0.82 \quad E^{-1.24} \quad \text{for} \quad 2 < E < 5 keV \\
&= 1.49 \quad E^{-1.59} \quad \text{for} \quad 5 < E < 10 keV \\
&= 3.54 \quad E^{-1.95} \quad \text{for} \quad 10 < E < 20 keV \quad\quad (6.1)
\end{aligned}
$$
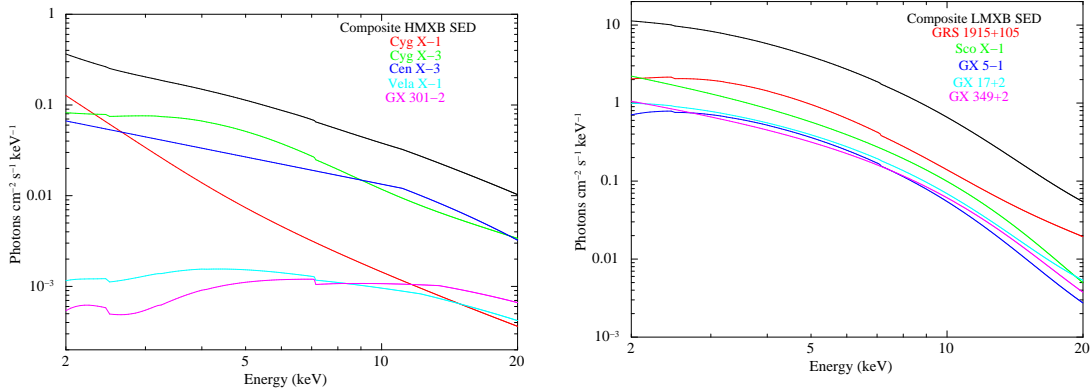
Figure 6.3: Composite HMXB SED and LMXB SED constructed out of long term averaged spectra of X-ray binaries with 5 years of monitoring with MAXI, accounting for the circumstellar absorption. Overlaid on the composite SEDs are the spectra of 5 most luminous HMXBs and LMXBs, showing their contribution to the composite X-ray binary spectra.

The composite LMXB SED is described empirically by the following function is the energy range of 2–20 keV.

$$
\begin{aligned}
F(E) &= 25.94 \quad E^{-1.08} \quad \text{for} \quad 2 < E < 5 keV \\
&= 213 \quad E^{-2.45} \quad \text{for} \quad 5 < E < 10 keV \\
&= 2629 \quad E^{-3.59} \quad \text{for} \quad 10 < E < 20 keV \quad (6.2)
\end{aligned}
$$

6.3 Implications of galactic X-ray binary spectra in extra-galactic SEDs

X-ray spectra of external galaxies consist of emission from a diverse range of X-ray emitting population (Persic & Rephaeli, 2002). In case of starbursts galaxies, at low energies E $\leq$ 2 keV, the emission is dominated by hot ISM with a steep power-law distribution of $\Gamma \sim 4$, whereas emission from X-ray binaries dominate the X-ray emission from galaxies at higher energies, having a hard X-ray spectral slope ($\Gamma \leq 2$) (Pacucci et al., 2014; Lehmer et al., 2015). Ultraluminous X-ray sources are point-like objects in
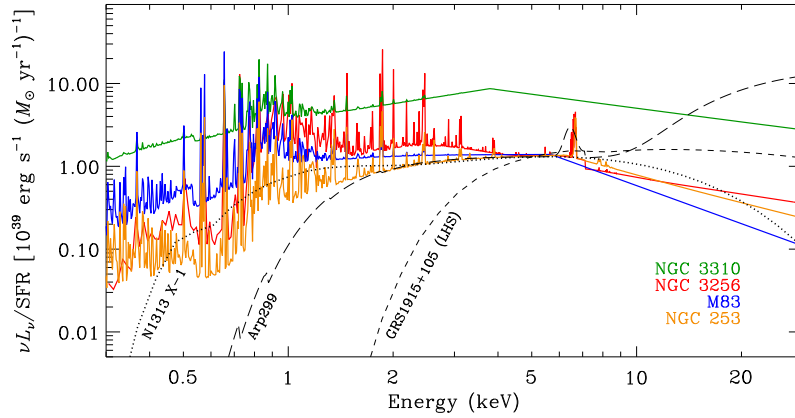
Figure 6.4: 0.3–30 keV spectral energy distribution of NGC 3256 (red), NGC 3310 (green), NGC 253 (orange), and M83 (blue) constructed out of simulataneous *Chandra / XMM–Newton* and *NuSTAR* observations. These galaxywide SEDs are compared with SEDs of an ULX N1313 X–1, a black hole binary GRS 1915+105 and a Compton thick AGN Arp 299 to estimate the contribution of various components. Figure taken from the paper by Lehmer et al. (2015).

external galaxies, with radiating at X-ray luminosity $\geq 10^{39}$ erg/sec and found to provide majority contributions to the X-ray emission from the galaxies at E $\geq$ 1–3 keV (Lehmer et al., 2015).

Figure 6.4 shows the galaxywide spectral energy distribution in energy range 0.3–30 keV for NGC 3256 (red), NGC 3310 (green), NGC 253 (orange), and M83 (blue) constructed out of simultaneous *Chandra / XMM–Newton* and *NuSTAR* observations of these galaxies (Lehmer et al., 2015). These galaxywide SEDs are compared with SEDs of an ULX N1313 X–1, a black hole binary GRS 1915+105 and a Compton thick AGN Arp 299, to estimate the contribution of various components in the SED. The composite X-ray binary spectra constructed in this work will be useful in estimating the contribution of emission from X-ray binaries in these galaxies.

6.4 Implications in EoR

About ~ 1 billion years after Big Bang, the universe underwent an "Epoch of Reionization", when the neutral hydrogen in the intergalactic medium was ionised by a background of ionising ultraviolet and X-ray photons produced by first generation of stars and galaxies (Venkatesan et al., 2001; Barkana & Loeb, 2007; Pritchard & Furlanetto, 2007). High Mass X-ray binaries are now considered important contributors to the heating and reionisation of very high redshift intergalactic medium (Power et al., 2009; Mirabel et al., 2011; Power et al., 2013). X-ray photons emitted from an accreting X-ray binary have longer mean free path than UV photons and are capable of producing several secondary ionization, thus enhancing its ionizing power. Indeed various cosmological simulations predicting the spectra of 21 cm transition of atomic hydrogen at very high redshift IGM ($z \sim 20$), utilise an input spectra to model the contribution of X-ray photons produced from HMXBs which are the remnants of primordial stars (Pritchard & Furlanetto, 2007; Power et al., 2013; Fialkov et al., 2014). However, there are disagreements related to the actual model of the input HMXB spectra used in various simulations. Pritchard & Furlanetto (2007) and Power et al. (2009) use an empirical power-law with energy-index $\alpha_s \sim 1$, whereas Mirabel et al. (2011) and Power et al. (2013) use the spectra of Cyg X–1, a galactic black hole HMXB, as the template for HMXB spectra. The most recent work by Fialkov et al. (2014) use the X-ray binary spectral energy distribution from XRBs population synthesis simulations by Fragos et al. (2013), which is motivated by *RXTE*–PCA observations of galactic neutron star and black hole binaries. These fiducial HMXB spectra do not represent the true average spectral energy distribution of HMXBs for following reasons

- RXTE PCA observations of galactic NS and BH binaries do not represent the long term averaged spectra of X-ray binaries because these are pointed observations carried in very selected states of XRBs (mentioned earlier).

- Using Cyg X-1 spectra as an input template for HMXB spectra is erroneous because it does not represent the spectral behaviour of HMXB population, which is
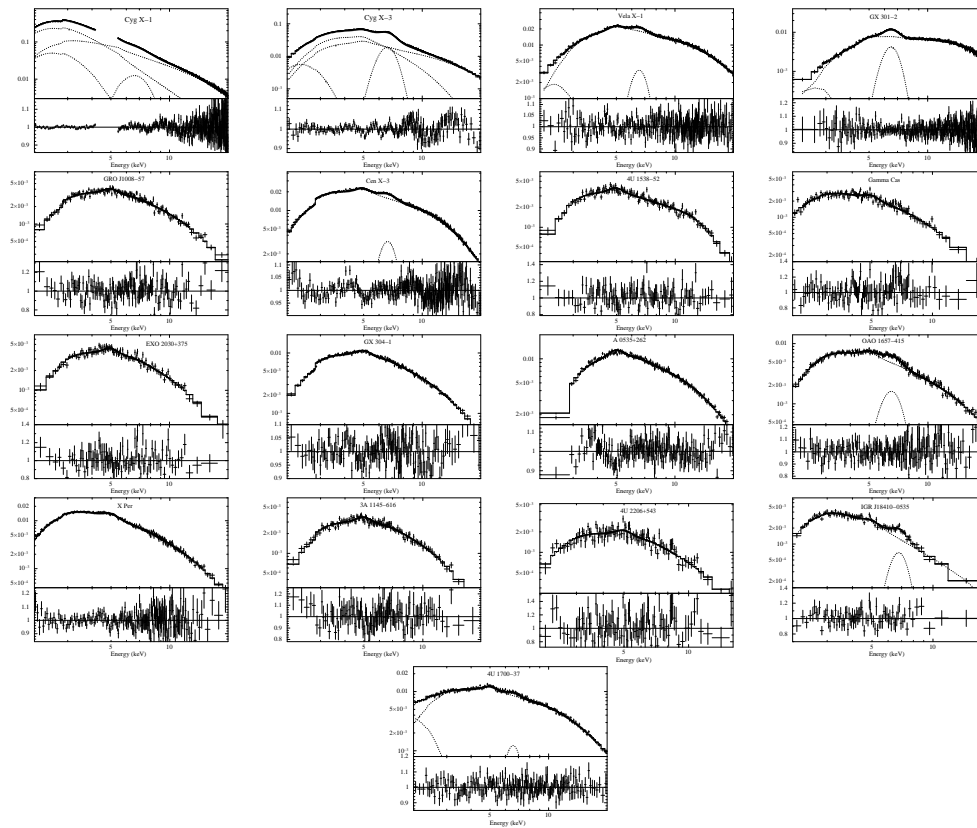
Figure 6.5: Long term averaged spectra of HMXBs along with best fit model and ratio of data and the best fit model.

dominated by accreting X-ray pulsars.

So the composite HMXB spectra, constructed from 5 years of continuous and unbiased monitoring of galactic X-ray binaries with MAXI, represent the true average HMXB spectra and it will provide realistic estimates on the fractional contribution of hard X-rays in heating of IGM and EoR.

Table 6.1: Best fit spectral parameters for long term averaged spectra of galactic HMXBs

Source	Model	Distance(kpc)	Flux (ergs cm^{-2} s^{-1})	Luminosity (ergs s^{-1})
Cyg X-1	phabs(diskbb + pow(1) + pow(2) + gaus)	1.83	1.5 $\times 10^{-8}$	6.02 $\times 10^{36}$
	nH fixed to DL-nH = 0.72			
	T_{in} = 0.52 $^{+0.09}_{-0.06}$ keV			
	Diskbb Norm = 4126$^{+7591}_{-2369}$			
	Γ_1 = 1.8 $\pm$ 0.1			
	pow(1) Norm = 1.5 $\pm$ 0.5			
	Γ_2 = 3.6 $\pm$ 0.3			
	pow(2) Norm = 22 $\pm$ 3			
	LineE = 6.60 $^{+0.09}_{-0.07}$ keV			
	Sigma = 0.89 $\pm$ 0.07 keV			
	Line flux = (3.6 $\pm$ 0.5) $\times 10^{-2}$			
	Eqw = 468 $\pm$ 26 eV			
Cyg X-3	phabs(diskbb + bbody + pow + gaus)	7.2	5.4 $\times 10^{-9}$	3.4 $\times 10^{37}$
	nH = 5.9 $\pm$ 0.4; DL-nH = 1.2			
	T_{in} = 1.76 $\pm$ 0.08 keV			
	Diskbb Norm = 18 $\pm$ 2			
	kT = 0.20 $\pm$ 0.01 keV			
	bbody Norm = 0.5 $\pm$ 0.2			
	Γ = 1.5 $\pm$ 0.1			
	pow Norm = 0.4 $\pm$ 0.2			
	LineE = 6.59 $\pm$ 0.01 keV			
	Sigma = 0.37 $\pm$ 0.02 keV			
	Line flux = (3.3 $\pm$ 0.1) $\times 10^{-2}$			
	Eqw = 757 $\pm$ 177 eV			
Vela X-1	phabs(pow*highecut + bbody + gaus)	2.2	3.7 $\times 10^{-9}$	2.1 $\times 10^{36}$
	nH = 6.0 $\pm$ 0.5; DL-nH = 0.5			
	Γ_1 = 0.87 $\pm$ 0.03			
	pow Norm = 0.11 $\pm$ 0.01			
	Cut-off energy E_C = 12 $\pm$ 1			
	Fold energy E_F = 28 $\pm$ 6			
	kT = 0.19 $\pm$ 0.02 keV			
	bbody Norm = 0.2 $\pm$ 0.1			
	LineE = 6.53 $\pm$ 0.04 keV			
	Sigma = 0.32 $\pm$ 0.09 keV			
	Line flux = (5.9 $\pm$ 0.6) $\times 10^{-3}$			
	Eqw = 266 $\pm$ 17 eV			
GX 301-2	phabs(pow*highecut + bbody + gaus)	3.1	2.2 $\times 10^{-9}$	3.2 $\times 10^{37}$
	nH = 11 $\pm$ 1; DL-nH = 1.8			
	Γ_1 = 0.37 $\pm$ 0.06			
	pow Norm = 0.021 $\pm$ 0.03			
	Cut-off energy E_C = 13.4 $\pm$ 0.6			
	Fold energy E_F = 21 $\pm$ 3			
	kT = 0.18 $\pm$ 0.04 keV			
	bbody Norm = 0.36 $\pm$ 0.2			
	LineE = 6.45 $\pm$ 0.02 keV			
	Sigma = 0.32 $\pm$ 0.04 keV			
	Line flux = (8.2 $\pm$ 0.5) $\times 10^{-3}$			
	Eqw = 783 $\pm$ 27 eV			
GRO J1008-57	phabs*pow*highecut	5.0	4.2 $\times 10^{-10}$	1.3 $\times 10^{36}$
	nH fixed to DL-nH = 1.5			
	Γ_1 = 0.88 $\pm$ 0.05			
	pow Norm = 0.018 $\pm$ 0.001			
	Cut-off energy E_C = 6.9 $\pm$ 0.4			
	Fold energy E_F = 10 $\pm$ 1			

Best fit spectral parameters for long term averaged spectra of galactic HMXBs

Source	Model	Distance(kpc)	Flux (ergs cm^{-2} s^{-1})	Luminosity (ergs s^{-1})
Cen X-3	phabs(pow*highecut + gaus)	9.0	2.9 $\times 10^{-9}$	2.8 $\times 10^{37}$
	nH fixed to DL-nH = 1.2			
	$\Gamma_1 = 0.997 \pm 0.009$			
	pow Norm = 0.119 $\pm$ 0.002			
	Cut-off energy $E_C = 11.1 \pm 0.3$			
	Fold energy $E_F = 12.2 \pm 0.9$			
	LineE = 6.62 $\pm$ 0.03 keV			
	Sigma = 0.39 $\pm$ 0.06 keV			
	Line flux = (5.5 $\pm$ 0.3) $\times 10^{-3}$			
	Eqw = 305 $\pm$ 10 eV			
4U 1538-52	phabs*pow*highecut	4.5	5.2 $\times 10^{-10}$	1.3 $\times 10^{36}$
	nH = 2.3 $\pm$ 0.5; DL-nH = 0.97			
	$\Gamma_1 = 0.91 \pm 0.07$			
	pow Norm = 0.019 $\pm$ 0.002			
	Cut-off energy $E_C = 12 \pm 1$			
	Fold energy $E_F = 9 \pm 3$			
Gamma Cas	phabs*pow*highecut	0.17	2.3 $\times 10^{-10}$	7.9 $\times 10^{32}$
	nH fixed to DL-nH = 0.48			
	$\Gamma_1 = 1.43 \pm 0.03$			
	pow Norm = 0.027 $\pm$ 0.001			
	Cut-off energy $E_C = 7.5 \pm 0.4$			
	Fold energy $E_F = 10 \pm 2$			
EXO 2030+375	phabs*pow*highecut	3.1	4.3 $\times 10^{-10}$	4.9 $\times 10^{35}$
	nH = 1.5 $\pm$ 0.7; DL-nH = 1.0			
	$\Gamma_1 = 0.9 \pm 0.2$			
	pow Norm = 0.019 $\pm$ 0.005			
	Cut-off energy $E_C = 6.9 \pm 0.6$			
	Fold energy $E_F = 9 \pm 2$			
GX 304-1	phabs*pow*highecut	1.3	1.2 $\times 10^{-9}$	2.4 $\times 10^{35}$
	nH = 1.6 $\pm$ 0.2; DL-nH = 1.1			
	$\Gamma_1 = 0.94 \pm 0.06$			
	pow Norm = 0.057 $\pm$ 0.006			
	Cut-off energy $E_C = 6.7 \pm 0.2$			
	Fold energy $E_F = 10.2 \pm 0.6$			
A 0535+262	phabs*pow*highecut	3.8	1.7 $\times 10^{-9}$	2.9 $\times 10^{36}$
	nH = 5.6 $\pm$ 0.4; DL-nH = 0.6			
	$\Gamma_1 = 0.87 \pm 0.07$			
	pow Norm = 0.064 $\pm$ 0.008			
	Cut-off energy $E_C = 7.3 \pm 0.4$			
	Fold energy $E_F = 20 \pm 2$			
OAO 1657-415	phabs(pow*highecut + gaus)	7.1	9.9 $\times 10^{-10}$	5.9 $\times 10^{36}$
	nH fixed to DL-nH = 1.7			
	$\Gamma_1 = 1.28 \pm 0.07$			
	pow Norm = 0.075 $^{+0.009}_{-0.006}$			
	Cut-off energy $E_C = 7 \pm 3$			
	Fold energy $E_F = 28 \pm 5$			
	LineE = 6.49 $^{+0.1}_{-0.08}$ keV			
	Sigma = 0.6 $\pm$ 0.1 keV			
	Line flux = (4.2 $\pm$ 0.9) $\times 10^{-3}$			
	Eqw = 619 $\pm$ 103 eV			

Best fit spectral parameters for long term averaged spectra of galactic HMXBs

Source	Model	Distance(kpc)	Flux (ergs cm^{-2} s^{-1})	Luminosity (ergs s^{-1})
X Per	phabs*pow*highecut	0.8	1.1 $\times 10^{-9}$	8.4 $\times 10^{34}$
	nH = 1.8 ± 0.2; DL-nH = 0.1			
	Γ_1 = 1.69 ± 0.04			
	pow Norm = 0.23 ± 0.02			
	Cut-off energy E$_C$ = 7.7 ± 0.4			
	Fold energy E$_F$ = 12 ± 1			
3A 1145-616	phabs*pow*highecut	8.5	3.6 $\times 10^{-10}$	3.1 $\times 10^{36}$
	nH fixed to DL-nH = 1.5			
	Γ_1 = 0.79 ± 0.06			
	pow Norm = 0.014 ± 0.001			
	Cut-off energy E$_C$ = 6.9 ± 0.4			
	Fold energy E$_F$ = 8.2 ± 0.8			
4U 2206+543	phabs*pow*highecut	3.4	2.1 $\times 10^{-10}$	2.9 $\times 10^{35}$
	nH fixed to DL-nH = 0.6			
	Γ_1 = 0.9 ± 0.1			
	pow Norm = 0.085 $^{+0.002}_{-0.005}$			
	Cut-off energy E$_C$ = 7 ± 1			
	Fold energy E$_F$ = 9 ± 3			
IGR J18410−0535	phabs(pow + gaus)	6.4	2.8 $\times 10^{-10}$	1.4 $\times 10^{36}$
	nH = 1.9 ± 0.3; DL-nH = 1.9			
	Γ_1 = 2.23 ± 0.1			
	pow Norm = 0.13 ± 0.02			
	LineE = 6.75 ± 0.1 keV			
	Sigma = 0.4 ± 0.2 keV			
	Line flux = (1.5 ± 0.3) $\times 10^{-3}$			
	Eqw = 823 ± 110 eV			
4U 1700−37	phabs(pow*highecut + bbody + gaus)	1.9	3.5 $\times 10^{-9}$	1.5 $\times 10^{36}$
	nH fixed to DL-nH = 0.74			
	Γ_1 = 0.89 ± 0.02			
	pow Norm = 0.114 ± 0.005			
	Cut-off energy E$_C$ = 9.5 ± 0.5			
	Fold energy E$_F$ = 18 ± 2			
	kT = 0.19 ± 0.02 keV			
	bbody Norm = 0.09 $^{+0.07}_{-0.04}$			
	LineE = 6.55 ± 0.08 keV			
	Sigma = 0.3 ± 0.2 keV			
	Line flux = (4.1 ± 0.1) $\times 10^{-3}$			
	Eqw = 192 ± 24 eV			

Table 6.2: Best fit spectral parameters for long term averaged spectra of galactic LMXBs

Source	Model	Distance(kpc)	Flux (ergs cm^{-2} s^{-1})	Luminosity (ergs s^{-1})
GRS 1915+105	phabs(pow + diskbb + bbody)	12.5	2.5 $\times 10^{-8}$	4.7 $\times 10^{38}$
	nH = 4.7 $\pm$ 0.1; DL-nH = 1.8			
	T$_{in}$ = 1.723 $\pm$ 0.009 keV			
	Diskbb Norm = 129 $\pm$ 5			
	Γ_1 = 2.25 $\pm$ 0.05			
	pow(1) Norm = 7 $\pm$ 1			
	kT = 0.15 $\pm$ 0.02 keV			
	bbody Norm = 5 $^{+7}_{-2}$			
Her X–1	phabs(pow + gaus)	6.6	1.0 $\times 10^{-9}$	5.2 $\times 10^{36}$
	nH = 0.25 $\pm$ 0.2; DL-nH = 0.018			
	Γ_1 = 0.87 $\pm$ 0.03			
	pow(1) Norm = 0.026 $\pm$ 0.002			
	LineE = 6.6 $\pm$ 0.1 keV			
	Sigma = 0.4 $\pm$ 0.2 keV			
	Line flux = (1.8 $\pm$ 0.3) $\times 10^{-3}$			
	Eqw = 371 $\pm$ 41 eV			
Aql X–1	phabs(pow + diskbb)	5.0	1.1 $\times 10^{-9}$	3.3 $\times 10^{36}$
	nH = 1.8 $\pm$ 0.4; DL-nH = 0.34			
	T$_{in}$ = 2.3 $\pm$ 0.1 keV			
	Diskbb Norm = 1.4 $\pm$ 0.2			
	Γ_1 = 2.9 $^{+0.4}_{-0.3}$			
	pow(1) Norm = 0.8 $^{+0.5}_{-0.3}$			
Cyg X–2	phabs(pow + diskbb + gaus)	7.2	1.3 $\times 10^{-8}$	8.1 $\times 10^{37}$
	nH = 0.8 $\pm$ 0.1; DL-nH = 0.22			
	T$_{in}$ = 2.04 $\pm$ 0.02 keV			
	Diskbb Norm = 34 $\pm$ 2			
	Γ_1 = 2.57 $\pm$ 0.08			
	pow(1) Norm = 3.1 $^{+0.7}_{-0.5}$			
	LineE = 6.98 $\pm$ 0.07 keV			
	Sigma = 0.2 $\pm$ 0.2 keV			
	Line flux = (5.7 $\pm$ 0.9) $\times 10^{-3}$			
	Eqw = 62 $\pm$ 5 eV			
GX 17+2	phabs(pow + diskbb + gaus)	9.8	1.8 $\times 10^{-8}$	2.1 $\times 10^{38}$
	nH = 1.71 $\pm$ 0.06; DL-nH = 0.93			
	T$_{in}$ = 2.275 $\pm$ 0.007 keV			
	Diskbb Norm = 38 $\pm$ 1			
	Γ_1 = 1.6 $\pm$ 0.1			
	pow(1) Norm = 0.4 $\pm$ 0.2			
	LineE = 6.92 $\pm$ 0.06 keV			
	Sigma = 0.2 $\pm$ 0.2 keV			
	Line flux = (7 $\pm$ 1) $\times 10^{-3}$			
	Eqw = 45 $\pm$ 6 eV			
GX 339–4	phabs(pow + diskbb)	6.0	1.2 $\times 10^{-9}$	5.2 $\times 10^{36}$
	nH fixed to DL-nH = 0.53			
	T$_{in}$ = 0.773 $\pm$ 0.007 keV			
	Diskbb Norm = 358 $\pm$ 12			
	Γ_1 = 2.0 $\pm$ 0.1			
	pow(1) Norm = 0.12 $\pm$ 0.03			
Cir X–1	phabs(diskbb + gaus)	10.9	9.6 $\times 10^{-10}$	1.4 $\times 10^{37}$
	nH fixed to DL-nH = 1.98			
	T$_{in}$ = 2.23 $\pm$ 0.02 keV			
	Diskbb Norm = 2.69 $\pm$ 0.09			
	LineE = 6.73 $\pm$ 0.08 keV			
	Sigma = 0.2 $\pm$ 0.2 keV			
	Line flux = (1.7 $\pm$ 0.3) $\times 10^{-3}$			
	Eqw = 189 $\pm$ 21 eV			

Best fit spectral parameters for long term averaged spectra of galactic LMXBs

Source	Model	Distance(kpc)	Flux (ergs cm^{-2} s^{-1})	Luminosity (ergs s^{-1})
GX 349+2	phabs(pow + diskbb + gaus)	8.5	2.1 $\times 10^{-8}$	1.8 $\times 10^{38}$
	nH fixed to DL-nH = 0.66			
	T$_{in}$ = 2.50 $\pm$ 0.01 keV			
	Diskbb Norm = 27.9 $\pm$ 0.5			
	Γ_1 = 1.83 $\pm$ 0.05			
	pow(1) Norm = 0.52 $\pm$ 0.05			
	LineE = 6.94 $\pm$ 0.04 keV			
	Sigma = 0.73 $\pm$ 0.07 keV			
	Line flux = (2.0 $\pm$ 0.2) $\times 10^{-2}$			
	Eqw = 160 $\pm$ 8 eV			
GS 1826−238	phabs*pow	6.7	1.35 $\times 10^{-9}$	7.3 $\times 10^{36}$
	nH = 1.13 $\pm$ 0.09; DL-nH = 0.19			
	Γ_1 = 1.71 $\pm$ 0.02			
	pow(1) Norm = 0.226 $\pm$ 0.008			
GX 340+0	phabs(pow + diskbb + gaus)	8.5	1.2 $\times 10^{-8}$	1.04 $\times 10^{38}$
	nH = 5.6 $\pm$ 0.2; DL-nH = 2.2			
	T$_{in}$ = 2.19 $\pm$ 0.02 keV			
	Diskbb Norm = 33 $\pm$ 2			
	Γ_1 = 2.7 $\pm$ 0.1			
	pow(1) Norm = 4 $\pm$ 1			
	LineE = 7.04 $\pm$ 0.07 keV			
	Sigma = 0.5 $\pm$ 0.1 keV			
	Line flux = (9 $\pm$ 2) $\times 10^{-3}$			
	Eqw = 77 $\pm$ 9 eV			
GX 5−1	phabs(pow + diskbb)	7.2	2.8 $\times 10^{-8}$	1.7 $\times 10^{38}$
	nH = 3.2 $\pm$ 0.2; DL-nH = 0.94			
	T$_{in}$ = 2.14 $\pm$ 0.01 keV			
	Diskbb Norm = 78 $\pm$ 2			
	Γ_1 = 2.61 $\pm$ 0.06			
	pow(1) Norm = 7.1 $\pm$ 0.9			
GX 13+1	phabs(pow + diskbb + gaus)	7.0	8.5 $\times 10^{-9}$	4.9 $\times 10^{37}$
	nH = 2.50 $\pm$ 0.07; DL-nH = 1.8			
	T$_{in}$ = 1.83 $\pm$ 0.01 keV			
	Diskbb Norm = 51 $\pm$ 1			
	Γ_1 = 1.8 $\pm$ 0.2			
	pow(1) Norm = 0.3 $\pm$ 0.2			
	LineE = 6.59 $\pm$ 0.05 keV			
	Sigma = 0.63 $\pm$ 0.08 keV			
	Line flux = (2 $\pm$ 1) $\times 10^{-2}$			
	Eqw = 154 $\pm$ 7 eV			
H 1735−444	phabs(pow + diskbb)	9.2	4.5 $\times 10^{-9}$	4.6 $\times 10^{37}$
	nH fixed to DL-nH = 0.3			
	T$_{in}$ = 3.08 $\pm$ 0.02 keV			
	Diskbb Norm = 2.49 $\pm$ 0.08			
	Γ_1 = 2.7 $\pm$ 0.2			
	pow(1) Norm = 0.52 $\pm$ 0.05			
Ser X−1	phabs(pow + diskbb + gaus)	8.4	5.1 $\times 10^{-9}$	4.3 $\times 10^{37}$
	nH = 1.1 $\pm$ 0.2; DL-nH = 0.47			
	T$_{in}$ = 1.83 $\pm$ 0.01 keV			
	Diskbb Norm = 7.7 $\pm$ 0.5			
	Γ_1 = 2.9 $\pm$ 0.2			
	pow(1) Norm = 2.2 $\pm$ 0.6			
	LineE = 6.9 $\pm$ 0.1 keV			
	Sigma = 0.2 $\pm$ 0.2 keV			
	Line flux = (1.7 $\pm$ 0.7) $\times 10^{-3}$			
	Eqw = 44 $\pm$ 10 eV			
4U 1608−52	phabs(pow + diskbb)	4.0	1.5 $\times 10^{-9}$	2.9 $\times 10^{36}$
	nH fixed to DL-nH = 1.9			
	T$_{in}$ = 2.60 $\pm$ 0.04 keV			
	Diskbb Norm = 1.3 $\pm$ 0.1			
	Γ_1 = 2.9 $\pm$ 0.2			
	pow(1) Norm = 0.84 $\pm$ 0.09			

Best fit spectral parameters for long term averaged spectra of galactic LMXBs

Source	Model	Distance(kpc)	Flux (ergs cm^{-2} s^{-1})	Luminosity (ergs s^{-1})
GX 9+1	phabs(diskbb + bbody)	7.2	1.6 $\times 10^{-8}$	9.9 $\times 10^{37}$
	nH = 1.33 ± 0.03; DL-nH = 0.91			
	T$_{in}$ = 2.3 $^{+0.04}_{-0.1}$ keV			
	Diskbb Norm = 31 $^{+5}_{-2}$			
	kT = 1.8 ± 0.1 keV			
	bbody Norm = (2.1 ± 0.3) $\times 10^{-2}$			
GX 9+9	phabs(pow + diskbb)	7.0	5.8 $\times 10^{-9}$	3.4 $\times 10^{37}$
	nH = 0.7 ± 0.2; DL-nH = 0.21			
	T$_{in}$ = 2.39 ± 0.03 keV			
	Diskbb Norm = 8.5 ± 0.4			
	Γ_1 = 2.8 ± 0.2			
	pow(1) Norm = 1.4 ± 0.5			
HETE J1900.1–2455	phabs*pow	3.6	7.3 $\times 10^{-10}$	1.1 $\times 10^{36}$
	nH fixed to DL-nH = 0.51			
	Γ_1 = 2.00 ± 0.01			
	pow(1) Norm = 0.205 ± 0.004			
GX 1+4	phabs(pow*highecut + gaus)	10.0	7.3 $\times 10^{-10}$	8.8 $\times 10^{36}$
	nH = 7.1 ± 0.8; DL-nH = 0.33			
	Γ_1 = 1.1 ± 0.1			
	pow Norm = (4 ± 1) $\times 10^{-2}$			
	Cut-off energy E$_C$ = 9 ± 2			
	Fold energy E$_F$ = 27 $^{+11}_{-7}$			
	LineE = 6.49 ± 0.09 keV			
	Sigma = 0.3 ± 0.2 keV			
	Line flux = (2.01 ± 0.5) $\times 10^{-3}$			
	Eqw = 373 ± 56 eV			
Sco X–1	phabs(pow + diskbb + bbody + gaus(1) + gaus(2))	2.8	3.5 $\times 10^{-7}$	3.3 $\times 10^{38}$
	nH fixed to DL-nH = 0.15			
	T$_{in}$ = 2.49 ± 0.03 keV			
	Diskbb Norm = 435 ± 27			
	Γ_1 = 2.32 ± 0.04			
	pow(1) Norm = 23 ± 1			
	kT = 0.86 ± 0.04 keV			
	bbody Norm = 0.29 ± 0.06			
	LineE(1) = 6.69 ± 0.03 keV			
	Sigma(1) = 0.31 ± 0.07 keV			
	Line flux(1) = 0.17 ± 0.03			
	Eqw(1) = 60 ± 7 eV			
	LineE(2) = 7.4 ± 0.2 keV			
	Sigma(2) = 1.3 ± 0.1 keV			
	Line flux(2) = 0.4 ± 0.1			
	Eqw(2) = 189 ± 28 eV			
SLX 1735–269	phabs*pow	5.6	5.7 $\times 10^{-10}$	2.1 $\times 10^{36}$
	nH = 1.6 ± 0.2; DL-nH = 0.48			
	Γ_1 = 2.54 ± 0.05			
	pow(1) Norm = 0.45 ± 0.04			
SWIFT J1753.5–0127	phabs(pow + diskbb)	6.0	1.1 $\times 10^{-9}$	4.7 $\times 10^{36}$
	nH fixed to DL-nH = 0.17			
	T$_{in}$ = 0.48 ± 0.08 keV			
	Diskbb Norm = 230 $^{+427}_{-123}$			
	Γ_1 = 1.73 ± 0.03			
	pow(1) Norm = 0.17 ± 0.01			

Best fit spectral parameters for long term averaged spectra of galactic LMXBs

Source	Model	Distance(kpc)	Flux (ergs cm^{-2} s^{-1})	Luminosity (ergs s^{-1})
GX 3+1	phabs(diskbb + gaus)	5.0	1.1 $\times 10^{-8}$	3.3 $\times 10^{37}$
	nH fixed to DL-nH = 1.2			
	T_{in} = 2.278 $\pm$ 0.006 keV			
	Diskbb Norm = 25.3 $\pm$ 0.2			
	LineE = 6.68 $\pm$ 0.05 keV			
	Sigma = 0.54 $\pm$ 0.08 keV			
	Line flux = (2.0 $\pm$ 0.2) $\times 10^{-2}$			
	Eqw = 207 $\pm$ 104 eV			
1H 0918–548	phabs*pow	4.0	2.9 $\times 10^{-10}$	5.6 $\times 10^{35}$
	nH = 1.1 $\pm$ 0.2; DL-nH = 0.7			
	Γ_1 = 2.20 $\pm$ 0.06			
	pow(1) Norm = 0.12 $\pm$ 0.01			
4U 1705–440	phabs(diskbb + gaus)	7.4	6.4 $\times 10^{-9}$	4.2 $\times 10^{37}$
	nH fixed to DL-nH = 0.67			
	T_{in} = 2.542 $\pm$ 0.007 keV			
	Diskbb Norm = 9.22 $\pm$ 0.09			
	LineE = 6.72 $\pm$ 0.05 keV			
	Sigma = 0.4 $\pm$ 0.1 keV			
	Line flux = (6.7 $\pm$ 0.7) $\times 10^{-3}$			
	Eqw = 118 $\pm$ 9 eV			
Terzan 2	phabs*pow	5.0	7.4 $\times 10^{-10}$	2.2 $\times 10^{36}$
	nH = 1.6 $\pm$ 0.2; DL-nH = 0.66			
	Γ_1 = 2.11 $\pm$ 0.04			
	pow(1) Norm = 0.27 $\pm$ 0.02			
4U 1254–690	phabs(pow + diskbb)	15.5	8.7 $\times 10^{-10}$	2.5 $\times 10^{37}$
	nH = 1.2 $\pm$ 0.7; DL-nH = 0.29			
	T_{in} = 2.42 $\pm$ 0.09 keV			
	Diskbb Norm = 1.2 $\pm$ 0.1			
	Γ_1 = 3.3 $\pm$ 0.6			
	pow(1) Norm = 1.2 $\pm$ 0.1			
4U 1323–619	phabs*pow	11.0	3.3 $\times 10^{-10}$	4.8 $\times 10^{36}$
	nH = 2.9 $\pm$ 0.4; DL-nH = 1.4			
	Γ_1 = 1.83 $\pm$ 0.06			
	pow(1) Norm = (7.7 $\pm$ 0.8) $\times 10^{-2}$			
4U 1746–37	phabs(pow + diskbb)	16.0	1.1 $\times 10^{-9}$	3.4 $\times 10^{37}$
	nH = 1.4 $\pm$ 0.9; DL-nH = 0.29			
	T_{in} = 2.87 $\pm$ 0.08 keV			
	Diskbb Norm = 0.79 $\pm$ 0.09			
	Γ_1 = 3.4 $\pm$ 0.8			
	pow(1) Norm = 0.59 $^{+1.6}_{-0.4}$			
1H 1556–605	phabs(pow + diskbb)	10.0	3.9 $\times 10^{-10}$	4.7 $\times 10^{36}$
	nH fixed to DL-nH = 0.29			
	T_{in} = 2.30 $\pm$ 0.07 keV			
	Diskbb Norm = 0.74 $\pm$ 0.09			
	Γ_1 = 2.7 $^{+0.8}_{-0.4}$			
	pow(1) Norm = 0.74 $\pm$ 0.09			
4U 1543–624	phabs(pow + diskbb + gaus)	10.0	8.8 $\times 10^{-10}$	1.1 $\times 10^{37}$
	nH fixed to DL-nH = 0.29			
	T_{in} = 2.50 $\pm$ 0.05 keV			
	Diskbb Norm = 1.1 $\pm$ 0.1			
	Γ_1 = 3.5 $\pm$ 0.5			
	pow(1) Norm = 0.33 $\pm$ 0.09			
	LineE = 6.8 $\pm$ 0.1 keV			
	Sigma = 0.8 $\pm$ 0.2 keV			
	Line flux = (2.1 $\pm$ 0.2) $\times 10^{-3}$			
	Eqw = 313 $\pm$ 45 eV			
4U 1626–67	phabs(pow + bbody)	8.0	8.4 $\times 10^{-10}$	6.4 $\times 10^{36}$
	nH fixed to DL-nH = 0.1			
	Γ_1 = 1.02 $\pm$ 0.03			
	pow(1) Norm = (3 $\pm$ 2) $\times 10^{-2}$			
	kT = 0.46 $\pm$ 0.04 keV			
	bbody Norm = (9 $\pm$ 1) $\times 10^{-4}$			

Best fit spectral parameters for long term averaged spectra of galactic LMXBs

Source	Model	Distance(kpc)	Flux (ergs cm^{-2} s^{-1})	Luminosity (ergs s^{-1})
4U 1630−472	phabs(pow + diskbb)	4.0	2.3 ×10^{-9}	4.4 ×10^{36}
	nH = 4.9 ± 0.1; DL-nH = 2.1			
	T$_{in}$ = 1.57 ± 0.03 keV			
	Diskbb Norm = 31 ± 2			
	Γ_1 = 1.0 ± 0.3			
	pow(1) Norm = (2 ± 1) ×10^{-2}			
4U 1822−371	phabs*pow	2.5	1.0 ×10^{-9}	7.5 ×10^{35}
	nH = 3.4 ± 0.2; DL-nH = 0.12			
	Γ_1 = 1.37 ± 0.03			
	pow(1) Norm = (9 ± 5) ×10^{-2}			
4U 1957+115	phabs(pow + diskbb)	7.0	7.5 ×10^{-10}	4.4 ×10^{36}
	nH = 1.8 ± 0.8; DL-nH = 0.13			
	T$_{in}$ = 1.57 ± 0.07 keV			
	Diskbb Norm = 7 ± 2			
	Γ_1 = 3.5 ± 0.6			
	pow(1) Norm = 0.9 ± 0.7			
H 0614+091	phabs(pow + diskbb)	3.0	1.3 ×10^{-9}	1.4 ×10^{36}
	nH = 0.9 ± 0.3; DL-nH = 0.55			
	T$_{in}$ = 2.7 ± 0.2 keV			
	Diskbb Norm = 0.6 ± 0.1			
	Γ_1 = 2.8 ± 0.2			
	pow(1) Norm = 0.9 ± 0.4			
1A 1742−294	phabs(pow + diskbb + gaus)	8.5	4.6 ×10^{-9}	3.9 ×10^{37}
	nH = 2.2 ± 0.1; DL-nH = 1.1			
	T$_{in}$ = 2.78 ± 0.04 keV			
	Diskbb Norm = 3.8 ± 0.3			
	Γ_1 = 0.9 ± 0.4			
	pow(1) Norm = (3 ± 2) ×10^{-2}			
	LineE = 6.62 ± 0.02 keV			
	Sigma = 0.11 ± 0.09 keV			
	Line flux = (9.8 ± 0.6) ×10^{-3}			
	Eqw = 243 ± 74 eV			
4U 1954+319	phabs(pow + bbody)	1.7	6.2 ×10^{-10}	2.1 ×10^{35}
	nH fixed to DL-nH = 1			
	Γ_1 = 1.67 ± 0.04			
	pow(1) Norm = (7.4 ± 0.6)×10^{-2}			
	kT = 0.238 ± 0.005 keV			
	bbody Norm = (7.1 ± 0.8) ×10^{-2}			
H 1822−000	phabs(pow + diskbb)	4.0	7.3 ×10^{-10}	1.4 ×10^{36}
	nH = 1.6 ± 0.5; DL-nH = 0.38			
	T$_{in}$ = 2.4 ± 0.2 keV			
	Diskbb Norm = 0.7 ± 0.2			
	Γ_1 = 2.7 ± 0.4			
	pow(1) Norm = 0.3 ± 0.2			
MAXI J0556−332	phabs*pow	8.5	2.1 ×10^{-10}	1.8 ×10^{36}
	nH = 2.4 ± 0.4; DL-nH = 0.03			
	Γ_1 = 2.43 ± 0.09			
	pow(1) Norm = 0.15 ± 0.02			
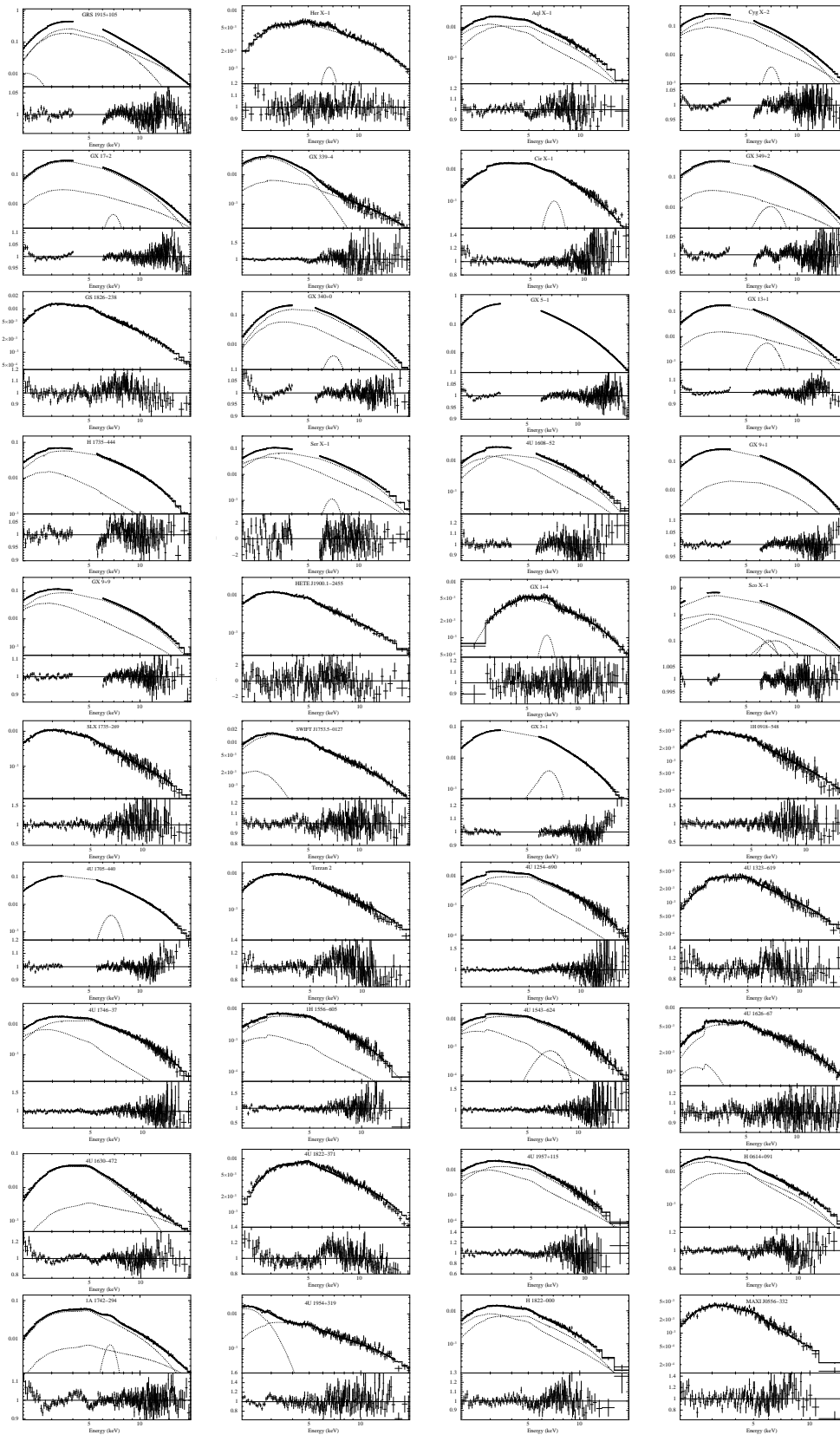
Figure 6.6: Long term averaged spectra of LMXBs along with best fit model and ratio of data and the best fit model.

Chapter 7

Summary and Future Work

7.1 Summary

In this thesis, different types of intensity variations seen in X-ray binaries using long term observations with X-ray all sky monitors are utilized to investigate certain aspects in individual systems as well as carry out X-ray binary population studies. The results from these studies are summarised below

- In Chapter 3, we investigated the energy resolved orbital intensity profiles of GX 301–2 and carried out exhaustive orbital phase resolved spectroscopic measurements of GX 301–2 with *MAXI*. Multiple orbit coverage of GX 301–2 smears out the shorter time scale variations and we can hence probe the long term behaviour of the source. The orbital variation of the spectral parameters, especially the relation between equivalent width of Fe line and column density of absorbing matter are then utilized to examine the various models about mode of accretion onto the neutron star in GX 301–2. The column density and flux of the Fe fluorescence line has a large value around the pre-periastron passage, suggesting the possible origin of X-ray flare due to enhanced mass accretion. A very large equivalent width of the iron line along with a small value of the column density in the orbital phase range 0.10-0.30 after the periastron passage indicates presence of high density absorbing

matter behind the neutron star in these orbital phase range. A large column density and strong Fe emission line together with the presence of low energy excess in orbital phases around the X-ray flare, strongly favours a high density gas stream plus a stellar wind model for mode of accretion onto the neutron star in GX 301–2 (Leahy & Kostka, 2008). The orbital dependence of column density and equivalent width of Fe line presented in this work provides stronger constraints to the dynamical wind plus stream model of Leahy & Kostka (2008).

- In Chapter 4, the presence of eclipse in two HMXBs are utilized to constrain the orbital parameters and investigate the orbital evolution of the system. For the HMXB system IGR J16393–4643, we found a short eclipse in the *Swift*–BAT light-curves and utilised it to constrain the orbital inclination of the system for possible optical counter-part: O9 supergiant star with radius 20 $R_\odot$ or a main sequence B star with radius 10 $R_\odot$. We have also studied for the first time broad-band pulsation and spectral characteristic of the system with a *Suzaku* observation, showing sub-orbital intensity variations. The broad-band pulse profiles show a complex double peaked structure with an increase in pulse fraction with energy. We also see a phase lag of the soft photons (0.3–6.0 keV and 6.0–12.0 keV) with respect to the hard photons (12–50 keV) in the energy resolved pulse profiles. The spectral characteristics of the source is similar to many accreting HMXB pulsars and has high absorbing column density of matter $\sim 10^{23}$ cm^{-2}.

4U 1700–37 is an eclipsing HMXB with a short orbital period of 3.412 days. Lack of pulsations in the system makes it difficult to measure the orbital parameters of the system especially eccentricity. We have studied the long term orbital evolution in the system using both archival mid-eclipse times as well as new mid-eclipse times from X-ray all sky monitors. The orbital period decay rate estimated is of the order of 10^{-7} yr^{-1}, an order slower than previous estimates and infact slower than other tidally interacting X-ray binaries like Cen X–3, LMC X–4 and SMC X–1, undergoing tidal interactions of similar strength. We have also utilised mid-eclipse times and eclipse durations from 10 years of *Swift*–BAT light-curves to put stronger

constraints on the eccentricity ($e \leq 0.008$) of the system, which is the first of its kind attempt.

- In Chapter 5, we have constructed X-ray luminosity functions of Milky Way including long term variability characteristics of X-ray binaries using 16 years $RXTE$–ASM light-curves. The count-rates of X-ray binaries in 16 years of $RXTE$–ASM light-curves are used to create differential and integral distribution of count-rates. These distribution of count-rates are employed to construct snapshot XLFs for mutiple iterations, separately for HMXB and LMXB population. Variability in X-ray binaries have an important contribution to the spread seen in the XLFs.

  The HMXB luminosity function taking into account variability of High Mass X-ray binaries, in luminosity range $10^{36} - 10^{39}$ erg/s is given by:

$$N(> L) = (54 \pm 8)(\frac{L}{10^{36}erg/s})^{-(0.48 \pm 0.19)} \tag{7.1}$$

  The LMXB luminosity function taking into account the variability of Low Mass X-ray binaries, in luminosity range $10^{36} - 10^{39}$ erg/s is given by:

$$N(> L) = (127 \pm 8)((\frac{L}{10^{36}erg/s})^{-(0.31 \pm 0.07)} - ((4.28 \pm 1.6) \times 10^3)^{-(0.31 \pm 0.07)}) \tag{7.2}$$

- The spectra of X-ray binaries have been previously studied by various X-ray observatories in selected states like outbursts, transitions etc and are always done in limited time windows of pointed observations. In Chapter 6, we have investigated the long term averaged spectral properties of galactic X-ray binaries with 5 years of monitoring with $MAXI$–GSC , which has the best sensitivity and highest energy resolutions amongst all operating X-ray all sky monitors. Except for Cyg X–1 and Cyg X–3, all accretion powered HMXB pulsars are modelled by a power-law with a high energy cut-off modified by a photo-electric absorption of by column density of absorbing matter along the line of sight. The LMXBs are modelled by a multi-color disk blackbody and a power-law model modified by a photo-electric absorption by column density of absorbing matter along the line of

sight. These long term averaged spectra of X-ray binaries are also used to construct composite HMXB and LMXB Spectral Energy Distributions (SEDs), accounting for the circumstellar absorption. These SEDs will be very useful in constraining the contribution of X-ray binaries in extra-galactic SEDs constructed from the simultaneous *Chandra / XMM–Newton* and *NuSTAR* observations of these galaxies. These SEDs will also serve as a useful input in estimating the contribution of XRB heating at high redshift IGM during Epoch of Reionization.

7.2 Future Work

- The orbital resolved spectroscopy of X-ray binaries with *MAXI*–GSC opens up a host of possibilities to study the long term accretion related behaviour of these systems and probe in great detail the circumstellar environment of these systems. Similar studies have been carried out for Vela X–1 (Doroshenko et al., 2013) and 4U 1538–52 (Rodes-Roca et al., 2015). We have investigated long term averaged spectra of many X-ray binaries in Chapter 6 and the results are tabulated in Table 6.1 and Table 6.2. Detailed investigation of the circumstellar matter around these some of the systems as well as the accretion processes occurring in these systems can be carried out using long term monitoring data with *MAXI*–GSC . Another important study that can be carried out using long term data from *MAXI*–GSC is super-orbital resolved spectroscopic study of Her X–1 to study the obscuration of matter along our line of sight by the precessing disk.

- In this thesis, we have probed one aspect of probable variation in XLFs due to variable nature of X-ray binaries. In case of star-bursts galaxies, the number of HMXBs present in a galaxy is related to its Star Formation Rate (SFR), whereas for elliptical galaxies, the number of LMXBs present in a galaxy is related to its stellar mass (Mineo et al., 2012). It will be interesting to probe the variation in extra-galactic XLFs due to both variability of X-ray binaries as well as the number of X-ray binaries present, which differs from galaxy to galaxy. Also we

have constructed the galactic XLFs in the energy range of 2–12 keV. In the era of hard X-ray observatories like *NuSTAR* and *Hitomi* (formerly ASTRO-H), it is essential to construct galactic XLFs in broad energy band to compare with their observations of external galaxies.

Bibliography

Abadie, J., Abbott, B. P., Abbott, R., et al. 2010, Classical and Quantum Gravity, 27, 173001

Alpar, M. A., & Shaham, J. 1985, Nature, 316, 239

Angel, J. R. P. 1979, ApJ, 233, 364

Ankay, A., Kaper, L., de Bruijne, J. H. J., et al. 2001, A&A, 370, 170

Ash, T. D. C., Reynolds, A. P., Roche, P., et al. 1999, MNRAS, 307, 357

Bahcall, J. N., & Soneira, R. M. 1980, ApJS, 44, 73

Barkana, R., & Loeb, A. 2007, Reports on Progress in Physics, 70, 627

Barthelmy, S. D., Barbier, L. M., Cummings, J. R., et al. 2005, Space Sci. Rev., 120, 143

Belczynski, K., Kalogera, V., & Bulik, T. 2002, ApJ, 572, 407

Bhadkamkar, H., & Ghosh, P. 2012, ApJ, 746, 22

Bhattacharyya, S. 2010, Advances in Space Research, 45, 949

Bird, A. J., Bazzano, A., Bassani, L., et al. 2010, ApJS, 186, 1

Bodaghee, A., Rahoui, F., Tomsick, J. A., & Rodriguez, J. 2012a, ApJ, 751, 113

Bodaghee, A., Tomsick, J. A., Rodriguez, J., & James, J. B. 2012b, ApJ, 744, 108

Bodaghee, A., Walter, R., Zurita Heras, J. A., et al. 2006, A&A, 447, 1027

Bowers, R. L., & Deeming, T. 1984, Astrophysics. Volume 1 - Stars

Bozzo, E., Falanga, M., & Stella, L. 2008, ApJ, 683, 1031

Bozzo, E., Pavan, L., Ferrigno, C., et al. 2012, A&A, 544, A118

Branduardi, G., Mason, K. O., & Sanford, P. W. 1978, MNRAS, 185, 137

Brookshaw, L., & Tavani, M. 1993, ApJ, 410, 719

Casares, J., Negueruela, I., Ribó, M., et al. 2014, Nature, 505, 378

Castor, J. I., Abbott, D. C., & Klein, R. I. 1975, ApJ, 195, 157

Cemeljic, M., & Bulik, T. 1998, Acta Astron., 48, 65

Church, M. J., Gibiec, A., & Bałucińska-Church, M. 2014, MNRAS, 438, 2784

Claret, A. 2004, A&A, 424, 919

Claret, A., & Gimenez, A. 1993, A&A, 277, 487

Clark, J. S., Goodwin, S. P., Crowther, P. A., et al. 2002, A&A, 392, 909

Coleiro, A., & Chaty, S. 2013a, ApJ, 764, 185

—. 2013b, ApJ, 764, 185

Coley, J. B., Corbet, R. H. D., & Krimm, H. A. 2015, ApJ, 808, 140

Corbet, R. H. D., & Krimm, H. A. 2013, ApJ, 778, 45

Corbet, R. H. D., Krimm, H. A., Barthelmy, S. D., et al. 2010, The Astronomer's Telegram, 2570, 1

Cowling, T. G. 1938, MNRAS, 98, 734

Crawford, D. F., Jauncey, D. L., & Murdoch, H. S. 1970, ApJ, 162, 405

Cui, W., Morgan, E. H., & Titarchuk, L. G. 1998, ApJ, 504, L27

Deeter, J. E., Boynton, P. E., Lamb, F. K., & Zylstra, G. 1987, ApJ, 314, 634

Dehnen, W., & Binney, J. 1998, MNRAS, 294, 429

Doroshenko, V., Santangelo, A., Nakahira, S., et al. 2013, A&A, 554, A37

Endo, T., Ishida, M., Masai, K., et al. 2002, ApJ, 574, 879

Evangelista, Y., Feroci, M., Costa, E., et al. 2010, ApJ, 708, 1663

Fabbiano, G. 2006, ARA&A, 44, 323

Falanga, M., Bozzo, E., Lutovinov, A., et al. 2015, A&A, 577, A130

Fialkov, A., Barkana, R., & Visbal, E. 2014, Nature, 506, 197

Fragos, T., Lehmer, B. D., Naoz, S., Zezas, A., & Basu-Zych, A. 2013, ApJ, 776, L31

Frank, J., King, A. R., & Lasota, J.-P. 1987, A&A, 178, 137

Frontera, F., & Dal Fiume, D. 1989, in ESA Special Publication, Vol. 296, Two Topics
    in X-Ray Astronomy, Volume 1: X Ray Binaries. Volume 2: AGN and the X Ray
    Background, ed. J. Hunt & B. Battrick, 57–69

Frontera, F., dal Fiume, D., Morelli, E., & Spada, G. 1985, ApJ, 298, 585

Fürst, F., Suchy, S., Kreykenbohm, I., et al. 2011, A&A, 535, A9

Galloway, D. K., Muno, M. P., Hartman, J. M., Psaltis, D., & Chakrabarty, D. 2008,
    ApJS, 179, 360

Gehrels, N., Chincarini, G., Giommi, P., et al. 2004, ApJ, 611, 1005

Giacconi, R., Gursky, H., Paolini, F. R., & Rossi, B. B. 1962, Physical Review Letters,
    9, 439

Gilfanov, M. 2004, MNRAS, 349, 146

Gimenez, A., & Garcia-Pelayo, J. M. 1983, Ap&SS, 92, 203

Grebenev, S. A., & Sunyaev, R. A. 2007, Astronomy Letters, 33, 149

Grimm, H.-J., Gilfanov, M., & Sunyaev, R. 2002, A&A, 391, 923

—. 2003, MNRAS, 339, 793

Haberl, F. 1991, ApJ, 376, 245

Haberl, F., White, N. E., & Kallman, T. R. 1989, ApJ, 343, 409

Habets, G. M. H. J., & Heintze, J. R. W. 1981, A&AS, 46, 193

Hammerschlag-Hensberge, G., van Kerkwijk, M. H., & Kaper, L. 2003, A&A, 407, 685

Harmon, B. A., Wilson, C. A., Fishman, G. J., et al. 2004, ApJS, 154, 585

Heap, S. R., & Corcoran, M. F. 1992, ApJ, 387, 340

Hickox, R. C., Narayan, R., & Kallman, T. R. 2004, ApJ, 614, 881

Hill, A. B., Walter, R., Knigge, C., et al. 2005, A&A, 439, 255

Holt, S. S. 1976, Ap&SS, 42, 123

Hut, P. 1981, A&A, 99, 126

Hutchings, J. B. 1974, ApJ, 192, 677

Ibragimov, A., Kajava, J. J. E., & Poutanen, J. 2011, MNRAS, 415, 1864

Inoue, H. 1985, Space Sci. Rev., 40, 317

in't Zand, J. J. M. 1992, PhD thesis, Space Research Organization Netherlands, Sorbonnelaan 2, 3584 CA Utrecht, The Netherlands

Jager, R., Mels, W. A., Brinkman, A. C., et al. 1997, A&AS, 125

Jain, C., Dutta, A., & Paul, B. 2008, Journal of Astrophysics and Astronomy, 28, 197

Jain, C., & Paul, B. 2011, MNRAS, 413, 2

Jain, C., Paul, B., & Dutta, A. 2010, MNRAS, 409, 755

Jenke, P. A., Finger, M. H., Wilson-Hodge, C. A., & Camero-Arranz, A. 2012, ApJ, 759, 124

Jones, C., Forman, W., Tananbaum, H., et al. 1973, ApJ, 181, L43

Jonker, P. G., & Nelemans, G. 2004, MNRAS, 354, 355

Kallman, T. R., Palmeri, P., Bautista, M. A., Mendoza, C., & Krolik, J. H. 2004, ApJS, 155, 675

Kaper, L., van der Meer, A., & Najarro, F. 2006, A&A, 457, 595

Kaur, R., Paul, B., Raichur, H., & Sagar, R. 2007, ApJ, 660, 1409

Kawai, N., Tomida, H., Yatsu, Y., et al. 2014, in Proc. SPIE, Vol. 9144, Space Telescopes and Instrumentation 2014: Ultraviolet to Gamma Ray, 91442P

Kelley, R. L., Rappaport, S., Clark, G. W., & Petro, L. D. 1983, ApJ, 268, 790

Kim, D.-W., & Fabbiano, G. 2010, ApJ, 721, 1523

Koh, D. T., Bildsten, L., Chakrabarty, D., et al. 1997, ApJ, 479, 933

Kopal, Z., ed. 1978, Astrophysics and Space Science Library, Vol. 68, Dynamics of close binary systems

Kotze, M. M., & Charles, P. A. 2012, MNRAS, 420, 1575

Koyama, K., Tsunemi, H., Dotani, T., et al. 2007, PASJ, 59, 23

Krimm, H. A., Holland, S. T., Corbet, R. H. D., et al. 2013, ApJS, 209, 14

Krivonos, R., Tsygankov, S., Lutovinov, A., et al. 2012, A&A, 545, A27

La Barbera, A., Segreto, A., Santangelo, A., Kreykenbohm, I., & Orlandini, M. 2005, A&A, 438, 617

Layton, J. T., Blondin, J. M., Owen, M. P., & Stevens, I. R. 1998, New A, 3, 111

Leahy, D. A. 2002, A&A, 391, 219

Leahy, D. A., & Creighton, J. 1993, MNRAS, 263, 314

Leahy, D. A., & Kostka, M. 2008, MNRAS, 384, 747

Leahy, D. A., & Matsuoka, M. 1990, ApJ, 355, 627

Lecar, M., Wheeler, J. C., & McKee, C. F. 1976, ApJ, 205, 556

Lehmer, B. D., Tyler, J. B., Hornschemeier, A. E., et al. 2015, ApJ, 806, 126

Levine, A., Rappaport, S., Deeter, J. E., Boynton, P. E., & Nagase, F. 1993, ApJ, 410, 328

Levine, A. M., Bradt, H., Cui, W., et al. 1996, ApJ, 469, L33

Levine, A. M., Bradt, H. V., Chakrabarty, D., Corbet, R. H. D., & Harris, R. J. 2011, ApJS, 196, 6

Levine, A. M., Rappaport, S. A., & Zojcheski, G. 2000, ApJ, 541, 194

Lewin, W. H. G., van Paradijs, J., & Taam, R. E. 1993, Space Sci. Rev., 62, 223

Liu, Q. Z., van Paradijs, J., & van den Heuvel, E. P. J. 2001, A&A, 368, 1021

—. 2006, A&A, 455, 1165

—. 2007, A&A, 469, 807

Lutovinov, A., Revnivtsev, M., Gilfanov, M., et al. 2005, A&A, 444, 821

Lutovinov, A. A., Revnivtsev, M. G., Tsygankov, S. S., & Krivonos, R. A. 2013, MNRAS, 431, 327

Maitra, C. 2013, PhD thesis, , Dept. of Physics, Indian Institute of Science, (2013)

Maitra, C., & Paul, B. 2013, ApJ, 763, 79

Makino, F., Leahy, D. A., & Kawai, N. 1985, Space Sci. Rev., 40, 421

Makishima, K. 1986, in Lecture Notes in Physics, Berlin Springer Verlag, Vol. 266, The Physics of Accretion onto Compact Objects, ed. K. O. Mason, M. G. Watson, & N. E. White, 249

Mason, A. B., Clark, J. S., Norton, A. J., et al. 2012, MNRAS, 422, 199

Mason, K. O., Branduardi, G., & Sanford, P. 1976, ApJ, 203, L29

Matilsky, T., Gursky, H., Kellogg, E., et al. 1973, ApJ, 181, 753

Matsuoka, M., Kawasaki, K., Ueno, S., et al. 2009, PASJ, 61, 999

Merloni, A., Predehl, P., Becker, W., et al. 2012, ArXiv e-prints

Mihara, T. 1995, PhD thesis, , Dept. of Physics, Univ. of Tokyo (M95), (1995)

Mihara, T., Nakajima, M., Sugizaki, M., et al. 2011, PASJ, 63, 623

Mineo, S., Gilfanov, M., & Sunyaev, R. 2012, MNRAS, 419, 2095

Mirabel, I. F., Dijkstra, M., Laurent, P., Loeb, A., & Pritchard, J. R. 2011, A&A, 528, A149

Mukherjee, U., & Paul, B. 2004, A&A, 427, 567

Mukherjee, U., Raichur, H., Paul, B., Naik, S., & Bhatt, N. 2006, Journal of Astrophysics and Astronomy, 27, 411

Murdoch, H. S., Crawford, D. F., & Jauncey, D. L. 1973, ApJ, 183, 1

Nagase, F. 1989, PASJ, 41, 1

Naik, S., Maitra, C., Jaisawal, G. K., & Paul, B. 2013, ApJ, 764, 158

Naik, S., & Paul, B. 2003, A&A, 401, 265

—. 2004, ApJ, 600, 351

Naik, S., Paul, B., & Callanan, P. J. 2005, ApJ, 618, 866

Nakahira, S., Koyama, S., Ueda, Y., et al. 2012, PASJ, 64, 13

Negueruela, I. 1998, A&A, 338, 505

Negueruela, I., Reig, P., Coe, M. J., & Fabregat, J. 1998, A&A, 336, 251

Nolan, P. L., Abdo, A. A., Ackermann, M., et al. 2012, ApJS, 199, 31

Ogasaka, Y., Kii, T., Ueda, Y., et al. 1998, Astronomische Nachrichten, 319, 43

Pacucci, F., Mesinger, A., Mineo, S., & Ferrara, A. 2014, MNRAS, 443, 678

Parmar, A. N., Smale, A. P., Verbunt, F., & Corbet, R. H. D. 1991, ApJ, 366, 253

Parmar, A. N., White, N. E., Giommi, P., & Gottwald, M. 1986, ApJ, 308, 199

Paul, B. 2013, International Journal of Modern Physics D, 22, 1341009

Paul, B., Kitamoto, S., & Makino, F. 2000, ApJ, 528, 410

Paul, B., & Naik, S. 2011, Bulletin of the Astronomical Society of India, 39, 429

Persic, M., & Rephaeli, Y. 2002, A&A, 382, 843

Peuten, M., Brockamp, M., Küpper, A. H. W., & Kroupa, P. 2014, ApJ, 795, 116

Pittori, C., Verrecchia, F., Chen, A. W., et al. 2009, A&A, 506, 1563

Postnov, K. A. 2003, Astronomy Letters, 29, 372

Postnov, K. A., & Kuranov, A. G. 2005, Astronomy Letters, 31, 7

Pottschmidt, K., Suchy, S., Rivers, E., et al. 2012, in American Institute of Physics Conference Series, Vol. 1427, American Institute of Physics Conference Series, ed. R. Petre, K. Mitsuda, & L. Angelini, 60–67

Power, C., James, G., Combet, C., & Wynn, G. 2013, ApJ, 764, 76

Power, C., Wynn, G. A., Combet, C., & Wilkinson, M. I. 2009, MNRAS, 395, 1146

Pradhan, P., Maitra, C., Paul, B., Islam, N., & Paul, B. C. 2014, MNRAS, 442, 2691

Pravdo, S. H., Becker, R. H., Boldt, E. A., et al. 1976, in Bulletin of the American Astronomical Society, Vol. 8, Bulletin of the American Astronomical Society, 512

Pravdo, S. H., & Ghosh, P. 2001, ApJ, 554, 383

Priedhorsky, W. C., Peele, A. G., & Nugent, K. A. 1996, MNRAS, 279, 733

Pritchard, J. R., & Furlanetto, S. R. 2007, MNRAS, 376, 1680

Raichur, H., & Paul, B. 2010a, MNRAS, 406, 2663

—. 2010b, MNRAS, 401, 1532

Ranalli, P., Comastri, A., & Setti, G. 2003, A&A, 399, 39

Rappaport, S., Verbunt, F., & Joss, P. C. 1983, ApJ, 275, 713

Rappaport, S. A., & Joss, P. C. 1983, in Accretion-Driven Stellar X-ray Sources, ed. W. H. G. Lewin & E. P. J. van den Heuvel, 13

Ray, P. S., & Chakrabarty, D. 2002, ApJ, 581, 1293

Reig, P. 2011, Ap&SS, 332, 1

Remillard, R. A., & McClintock, J. E. 2006, ARA&A, 44, 49

Revnivtsev, M., Lutovinov, A., Churazov, E., et al. 2008, A&A, 491, 209

Revnivtsev, M., Postnov, K., Kuranov, A., & Ritter, H. 2011, A&A, 526, A94

Reynolds, A. P., Quaintrell, H., Still, M. D., et al. 1997, MNRAS, 288, 43

Rodes-Roca, J. J., Mihara, T., Nakahira, S., et al. 2015, A&A, 580, A140

Rubin, B. C., Finger, M. H., Harmon, B. A., et al. 1996, ApJ, 459, 259

Ruderman, M., Shaham, J., Tavani, M., & Eichler, D. 1989, ApJ, 343, 292

Saraswat, P., Yoshida, A., Mihara, T., et al. 1996, ApJ, 463, 726

Sato, N., Nagase, F., Kawai, N., et al. 1986, ApJ, 304, 241

Sazonov, S. Y., Lapshov, I. Y., Syunyaev, R. A., et al. 1993, Astronomy Letters, 19, 272

Sguera, V., Bazzano, A., Bird, A. J., et al. 2006, ApJ, 646, 452

Shirasaki, Y., Kawai, N., Yoshida, A., et al. 2003, PASJ, 55, 1033

Sidoli, L., Romano, P., Mereghetti, S., et al. 2007, A&A, 476, 1307

Singh, N. S., Naik, S., Paul, B., et al. 2002, A&A, 392, 161

Staubert, R., Klochkov, D., & Wilms, J. 2009, A&A, 500, 883

Sterne, T. E. 1939, MNRAS, 99, 451

Stevens, I. R. 1988, MNRAS, 232, 199

Suchy, S., Fürst, F., Pottschmidt, K., et al. 2012, ApJ, 745, 124

Sugizaki, M., Mitsuda, K., Kaneda, H., et al. 2001, ApJS, 134, 77

Sugizaki, M., Mihara, T., Serino, M., et al. 2011, PASJ, 63, 635

Sunyaev, R. A., Churazov, E., Efremov, V., Gil'Fanov, M., & Grebenev, S. 1990, Advances in Space Research, 10, 41

Takahashi, T., Abe, K., Endo, M., et al. 2007, PASJ, 59, 35

Tanaka, Y. 1986, in Lecture Notes in Physics, Berlin Springer Verlag, Vol. 255, IAU Colloq. 89: Radiation Hydrodynamics in Stars and Compact Objects, ed. D. Mihalas & K.-H. A. Winkler, 198

Taylor, J. H., & Cordes, J. M. 1993, ApJ, 411, 674

Thompson, T. W. J., Tomsick, J. A., Rothschild, R. E., in't Zand, J. J. M., & Walter, R. 2006, ApJ, 649, 373

Tomida, H., Tsunemi, H., Kimura, M., et al. 2011, PASJ, 63, 397

Torrejón, J. M., Negueruela, I., Smith, D. M., & Harrison, T. E. 2010, A&A, 510, A61

Tsunemi, H., Kitamoto, S., Manabe, M., et al. 1989, PASJ, 41, 391

Tsunemi, H., Tomida, H., Katayama, H., et al. 2010, PASJ, 62, 1371

van den Heuvel, E. P. J. 1994, in Saas-Fee Advanced Course 22: Interacting Binaries, ed. S. N. Shore, M. Livio, E. P. J. van den Heuvel, H. Nussbaumer, & A. Orr, 263–474

van der Klis, M. 1989, ARA&A, 27, 517

van der Klis, M., & Bonnet-Bidaud, J. M. 1984, A&A, 135, 155

van der Klis, M., Wijnands, R. A. D., Horne, K., & Chen, W. 1997, ApJ, 481, L97

van der Meer, A., Kaper, L., van Kerkwijk, M. H., Heemskerk, M. H. M., & van den Heuvel, E. P. J. 2007, A&A, 473, 523

van Kerkwijk, M. H., van Paradijs, J., & Zuiderwijk, E. J. 1995, A&A, 303, 497

van Paradijs, J., & White, N. 1995, ApJ, 447, L33

Venkatesan, A., Giroux, M. L., & Shull, J. M. 2001, ApJ, 563, 1

Verbunt, F. 1993, ARA&A, 31, 93

Voges, W., Aschenbach, B., Boller, T., et al. 1999, A&A, 349, 389

Voss, R., & Ajello, M. 2010, ApJ, 721, 1843

Voss, R., & Gilfanov, M. 2007, A&A, 468, 49

Walter, R., & Zurita Heras, J. 2007, A&A, 476, 335

Watanabe, S., Sako, M., Ishida, M., et al. 2003, ApJ, 597, L37

Wen, L., Levine, A. M., Corbet, R. H. D., & Bradt, H. V. 2006, ApJS, 163, 372

White, N. E., & Swank, J. H. 1982, ApJ, 253, L61

White, N. E., Swank, J. H., & Holt, S. S. 1983, ApJ, 270, 711

Wijnands, R., & van der Klis, M. 1999, ApJ, 514, 939

Williams, B. F., Naik, S., Garcia, M. R., & Callanan, P. J. 2006, ApJ, 643, 356

Wolf, M., Harmanec, P., Šarounová, L., et al. 2004, A&A, 420, 619

Wolff, M. T., Ray, P. S., Wood, K. S., & Hertz, P. L. 2009, ApJS, 183, 156

Woosley, S. E., & Taam, R. E. 1976, Nature, 263, 101

Wu, Y. X., Yu, W., Li, T. P., Maccarone, T. J., & Li, X. D. 2010, ApJ, 718, 620

Zahn, J.-P. 1977, A&A, 57, 383

Zasche, P., Wolf, M., Vraštil, J., et al. 2014, A&A, 572, A71

Zezas, A., Fabbiano, G., Baldi, A., et al. 2007, ApJ, 661, 135